Spring 2018

MECHANISTIC STUDIES OF THE COMPLETE ELECTROCHEMICAL OXIDATION OF ETHANOL INTO CO2 OVER PLATINUM-BASED CORE-SHELL NANOCATALYSTS

Guangxing Yang
University of New Hampshire, Durham

MECHANISTIC STUDIES OF THE COMPLETE ELECTROCHEMICAL OXIDATION OF ETHANOL INTO CO_2 OVER PLATINUM-BASED CORE-SHELL NANOCATALYSTS

BY

GUANGXING YANG

Baccalaureate Degree, Chemical Engineering and Technology, South China University of Technology, Guangzhou, China, 2008

Master's Degree, Industrial Catalysis, South China University of Technology, Guangzhou, China, 2011

DISSERTATION

Submitted to the University of New Hampshire

In Partial fulfillment of the requirements for the Degree of

Doctor of Philosophy

in

Chemical Engineering

May, 2018

This dissertation has been examined and approved in partial fulfillment of the requirements for the degree of Doctor of Philosophy in Chemical Engineering by:

Dissertation Director, Dr. Xiaowei Teng,
Associate professor of Chemical Engineering, UNH

Dr. Nivedita Gupta, Professor of Chemical Engineering, UNH

Dr. Nan Yi, Assistant professor of Chemical Engineering, UNH

Dr. Sterling A. Tomellini, Professor of Chemistry, UNH

Dr. Anyin Li, Assistant Professor of Chemistry, UNH

On April 11, 2018

Original approval signatures are on file with the University of New Hampshire Graduate School.

CONTENTS

ACKNOWLEDGEMENTS

Firstly, I would like to express my sincere gratitude to my advisor Prof. Xiaowei Teng for the continuous scientific and financial support of my PhD study. His patience, motivation, immense knowledge and guidance helped me in all the time of research and writing of this thesis. He has taught me more than I could ever give him credit for here. I am also thankful for the excellent example he has provided as a successful and professional scientist.

Besides my advisor, I would like to thank the rest of my PhD dissertation committee: Prof. Nivedita Gupta, Prof. Nan Yi, Prof. Sterling A. Tomellini, and Prof. Anyin Li, for their invaluable support and dedication.

I would like to thank my coauthors: Prof. Anatoly I. Frenkel at Stony Brook University, Dr. Dong Su at the Brookhaven National Lab, Prof. N. Aaron Deskins and Dr. Lida M. Namin at Worcester Polytechnic Institute.

I also appreciate Chemical Engineering undergraduates Emily Wong, Alexander L. Radke, Ami L. Humphrey and Mitchell B. Juneau in the material synthesis and electrochemical tests. Also, I appreciate the help from Machine shop and University Instrument Center at the University of New Hampshire.

I gratefully acknowledge the funding sources that made my PhD work possible. I was funded by the teaching assistantship from Chemical Engineering department, research assistantship from the funding of National Science Foundation, and Dissertation Year Fellowship from graduate school.

My time at UNH was made enjoyable in large part due to my friends that became a part of my life. I am grateful for time spent with my group members, friends and roommates.

Nobody has been more important to me in the pursuit of my PhD degree than the members of my family. Love and encouragement from my parents, sister and brother supported and motivated me always. And most of all for my loving, supportive, encouraging and patient wife throughout this entire process, she made countless sacrifices to help me. Without her behind me, I doubt that I would be in this place today.

LIST OF TABLES

LIST OF FIGURES

ABSTRACT

MECHANISTIC STUDIES OF THE COMPLETE ELECTROCHEMICAL OXIDATION OF ETHANOL INTO CO_2 OVER PLATINUM-BASED CORE-SHELL NANOCATALYSTS

by

Guangxing Yang

University of New Hampshire, May 2018

Direct ethanol fuel cells (DEFCs) are a promising technology for the generation of electricity via the direct conversion of ethanol into CO_2, showing higher thermodynamic efficiency and volumetric energy density than hydrogen fuel cells. However, implementation of DEFCs is hampered by low selectivity of CO_2 generation at the anode where the ethanol oxidation reaction (EOR) happens. Therefore, anode catalysts with high reactivity for the EOR and high selectivity for CO_2 generation via breaking C-C bond are highly needed. To evaluate the catalysts' capability of splitting C-C bond of the ethanol molecule, highly sensitive CO_2 detection technique was developed in this research using a CO_2 microelectrode. Such an *in situ* CO_2 measurement tool enabled the real time detection of the partial pressure of CO_2 during the EOR using linear sweeping voltammetry measurements, through which electro-kinetic details of CO_2 generation could be obtained. Electro-kinetics of CO_2 generation were studied on the $PtRh/SnO_2$ core-shell catalysts made by a 'surfactant-free' method. The results showed that Pt and Rh components located in the core were partially oxidized and therefore

improved the CO_2 generation at low electrical potential. In addition, *in situ* CO_2 measurements provided the mechanistic understanding of potentiodynamics of the EOR, particularly the influence of *OH adsorbates on CO_2 generation rate and CO_2 selectivity. Our results showed that at low potential, inadequate *OH adsorbates impaired the removal of reaction intermediates, and thus Pt/Rh/SnO_2 exhibited the best performance toward CO_2 generation due to its strong ability to dissociate water molecules forming *OH oxidants, while at high potential, Rh sites were overwhelmingly occupied (poisoned) by *OH adsorbates, and thus Pt/SnO_2 exhibited the best performance toward CO_2 generation.

CHAPTER 1

INTRODUCTION

1.1 FUEL CELLS

Fuel cells, the devices that directly convert the chemical energy stored in fuels to electric energy, have been widely studied and used in many varieties, since the first hydrogen fuel cells were invented in 1838. Compared with conventional combustion-based technologies, fuel cells can operate at higher energy-conversion efficiencies without the limitation of the second law of thermodynamics, which is determined by the ratio of the Gibbs function change to the Enthalpy change in the overall cell reaction. To alleviate current energy crisis and environmental pollution, fuel cells can utilize renewable fuels such as ethanol and emit less pollutants. Moreover, the operation of fuel cells is safe, quiet and reliable because they are operated at a relatively low temperature and have fewer moving parts compared with heat engines. Motivated by the above advantages, fuel cells have been equipped to power vehicles recently.

1.2 PRINCIPLE

A variety of fuel cells have been developed, but they follow a similar working principle. Anode catalysts, electrolyte, and cathode catalysts comprise the necessary segments of a fuel cell. Catalysts loaded on electrodes are used to accelerate electrochemical reactions. For a typical process, fuels are transported onto the anode and then undergo an electrochemical oxidation on the anode catalyst, producing chemicals, electrons and

protons. The produced electrons travel though an external circuit (current) to power a given load. The generated protons pass through the electrolyte and membrane and reach the cathode to combine with oxidants (usually oxygen gas) and electrons from the external circuit to form products at the cathode.

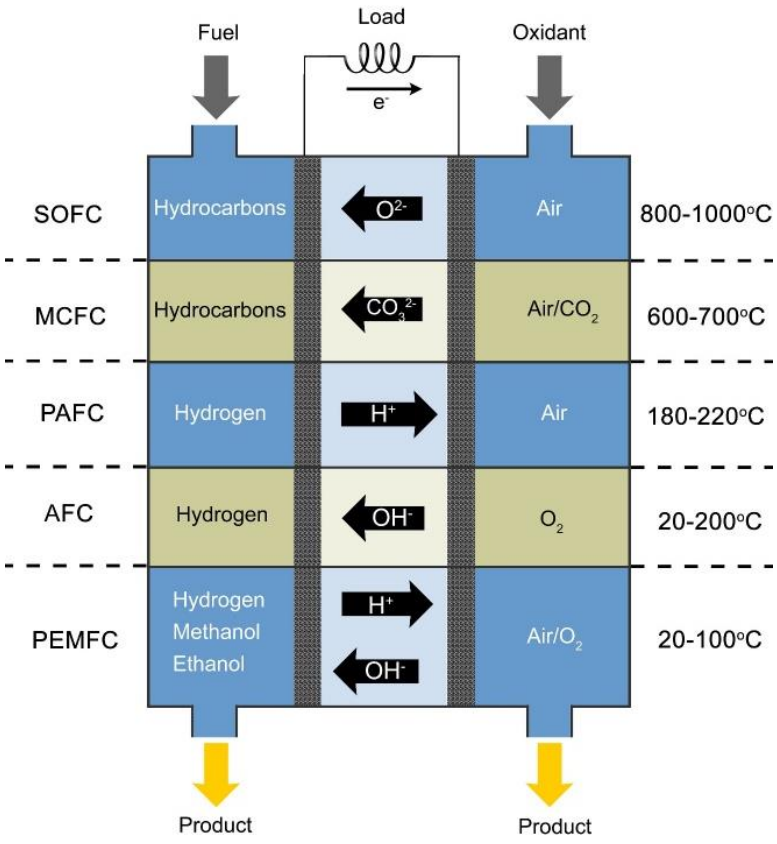

Figure 1.1 Classification of fuel cells by operation temperature

Fuel cells can be classified according to their operating temperatures, electrolytes and the corresponding conductive ions, which are summarized in the **Figure 1.1**. Solid Oxide Fuel Cells (SOFC) generally operate at very high temperature above 800 ºC to generate oxygen ions at the cathode migrating through the crystal lattice to oxidize fuel at the anode.[1] Molten Carbonate Fuel Cells (MCFC) need high temperature in the range of 600

to 700 ^{o}C to melt salts and conduct carbonate ions from the cathode to the anode.[2] The low-temperature fuel cells consist of Polymer Electrolyte Membrane Fuel Cells (PEMFC), Phosphoric Acid Fuel Cells (PAFC) and Alkaline Fuel Cells (AFC). PAFCs normally operate at temperatures between 180 °C and 220 °C, allowing high tolerance of carbon monoxide.[3] AFCs operate at temperatures between 20 and 200 ^{o}C in an alkaline solution with fast reaction kinetics, allowing lower quantities of noble metal catalysts.[4] PEMFCs operate at low temperatures ranging from 20 to 100 ^{o}C, delivering high-power density and offering the advantages of low weight and volume. Among various PEMFCs, hydrogen fuel cells have been commercialized widely. Other direct fuel cells such as methanol and ethanol have further advantageous for their ease of fuel delivery, storage, high safety and high power density.[5]

1.3 ACIDIC DIRECT ETHANOL FUEL CELLS

The direct ethanol fuel cells (DEFCs) are promising candidates for supplying portable power applications, where the chemical energy of the liquid ethanol is directly converted into electricity. Ethanol has an energy density of 8.03 kWh/kg, lower than that of hydrogen (32.8 kWh/kg). If taking the density of the fuel into account, however, the volumetric energy density of 6.28 kWh/L for ethanol is much higher than that of hydrogen gas compressed at 200 atm (0.18 kWh/L). In addition to the energy density, the theoretical thermodynamic energy efficiency of DEFC is much higher than that of the heat engine (97% vs. 35%). Even if we consider realistic operation conditions where the DEFC works at a voltage of 0.5 V and a current density of 100 mA/cm^2 with complete oxidation of

ethanol to CO_2 via a 12-electron transfer, the thermodynamic efficiency of a DEFC will be around 40%, comparable with a conventional diesel engine.[6]

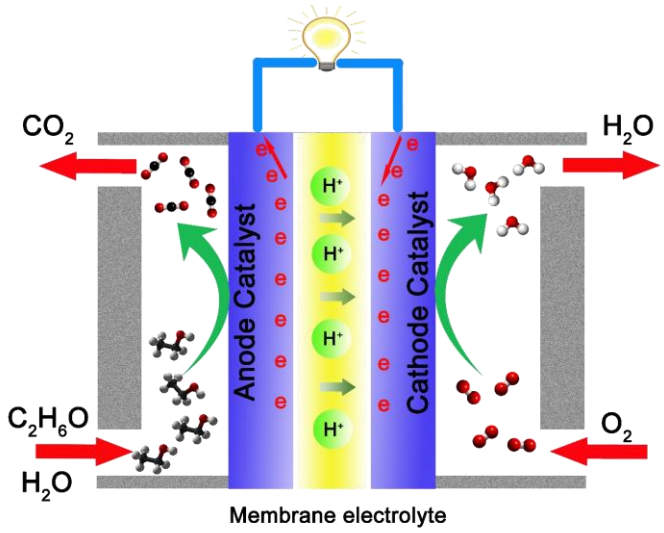

Figure 1.2 Schematic of the direct ethanol fuel cell

1.3.1 ANODE: ELECTROOXIDATION OF ETHANOL

$$C_2H_5OH + 3H_2O \rightarrow 2CO_2 + 12H^+ + 12e^- \quad E_a^o = -0.084 V vs.\ SHE \qquad 1.1$$

where SHE is the standard hydrogen electrode, E_a^o is the standard potential of ethanol oxidation at the anode, which can be calculated from the standard energy formation of species as the following equation 1.2.

For an ideal anodic reaction, ethanol is oxidized to CO_2 completely with 12-electron transfer. Unfortunately, the undesired products such as acetaldehyde and acetic acid are often produced under practical conditions, which will decrease the current density dramatically because only 2- and 4-electron transfer reactions happen for the formation

of acetaldehyde and acetic acid, respectively. To obtain higher current density, selectively breaking C-C bond to C_1 species such as $*CH_x$ and *CO will be necessary.

$$\begin{aligned} E_a^o &= -\frac{-\Delta G_r^o}{nF} \\ &= -\frac{2\Delta G_{CO_2}^f - \Delta G_{C_2H_5OH}^f - 3\Delta G_{H_2O}^f}{nF} \\ &= -\frac{2\times(-394.4)-(-174.8)-3\times(-237.1)\ kJ\cdot mol^{-1}}{12\times 96500\ C\cdot mol^{-1}} \\ &= -\frac{97.3\ kJ\cdot mol^{-1}}{12\times 96500\ C\cdot mol^{-1}} \\ &= -0.084\ V\ vs.\ SHE \end{aligned} \quad 1.2$$

1.3.2 CATHODE: ELECTROREDUCTION OF OXYGEN

$$3O_2 + 12H^+ + 12e^- \rightarrow 6H_2O \quad E_c^o = 1.229\ V\ vs.\ SHE \quad 1.3$$

where E_c^o at the cathode can be calculated by the following formula:

$$\begin{aligned} E_c^o &= -\frac{\Delta G_r^o}{nF} \\ &= -\frac{6\Delta G_{H_2O}^f - 3\Delta G_{O_2}^f}{nF} \\ &= -\frac{6\times(-237.1-0)\ kJ\cdot mol^{-1}}{12\times 96500 C\cdot mol^{-1}} \\ &= 1.229\ V\ vs.\ SHE \end{aligned} \quad 1.4$$

For the cathodic reaction, oxygen gas dissolves in water and transports onto the catalyst surface and then is reduced to water. The cathodic current is generally limited by the flux of oxygen transport.

1.3.3 OVERALL REACTION

Hence, the overall electrochemical ethanol fuel cell reaction can be written as

$$C_2H_5OH + 3O_2 \rightarrow 2CO_2 + 3H_2O \quad E^0_{Overall} = 1.145V \; vs.\; SHE \tag{1.5}$$

where the overall potential of the reaction can be calculated by the formula:

$$E^o_{Overall} = E^o_c + E^o_a = 1.229\,V - 0.084\,V = 1.145\,V \tag{1.6}$$

The overall reaction energy is

$$\Delta G^o_{Overall} = 2\Delta G^f_{CO_2} + 3\Delta G^f_{H_2O} - \Delta G^f_{C_2H_5OH} - 3\Delta G^f_{O_2} = -1325.3\,kJ \cdot mol^{-1} \tag{1.7}$$

Hence the specific energy by mass can be obtained as follows

$$W_e = \frac{-\Delta G^o_{Overall}}{3600 \times M_{ethanol}} = \frac{1325.3\,kJ \cdot mol^{-1}}{3600 \times 0.046\,kg \cdot mol^{-1}} = 8.0\,kWh \cdot kg^{-1} \tag{1.8}$$

where M is the molar mass of 0.046 kg/mol for ethanol.

This mass specific energy of ethanol is comparable with 6.0 kWh/kg of methanol and 13 kWh/kg of gasoline. Therefore, ethanol is a promising and alternative fuel for the low temperature direct fuel cells.

1.4 CATALYSTS FOR ELECTROOXIDATION OF ETHANOL IN ACID MEDIUM

The studies of the electrooxidation of ethanol have been reported since 1920s.[7] In the early years, pure platinum wire and foil or platinized metal were selected as model material for EOR in an acidic electrolyte.[8-16] The primitive studies on the influences of reaction temperature, ethanol concentration, electrolyte, and impurity were conducted. Over almost a century of development, the anode materials for EOR have been expanded

from bulk size material to nanomaterial, from platinum to other metals, and from single component to multi-component. In this section, the Pt-based and Pt-free electrocatalysts for EOR will be reviewed briefly.

1.4.1 PLATINUM SINGLE CATALYSTS

Metallic platinum has been widely used as electrocatalysts for EOR due to its high catalytic activity and passivity in acidic electrolytes. However, its high price and low abundance motivates researchers to minimize the amount without sacrificing the catalytic activity. Minimizing the size of Pt nanoparticles will increase the surface area exposed to reactants hence increasing the utilization of Pt atoms. Taking the size effect into account, Pt nanoparticles around 2.6 nm showed the best electrocatalytic activity with the size ranging from 1.7 to 13.9 nm.[17, 18] In addition, using a different carbon support such as carbon black, carbon nanotubes, and graphene with different surface area could change the platinum loadings and tune the distance between platinum particles. Thereby, adjust the diffusion of the reactants, intermediates and products.[19-24] It is reported that the Pt supported on graphene had higher catalytic activity than that on carbon black.[19]

Pt single crystal and polycrystal have been used as model catalyst to investigate the reaction mechanism assisted by infrared spectroscopy.[25-30] The investigation of the electrooxidation of ethanol on well-ordered surface planes of single crystal materials is an important approach to optimize the rate of the EOR and the selectivity of product. Some studies compared EOR processes at the smooth and stepped surface planes of Pt single crystal electrodes.[31-38] Korzeniewski et al found that the smooth surface of a Pt(111) electrode displayed lower electrocatalytic activities than the surfaces with step sites such as Pt(335) and Pt(557).[30, 39] More acetic acid formation was observed on

Pt(111) surface and more adsorbed CO on surfaces with high step density. Colmati et al showed that the surface with (100) steps was much less active for C-C bond breaking than surfaces with (110) steps,[36, 37] while the distributions of acetaldehyde and CO_2 were not affected by (110) steps in a perchloric acid solution.[33]

The faceted nanocrystals also showed similar properties to the single crystal with the same crystalline plane.[40, 41] For example, Tian et al synthesized tetrahexahedral Pt nanocrystals bounded by 24 facets of high-index planes. The tetrahexahedral Pt nanocrystals varying from 20 to 200 nm showed 3.3 times higher surface area specific current density than commercial Pt/C catalyst at 0.3 V vs. SCE (Saturated calomel electrode).[41] Moreover, this high index faceted Pt nanocrystals with size ranging from 2 to 10 nm had higher density of atomic steps which facilitated the C-C bond splitting to generate double the amount of CO_2 as commercial Pt/C catalyst.[42] Even after long-term cycling for ethanol oxidation, they still maintained the tetrahexahedral shape.[43]

1.4.2 PLATINUM-BASED BINARY CATALYSTS

A single-component Pt particle is not the most efficient electrocatalyst for the EOR because tenaciously adsorbed species generated during the reaction will poison the catalysts and result in quick loss of electroactivity. The addition of the other metal element coworking with Pt will mitigate the poisoning of Pt or tuning the selectivity of products though the bifunctional mechanisms or electronic effect. The following is the synopsis of several Pt-based binary anode catalysts commonly used for the EOR.

1.4.2.1 PLATINUM-RUTHENIUM CATALYSTS

Pt-Ru bimetal catalysts could be prepared by several approaches, such as electrochemically co-deposits of Pt and Ru,[44, 45] Ru modified Pt single crystal with

stepped surfaces,[46] Pt-Ru nanoparticles made by wet chemistry methods.[47-51]. Generally, the content of Ru in a Pt-Ru bimetal catalyst had a maximum value, depending on the preparation method.[47, 49, 52-54] A proper amount of Ru could provide sufficient sites for the dissociative adsorption of water molecules, and the resulting oxygenous species (e.g., *OH species) could serve as the oxidants and help the oxidation of adsorbed intermediates to CO_2, acetaldehyde, and/or acetic acid. The addition of Ru, therefore, could increase the current density of the EOR. However, high Ru content could result in the decrease of EOR activity due to the insufficient adsorption of ethanol on the limited Pt sites on catalyst surface. The mass spectrometric measurement showed that the main products during the EOR were acetaldehyde, acetic acid and CO_2. If we want to harvest 12-electron transfer reaction from the oxidation of ethanol, obtaining high selectivity toward CO_2 formation will be greatly important. However, it is worth mentioning that Ru addition not only helped the generation of CO_2 but also facilitated the formation of acetic acid. It has been considered that increasing the roughness of the Pt-Ru electrode and the step sites would yield more CO_2 production because both factors could facilitate C-C bond breaking.

Besides the composition effect, the alloying effect of Pt-Ru materials on the EOR have been investigated by several researchers. For example, Colmenares et al modeled the Pt/Ru catalysts as the mixture of PtRu alloy and RuO_x. By comparing the Pt-Ru/C catalysts with less alloying degree (less ratio of PtRu phase and high ratio of RuO_x phase) with the one with totally alloying (complete PtRu phase), they concluded that the catalysts with a less alloying degree had lower overall current and higher onset potential with more generation of acetic acid. With a fixed Pt/Ru atomic ratio, the alloying degree of Pt-Ru/C

was reflected by the lattice parameter of the PtRu alloy and the coordination number of Pt-Ru, which might determine the EOR activity. [55-57]

1.4.2.2 PLATINUM-TIN BINARY CATALYSTS

In general, Pt-Sn bimetallic catalyst has a higher current density than a pure Pt catalyst at lower potentials, which has been as one of the most important groups of anode catalysts for the EOR. The Pt-Sn catalysts can be synthesized through several approaches including thermal decomposition,[58, 59] electrochemical deposition,[60-63] colloidal method,[64-66] and impregnation reduction process[67-70]. The synthetic process could affect the particle size,[71] the structural configuration of Pt and Sn on catalyst surface,[66, 72] chemical valence of Pt and Sn on catalyst surface, alloying degree between Pt and Sn, alloyed crystal structure[66] and the composition. All these characteristics played important roles in determining electrocatalytic activity of the EOR. Apart from the material preparation, atomics ratios between Pt and Sn influenced the EOR performance of the Pt-Sn binary catalysts. The optimum composition of Sn in Pt-Sn catalyst was reported to be dependent on the synthetic approaches. The role of Sn element could increase the current density due to the supply of the *OH (product from the dissociative absorption of the water) for the oxidation of intermediates, while the role of Sn element on the CO_2 selectivity is still controversial.

Under mild synthetic conditions, the Pt-Sn alloys generally formed a face centered cubic structure. The nonalloyed Sn oxide, if any, was usually dispersed around the PtSn alloy. Therefore, the alloying degree of PtSn and the relative amount of PtSn alloy to SnO_x played important roles in EOR performance. Jiang et al showed that the $PtSnO_x$ exhibited higher current density than PtSn alloyed particle. They attributed the enhanced

performance to the Pt ensembles in $PtSnO_x$ without lattice dilation that favored the ethanol adsorption and C-C bond splitting, as well as to the tin oxide in the vicinity of Pt nanoparticles that offered sufficient *OH species to remove residues.[73] This study indicated that the relative amount of PtSn alloyed phase and nonalloyed Sn phase was important for the EOR. The formation of PtSn alloy could change the electronic environment of Pt component which displayed a weaker adsorption of intermediates compared with pure Pt nanomaterial. Therefore, intermediates could desorb easily from the Pt sites without C-C bond cleavage and combine with the *OH generated on adjacent SnO_2 sites. It is notable that although the presence of SnO_2 in the PtSn alloy-SnO_2 nanoparticle system was very important, it would dilute the Pt sites on the catalysts surface, leading to the low efficiency of Pt utilization.

1.4.2.3 PLATINUM-RHODIUM BINARY CATALYSTS

Pure Rh has been used as the electrocatalyst for the EOR in acidic electrolytes[74-79], which showed extremely low current comparing with pure Pt, but exhibited very high CO_2 selectivity. Alloying with Pt can tune the electronic structure of the Rh and provide synergic effect to improve the EOR performance, especially enhancing CO_2 selectivity. PtRh material could be prepared in the forms of nanoparticles,[80-82] nanocubes,[20] nanowires[83, 84] and Rh/Pt bilayer on Pt substrate[85] using different synthetic methods. Several studies showed the optimization of the Rh content in PtRh alloys for EOR. Rao et al and de Souza et al found an optimum Pt/Rh ratio of 9:1 for the best electroactivity of the EOR (high current density),[20, 79] however, other optimum ratios were reported by Cantane et al and Yuan et al.[77, 81, 83] It was reported that the presence of Rh in the PtRh bimetal system improved the CO_2 generation. It also suggested that Rh composition

cooperating with Pt atoms helped the cleavage of C-C bond of C_2 species. Only concerning the CO_2 selectivity, the optimum of Rh content may not be the same with the one required for the high overall current density, probably because of slower kinetics of EOR on Rh sites than those on Pt sites.[86]

Other metals can be introduced to improve the electroactivity of the EOR by the formation of PtBi nanomaterials,[87, 88] PtIr,[89, 90] Os on Pt single crystals [91-93], PtRe,[94] PtCo,[95] PtNi[96], Pt/CeO_2,[97, 98] Pt/La_2O_3,[99] Pt/TiO_2[100, 101] binary catalysts. Santos et al showed that low Os coverage (around 0.15) on Pt(100) single crystal facilitated the complete oxidation of ethanol to CO_2 and the high Os coverage up to 0.33 produced more acetaldehyde and acetic acid.[91] But the coverage of Os on Pt(110) showed different relationships with products distribution.[92] In addition, Du et al showed that $Pt_{95}Bi_5$ nanowire displayed higher steady current than commercial Pt at 0.55 V vs. Ag/AgCl, due to the enhanced adsorption of water on Pt sites adjacent to Bi atoms, and consequently an increased rate of oxidation.[88]

1.4.3 PLATINUM-BASED TERNARY CATALYSTS

To further increase the activities of binary catalysts for the EOR and enhance the ability to break C-C bond then to form CO_2, a third metal component is generally added to form ternary catalysts through synergistic interaction between three components. There are many different combinations for Pt-based ternary catalysts used in acidic environment, Pt-Ru-M (M=Rh,[102-104] Ni,[105, 106] Mo,[107-110] W,[108, 111] Bi,[87, 112] Co,[113] Cu,[114] and Pb[115]), and Pt-Sn-M (M=Rh,[78, 116-123] Ru,[124-127] Ir,[90] Re,[94] Pd,[116, 128, 129] Ni[116, 130, 131], Co[116], and Cu[132]). Among these Pt-based ternary catalysts, Pt-Sn-Rh and Pt-Ru-Sn catalysts are chosen for the briefly review in the following sections.

1.4.3.1 PLATINUM-TIN-RHODIUM TERNARY CATALYSTS

In the cases of Pt-Rh-Sn systems, Rh was generally alloyed with Pt, hence forming bi-phase PtRh-SnO_2 materials with a PtRh alloy and a segregated SnO_2 phase. They have been considered as the best group of catalysts for the EOR due to the excellent abilities for the adsorption, dehydrogenation, and oxidation of ethanol via C-C bond splitting, as well as plausible chemical stability.[117, 118, 120-122, 133] The superiority of Pt and Rh towards C-C bond splitting has been demonstrated by density functional theory (DFT) calculations, showing that Pt-Rh helped cleave the C-H bond of the terminal methyl group (β-carbon dehydrogenation) and form oxometallate intermediate (M-CH_2-CH_2-O-M).[134] Oxophilic Sn, on the other hand, interacted with water strongly to form an oxygenated species on catalyst surface (OH_{ads}), which helped oxidize reaction intermediates (e.g. CH_x and CO) generated on adjacent Pt or Rh sites.[62, 66] Attributed to this bifunctional effect, Pt/Rh/Sn ternary catalysts have been generally considered as the most effective materials towards EOR, especially at higher overpotential. However, fuel cells generally tend to operate at an external potential close to their equilibrium potential. At low overpotentials, the Pt/Rh/Sn components showed a weak dissociative adsorption of water, and the resulting low OH_{ads} coverage on catalyst surface might not be adequate to remove the strongly adsorbed reaction intermediates especially CO that poisoned the active sites.

1.4.3.2 PLATINUM-RUTHENIUM-TIN TERNARY CATALYSTS

Platinum-ruthenium-tin ternary (Pt-Ru-Sn) catalysts have different structure configurations, surface chemistry, and compositions due to the variations of the synthetic approaches, forming various ternary structures including PtSn alloy with Ru oxide, PtRu alloy with Sn oxide, PtSn and PtRu alloys with Sn and Ru oxides, PtRuSn ternary alloy,

PtSn alloy with PtRu alloy, and Pt particles with segregated Sn and Ru oxides. In the cases of the presence of either Sn oxide or Ru oxide, the amount of oxides should not exceed a critical value in order to guarantee sufficient Pt sites accessible to ethanol molecules. Chang et al reported that the surface Ru oxide, which interacted with surface amorphous SnO instead of well crystallized SnO_2, worked with PtSn alloyed component to promote the performance of the EOR.[124] The ratio of Ru and Sn was suggested as a key parameter in these ternary catalysts affecting the electroactivity of the EOR.[135] On the other hand, the Ru-rich PtRuSn catalysts showed the lowest onset potential of EOR due to the oxidative removal of the intermediates on Pt sites by oxidants generated on adjacent Ru sites. However, the Sn-rich PtRuSn catalyst, where the PtSn alloy and SnO_2 existed, facilitated C-C bond cleavage and hence improved the EOR current.[136] Liu et al synthesized both reduced and oxidized PtRuSn ternary catalysts and showed that RuO_2 helped the removal of adsorbed CO only in the high potential range, while Pt_3Sn, SnO and SnO_2 components promoted the EOR performance throughout the potential window by oxidizing $C_2H_4O_{ads}$ and/or CO_{ads} further by SnO and RuO_x via a bifunctional mechanism.[127]

1.4.4 PLATINUM-FREE METAL CATALYSTS

Besides pure platinum, pure rhodium and iridium can also be used as catalysts but with lower electroactivities than platinum. Interestingly, the major product on pure Rh was CO_2, whereas the major product on pure Ir was acetic acid.[74, 76]

Iridium-tin binary catalysts showed high electroactivity of the EOR at low potentials.[137-139] Du et al synthesized the Ir/IrSn/SnO_2 core-shell particle, consisting of an Ir-rich core and an IrSn alloy shell with SnO_2 present on the surface using a “surfactant free”

synthesis process. The carbon supported IrSn catalysts showed a very low peak potential around 0.07 V vs. Ag/AgCl during the EOR, agreeing well with the peak potential at 0.04 V vs. Ag/AgCl on Ir-Sn nanowires with abundant oxidized Sn. IrRu and IrRh alloys were synthesized and evaluated for the EOR as well.[140, 141] It was found that $Ir_{77}Ru_{23}$/C and Ir_4Rh_1 both had superior catalytic activities for the EOR compared to Ir/C and commercial Pt/C catalysts, probably due to the lower reaction energy of the C-C bond splitting than those on Ir and Ru catalysts.[140, 141]

1.5 MECHANISMS FOR ELECTROOXIDATION OF ETHANOL IN ACID MEDIUM

The mechanism of the electro-oxidation of ethanol for varying potentials in acid medium on Pt catalyst was investigated by differential electrochemical mass spectrometry (DEMS), Fourier transform infrared spectroscopy (FTIRS), sum frequency generation spectroscopy (SFGS) and surface enhanced Raman spectroscopy (SERS).[25, 34, 35, 142, 143] It was concluded that the EOR process started with the adsorption of ethanol on Pt. Then, the adsorbed ethanol underwent the α-dehydrogenation (dehydrogenation of C-H where the C atom bonded to the -OH functional group) and then formed adsorbed acetaldehyde which further decomposed to adsorbed C_1 species such as $*CH_x$ and *CO. Therefore, C-C bond splitting at low potentials below 0.3 V may take place readily with slow kinetics. Unfortunately, *CO could not be oxidized to CO_2 easily in such a low potential range without the participation of the oxidants, and therefore it would poison Pt sites due to its strong interaction with Pt and then blocked the ethanol adsorption, leading to the low current observed from CVs below 0.3 V. Subsequently, with increasing potential

applied, more *OH species were generated from the dissociation of water, which could interact with *CH_x and *CO formed at low potentials.[143] As a result, CO_2 generation occurred via the oxidation of the *CH_x and *CO by *OH, confirmed by the *in situ* FTIR results where the signal from CO_2 increased coupled with the decreased signal from *CO. However, the experiments involving isotope-labeled ethanol showed that main CO_2 generation attributed to the oxidation of *CO rather than *CH_x, likely because some *CH_x was reduced to methane at low potentials which was observed from DEMS and *CH_x still survived at higher potentials. After the removal of CH_x and CO, the unoccupied Pt sites adsorbed ethanol and then broke C-H bonds to produce acetaldehyde, or the adsorb ethanol was oxidized by *OH to acetaldehyde at the intermediate potentials, confirmed by the increasing signal from acetaldehyde by DEMS and FTIR techniques. Further increasing potential could oxidize adsorbed ethanol and acetaldehyde to acetic acid with fast kinetics in the presence of abundant *OH, which was a rather stable species and could be further oxidized to CO_2. However, in most potential regions, acetaldehyde and acetic acid were the major products, though CO_2 was always detected, indicating that C-C bond splitting proceeded but suffered slow kinetics. Based on the discussion above, the main reaction steps of the electro-oxidation of ethanol are proposed in different potential domains as follows (To simplify the discussion, other intermediates are not considered.):

Starting with α-dehydrogenation

$$CH_3CH_2OH \rightarrow *CH_3CH_2OH \quad (1.9)$$

In the low potential region: E < 0.3 V

$$*CH_3CH_2OH \rightarrow *CH_x + *CO \quad (1.10)$$

$$CH_3CH_2OH \rightarrow *CH_3CHO \quad 1.11$$

$$*CH_3CHO \rightarrow *CH_x + *CO \quad 1.12$$

$$*CH_x \rightarrow CH_4 \quad 1.13$$

In the middle potential region: 0.3 V < E < 0.6 V

$$*CH_x + *OH \rightarrow CO_2 \quad 1.14$$

$$*CO + *OH \rightarrow CO_2 \quad 1.15$$

In the high potential region: E > 0.6 V

$$CH_3CH_2OH \rightarrow *CH_3CHO \quad 1.16$$

$$*CH_3CHO \rightarrow CH_3COOH \quad 1.17$$

$$CH_3CH_2OH \rightarrow *CH_3COOH \quad 1.18$$

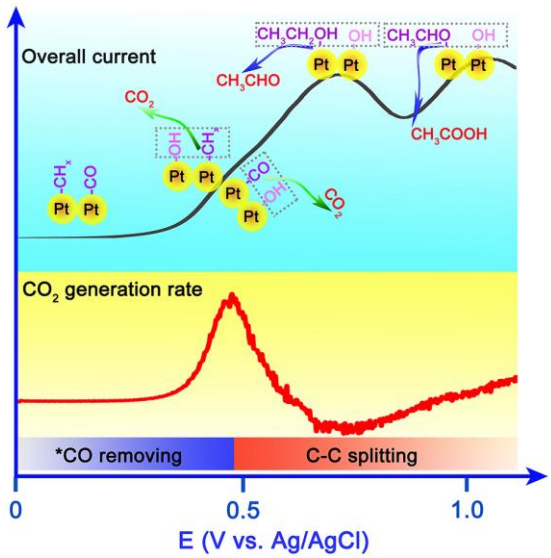

Figure 1.3 Proposed reaction domain of the electro-oxidation of ethanol (Upper) on pure Pt; proposed limiting steps of CO_2 generation on Pt (Bottom).

To summarize, EOR began with ethanol adsorption, and then dehydrogenation. C-C bond is broken readily below 0.3 V forming *CO and CH_x. Aided by the *OH from the

dissociation of water above 0.3 V, CO_2 generated from the oxidation of *CO and *CH_x. Thereafter, acetaldehyde and acetic acid become the main products in the presence of a large amount of *OH, while CO_2 contributed less to the final products. The scheme of the proposed mechanism is shown in **Figure 1.3**. In that case, improving the C-C bond splitting ability and enhancing the *CO removal rate should be an effective way to gain a higher CO_2 generation rate with higher CO_2 selectivity.

1.6 TECHNIQUES FOR STUDYING ELECTROOXIDATION OF ETHANOL

The mechanisms of the electrooxidation of ethanol can be indirectly understood by investigating the current signals at a given potential using specific electrochemical apparatus, where the voltage can be continuously increased or decreased linearly with respect to time. By changing the scanning rate, the electrochemical kinetics can be analyzed. To further study the reaction mechanism of electrooxidation of organic compounds, mass spectrometry or spectral technics coupled with electrochemical methods have been developed to deliver qualitative and quantitative results of the final products and intermediates during the electrochemical process. In the following sections, these techniques will be discussed in detail.

1.6.1 CHRONOAMPEROMETRY (CA) AND CYCLIC VOLTAMMETRY (CV)

Chronoamperometry is a technique that the potential of the working electrode is stepped and the resulting current from faradaic processes occurring at the electrode is monitored as a function of time **Figure 1.4** a. Taking a simple elementary reaction as an

example, the reactant at a more reduced state (R) is oxidized at the electrode surface to form a product at a more oxidized state (O) ($R \rightleftharpoons O + e$), accompanied by the generation of the electron.

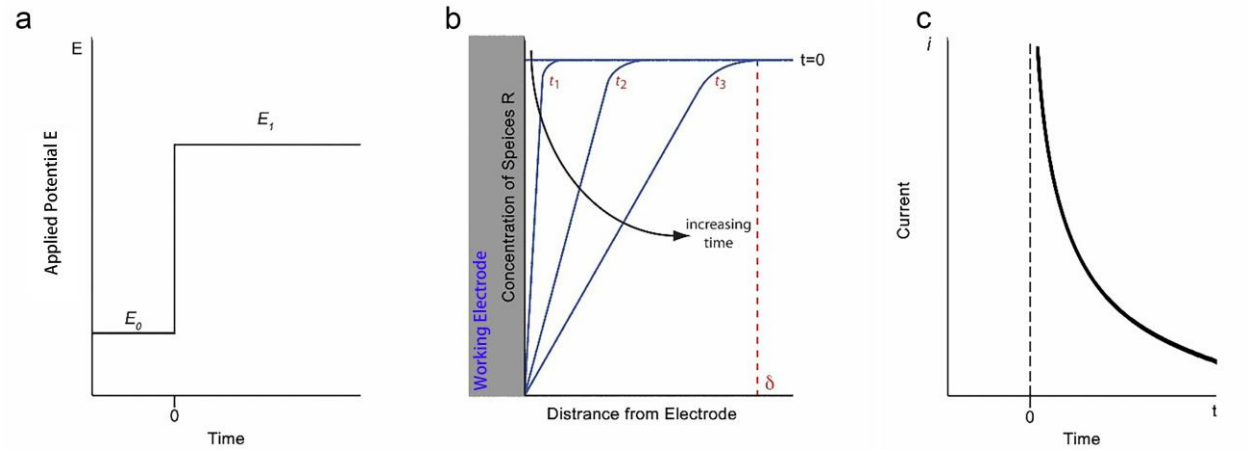

Figure 1.4 (a) Step increasing the potential at working electrode from E_0 to E_1 (b) Concentration profile of reactant R varying from the distance to the electrode and time. (c) Current with respect to time at E_1.

When the potential is applied to the electrode, the reaction starts producing a very large current at the initial stage due to a large amount of reactant R at the surface. Subsequently, the current decreases because of the decrease in the concentration of species R at the electrode surface. It is notable that there will be a concentration gradient of species R from the bulk solution to the electrode surface. Therefore, species R diffuses from the bulk solution to the electrode surface and then will be totally oxidized to species O at the electrode surface. The flux of species R, hence the current of the electrochemical process, is proportional to the concentration gradient of the species R at the electrode surface. As the reaction proceeds, the thickness of diffusion layer becomes thicker, resulting in smaller gradient of concentration and correlated smaller current as shown in

Figure 1.4 b. Hence, a curve with respect to time was obtained, named by chronoamperometry, as shown in **Figure 1.4** c.

The potential is increased step by step from E_1 to E_5 and then each step is kept for a given time as shown in **Figure 1.5** a. E_1 does not reach the potential that can activate the oxidation, so the current is 0 as curve 1 in **Figure 1.5** b. E_2 and E_3 can activate the oxidation reaction but the reaction rate is not high enough to consume all the reactants, therefore the concentration of species R is not zero. So the current depends on the applied potential at the early stage depicted as curve 2 and 3 in **Figure 1.5** b. When the potential is increased to E_4 high enough to consume all the surface R species immediately, so the current depends on the diffusion rate of the R. Even though the potential is stepped to even high potential E_5, the current profile will not change as shown in **Figure 1.5** c.

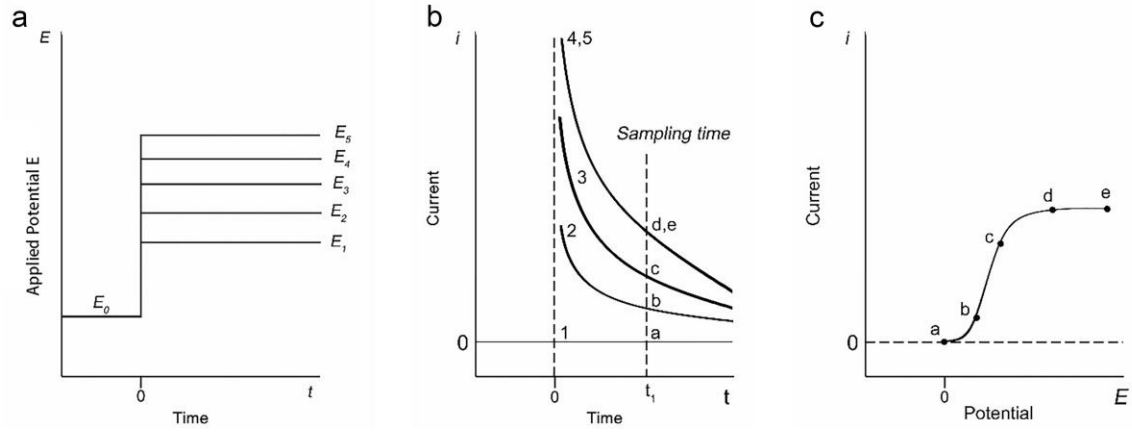

Figure 1.5 (a) Step increasing applied potentials. (b) Current curves in response to the steps. (c) Sampled-current voltammogram.[144]

Linear sweep voltammetry (LSV) is the technique where the voltage changed with respect to time by a linear function from initial potential E_0 to high limit potential E_h. If the

potential reaches the high limit and then goes back to the initial potential to complete one cycle scan, it is called cyclic voltammetry (CV) which has become a necessary tool for studying electrochemical reactions (**Figure 1.6** c).

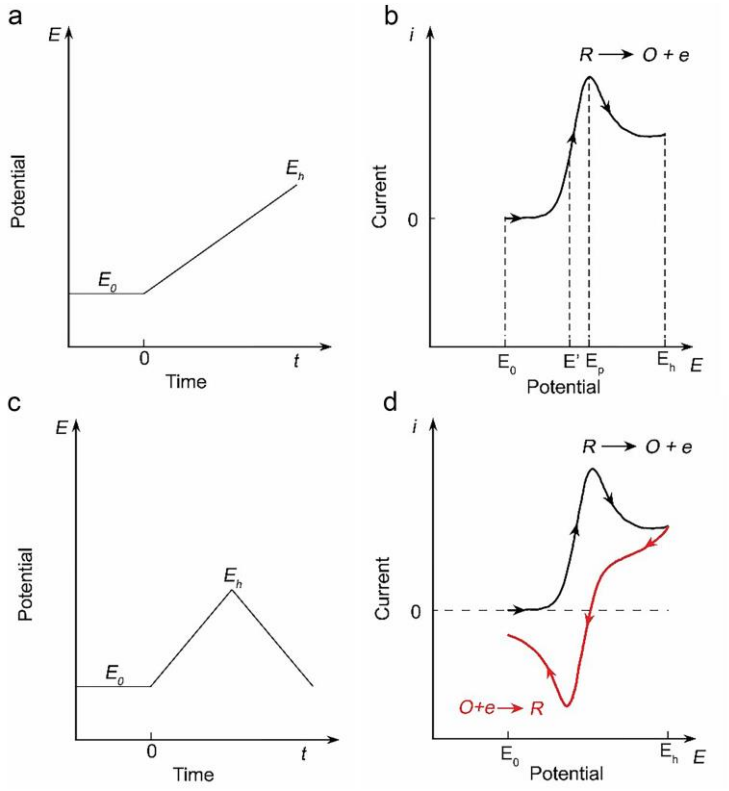

Figure 1.6 (a) Linear sweeping potential from E_0 up to E_h and (b) resulting oxidation current curve. (c) cyclic sweeping potential from E_0 upto E_h then back to E_0 and (d) resulting a cyclic voltammogram.[144]

CV curves can offer both thermodynamics and kinetics information. For a typical LSV curve, if the initial potential E_0 is much lower than the oxidation potential E', then there is non-faradaic current at the early stage. When the potential increase to the vicinity of the oxidation potential, the oxidation occurs, resulting in the increase of current. As the potential increases more positively and eventually reaches the oxidation potential, R is oxidized to O, and therefore the concentration of species R at the electrode surface starts

to drop, which results in the concentration of species R at the electrode surface approaching nearly to zero. Therefore, the current depends on the mass transfer rate of species R. As the reaction continues, the concentration gradient of species R near the electrode surface becomes smaller, and the rate of mass transfer starts to drop, resulting in the drop of current. Over the reaction time, the diffusion reaches the steady state, so does the current, which results in a plateau in the high potential range after the current drop. The peaked current-potential curve is depicted in **Figure 1.6** b.

When the potential reaches the highest value, the concentration of species R at the electrode surface is nearly zero, while the concentration of the oxidation product (species O) is very high. When the potential decreases to the low potential values with the same scan rate as shown in **Figure 1.6** c, the current will not turn to a negative value immediately due to the existence of electrooxidation process and possible non-faradaic contributions. As the potential reaches the electroreduction potential E', the electroreduction of species O dominates the current. The reversal current shape resembles the forward shape of electrooxidation of species R as shown in **Figure 1.6** d.

CV and CA techniques can provide some basic kinetic information for the electrooxidation of ethanol. Rightmire et al applied CV to investigate the EOR in 0.5 M H_2SO_4 over the platinum surface from 0.05 to 1.9 V versus SHE, from which two oxidation peaks at ~0.9 V and ~1.3 V during the forward scan and one oxidation peak at ~0.7 V during the backward scan were observed. The first forward peak at ~0.9 V was assigned to the surface oxidation of Pt surface and the partial oxidation of ethanol (Eqs. 1.19-1.21). The second forward peak was due to the competition of the gradual poisoning of the Pt surface (Eq.1.22) and the oxidation of ethanol (1.23)

$$Pt + nH_2O \xrightarrow{slow} Pt(OH)_n + nH^+ + ne^- \quad 1.19$$

$$Pt(OH)_n \xrightarrow{fast} Pt(O)_n + nH^+ + ne^- \quad 1.20$$

$$Pt + nCH_3CH_2OH \xrightarrow{slow} Pt(OCH_2CH_3)_n + nH^+ + ne^- \quad 1.21$$

$$H_2O + Pt(OCH_2CH_3)_n \rightarrow Pt(O)_n + nCH_3CH_2OH + nH^+ + ne^- \quad 1.22$$

$$Pt(OCH_2CH_3)_n \rightarrow Pt + nCH_3CHO + nH^+ + ne^- \quad 1.23$$

During the backward scan, the oxide film on the Pt electrode was reduced until to 0.85 V, where the Pt electrode was reactivated to oxidize ethanol or residue to form the oxidation peak in the backward scan. The peak current increased with the concentration of the ethanol. The relative intensity between the first and second forward peaks reversed if the concentration of ethanol increased. Also, all the peaks shifted to high potential as the concentration of ethanol increased. In the range of low concentration of ethanol, the overall reaction order (m) can be calculated according to the formula (Eq. 1.24), which was found around the first order reaction.

$$\log(j) = \log\left(\frac{nFk}{S}\right) + m\log(c) \quad 1.24$$

where j is the current density, n is the charge transfer number, F is the Faraday constant, S is the geometric surface area of the electrode, c is the concentration of the ethanol, m is the overall reaction order.

Tafel slope and exchange current density of the EOR can be obtained from CVs, described as:

$$\eta = 2.303\frac{RT}{\alpha nF}\log\left(\frac{j}{j_0}\right)$$

$$= 2.303\frac{RT}{\alpha nF}\log(j) - 2.303\frac{RT}{\alpha nF}\log(j_0) \qquad 1.25$$

where η is the over-potential, α is the anodic transfer coefficient, n is the number of electrons transferred in the reaction, j is the current density, and j_0 is the exchange current density when over-potential is equal to zero. Tafel slope defined as $\frac{2.303RT}{\alpha nF}$ and the exchange current can be calculated from the intercept of the plot of overpotential vs. $\log(j)$.

1.6.2 FOURIER TRANSFORM INFRARED SPECTROSCOPY (FTIR)

Since the 1960s *in situ* IR has been used as a powerful tool to analyze reaction intermediates and surface species in the electrochemical processes in both the static electrochemical cell and the flow electrochemical cell. In general, internal and external reflection configurations for cell design were applied to minimize the IR absorption by electrolyte as shown in **Figure 1.7**. For the external reflection configuration depicted in **Figure 1.7** a, the electrode sample is placed very close to the light guiding prism. There is a thin layer of electrolyte between the catalyst and prism, allowing the detection of the species dissolved in electrolyte and adsorbed on catalyst surface as shown in **Figure 1.7** b. The disadvantage of this design includes the mass transport between the thin layer and the bulk electrolyte usually causing deficient concentration of ethanol on the catalyst surface.

On the other hand, in an internal reflection mode with an attenuated total reflection (ATR) a thin catalyst supported on a thin metal film deposited on a prism with high refractive index is used as the working electrode depicted in **Figure 1.7** c.[145, 146] Since

the IR beam contacts with the back of electrode, the front of the electrode can be merged in thick solution layer, facilitating mass transport and giving a quick response of FTIR signal with the function of potential at a fast scanning rate as shown in **Figure 1.7** d.

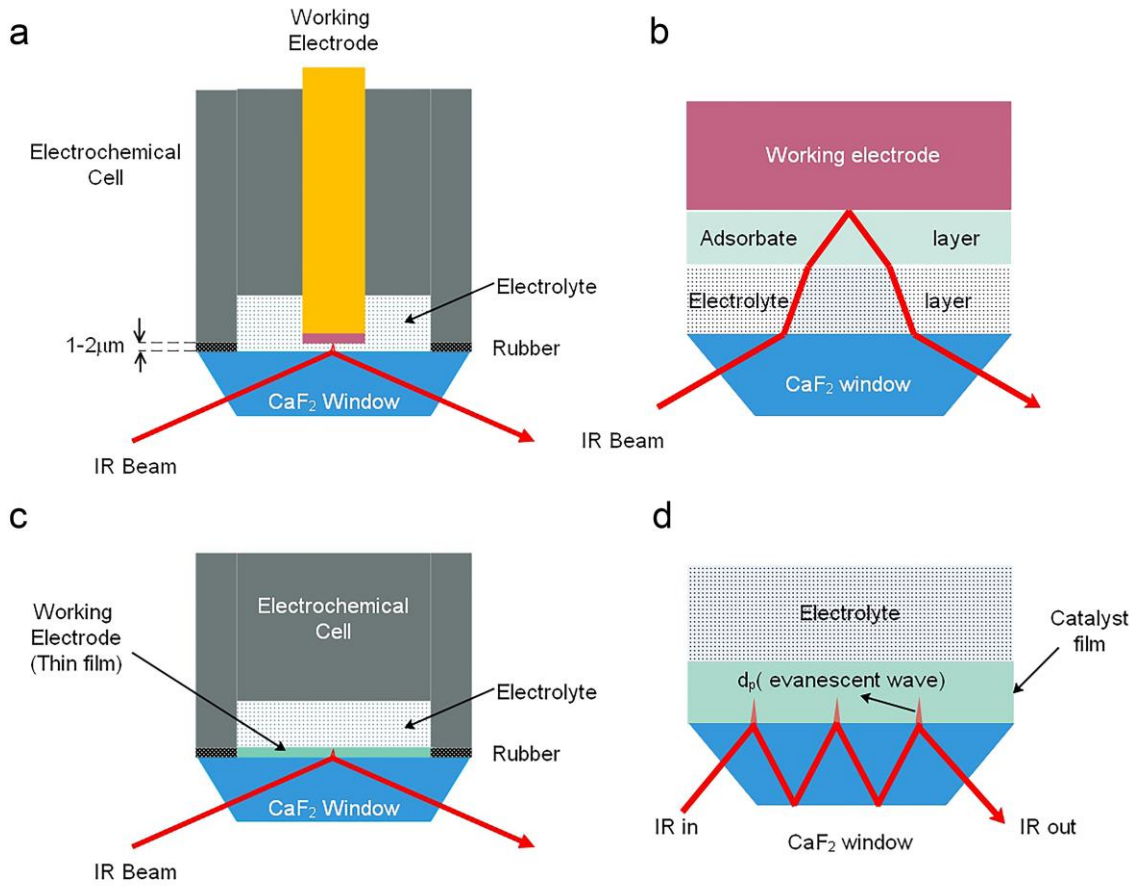

Figure 1.7 (a) External *in situ* FTIR electrochemical cell and (b) the corresponding pathway of IR. (c) Internal *in situ* FTIR electrochemical cell and (d) the corresponding pathway of IR.

Mid-IR can detect the different stretching modes of adsorbed CO from 1800 to 2000 cm^{-1} on the catalyst surface and CO_2 at 2343 cm^{-1} generated after C-C bond breaking of ethanol. Also, it can identify the acetaldehyde and acetic acid from the incomplete oxidation of ethanol indicated by the C=O bond stretching near 1720 cm^{-1}. Meanwhile, the C-O single bond stretching at 1044 cm^{-1} can reveal the consumption of ethanol. The

data acquisition with high quality during *in situ* IR spectroscopic measurement enables researchers to calculate the relative selectivity of products of interest and postulate the reaction pathways of ethanol oxidation at different potentials. Infrared spectroscopic studies showed that the electrooxidation of ethanol from the bulk solution commenced after the consumption of the adsorbed *CO intermediate.[29, 147-150] In addition to adsorbed *CO, other adsorbed species containing ethoxy, acetyl and alcohol groups were also identified.[25]

1.6.3 RAMAN SPECTROSCOPY

The configuration of an *in situ* Raman spectroscopic cell is similar to the *in situ* IR cell as shown in **Figure 1.8** a. Raman spectroscopy can reflect the information of vibrational, rotational, and other low-frequency modes in a system, provided by inelastic scattering including Stokes scattering and anti-Stokes scattering, and elastic scattering dominantly contributed by Rayleigh scattering as shown in **Figure 1.8** b.

During the electrooxidation of ethanol, the formation of the adsorbed CH_x species was only postulated on the finding of an adsorbate by FTIR[39] and DEMS[151], which can be desorbed either as CH_4 via hydrogenation or CO_2 via oxidation. However, FTIR neither can directly distinguish C-H vibration of adsorbed *CH_x from that of CH_x groups in molecules nor detect the low frequency vibration modes such as Metal-CO (v_{M-CO}) stretching and Metal-CH_x (v_{M-CHx}) stretching in the range of 400-500 cm^{-1}.[142] Raman spectroscopy based on visible light rather than infrared light is able to obtain the low frequency vibration below 700 cm^{-1},[152] a region that infrared spectroscopy is hard to reach due to the limited transparency of most optical windows in that range. Along with small Raman scattering of water, Raman spectroscopy works better than infrared

spectroscopy to observe metal-adsorbate vibration modes in aqueous electrochemical cell.

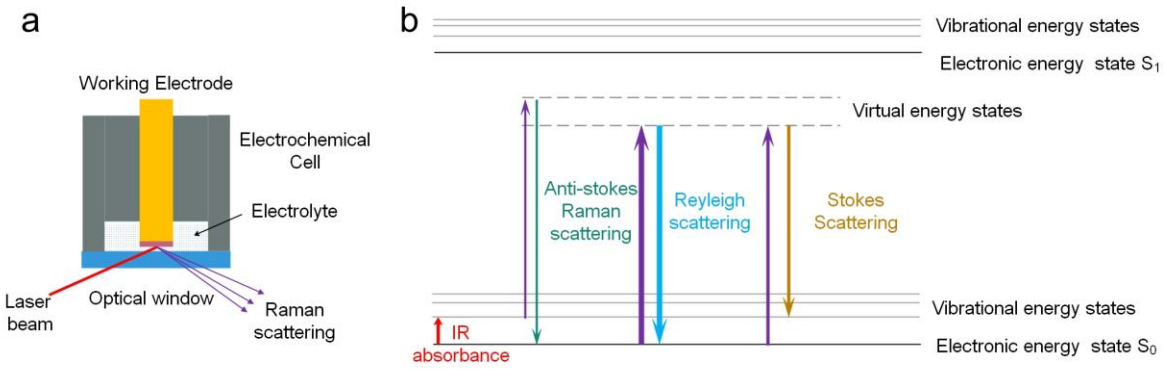

Figure 1.8 (a) *in situ* Raman spectroscopic electrochemical cell. (b) Energy-level diagram showing the states involved in Raman spectra.

Lai et al employed isotopically labeled compounds for Raman spectroscopic study, identifying the adsorbed *CH_x should be CH as the decomposition product of ethanol. Their results showed that CH fragment can be oxidized to CO_2 on Pt(111) surface at low potentials.

1.6.4 SUM-FREQUENCY GENERATION SPECTROSCOPY (SFGS)

FTIR spectroscopy has been widely used to detect the reaction intermediates to investigate reaction pathways for ethanol electrooxidation. However, the signal of FTIR can result from both species adsorbed on catalyst surface and species in bulk solution. Infrared-visible SFG spectroscopy can be used to only detect surface adsorbed species without the contribution of the solution. In a SFG spectroscopy, two laser beams are temporal and spatially overlapped on the sample. One of the laser beams has a fixed energy in the region of visible light with frequency of ω_{Vis} and the other laser beam has

tunable energy in the region of infrared light with frequencies of ω_{IR}. Light is emitted at the sum of the two incident frequencies $\omega_{SFG} = \omega_{Vis} + \omega_{IR}$ as depicted in **Figure 1.9**.

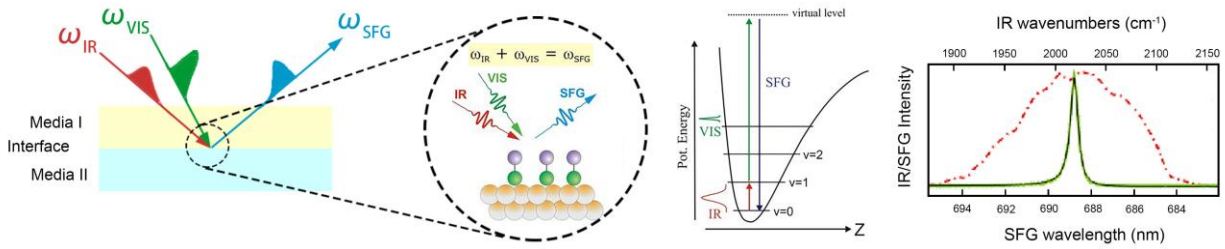

Figure 1.9 Principle of sum frequency generation spectroscopy

When the frequency of the tunable infrared beam coincides with a vibrational mode of the molecules at the interface, the intensity of the output light is resonantly enhanced. The SFG intensity is a measure of the second-order susceptibility $\chi^{(2)}$ of the sample. In the dipole approximation $\chi^{(2)}$ vanishes ($\chi^{(2)} = 0$) in centrosymmetric media: the bulk of the sample. However, at surfaces and interfaces the symmetry is broken, and therefore SFG is active. Thus, SFG spectroscopy is sensitive and selective to the species present at the surfaces and interfaces. In a typical *in situ* SFG electrochemical cell shown in **Figure 1.10** a, the light goes through the electrolyte layer (**Figure 1.10** b), and only the surface species respond to the signal changes. By detecting the sum frequency (SF) light with respect to infrared frequency, a vibrational spectrum is obtained. Since SFG is a second-order non-linear optical process that occurs only at a medium (interface) where the inversion symmetry is broken. Thus, only the adsorbed species can be detected. SFG was first applied to detect the C-H stretching model at the liquid/solid interfaces by Guyot-Sionnest et al.[153] Then it was applied to the investigation of CO vibrational bands during

electrochemical reactions.[154-158] Later, other surface-adsorbed species such as acetaldehyde, acetyl, acetate and (bi)sulfate have been identified as the adsorbed species on the catalyst surface in electrochemical reactions.[143, 159, 160]

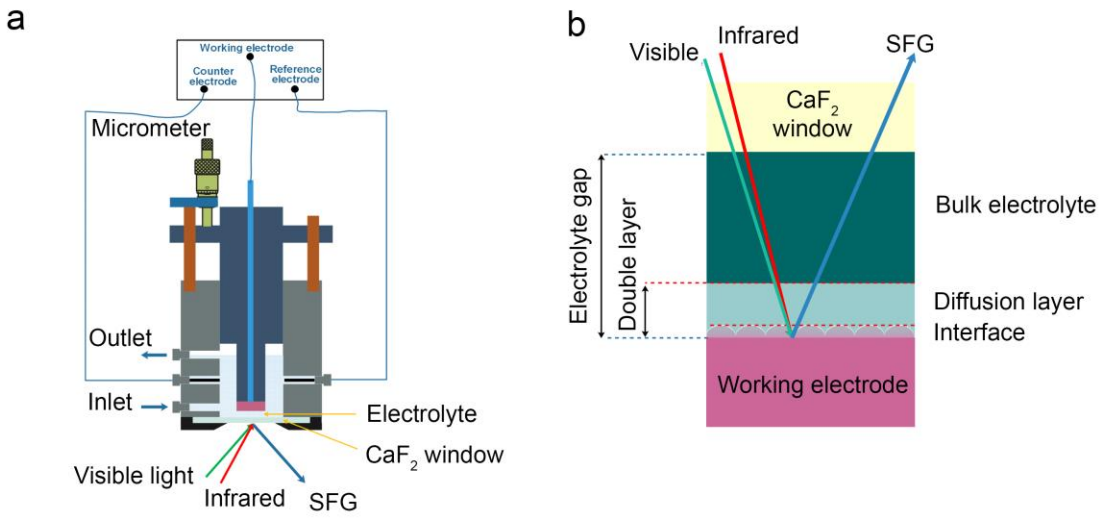

Figure 1.10 (a) Schematic of the *in situ* SFG-electrochemical setup. (b)Simplified model for the electrified interface probed by SFG.

Kutz et al first applied broadband SFG spectroscopy to study the reaction pathways of ethanol electrooxidation on polycrystalline Pt catalysts in alkaline and acidic electrolyte. In acidic electrolyte, adsorbed acetate and co-adsorbed sulfuric acid anions were observed. Since SFG can differentiate the bands between ^{12}CO and ^{13}CO, isotopically labeled ethanol ($^{12}CH_3{}^{13}CH_2OH$) was employed and the results showed that the methyl fragment ($-^{12}CH_x$) produced far less ^{12}CO, and therefore suggested that the methyl group was reduced to methane and/or appeared to be stable (inactive) on the Pt surface in acidic and alkaline electrolyte. On the other hand, the results suggested that ^{12}CO could be detected at unusually high potentials, indicating methyl-like species CH_x was difficult to be oxidized.[143, 161] To effectively employ SFG spectroscopy to study the reaction

mechanism of an electrochemical process, other reaction intermediates such as η^2-acetaldehyde, η^2-acetyl, ethylidyne, monodentate acetate, methoxy, tertiary methanol derivative, *COH residue, η^2-formaldehyde, mono and bidentate formate, $*CH_3$ and $*CH_2$ residues were identified by Gomes et al.[160]

1.6.5 MASS SPECTROMETRY (MS)

In additional to *in situ* Raman and IR spectroscopies, online mass spectrometry was also utilized by electrochemists to analyze the products and intermediates involved in electrode reactions. In the early seventies, electrochemical mass spectrometry (EMS) only for the analysis of gaseous reaction products was first invented by Bruckenstein.[162] However, the rise time (the time from the generation of the products to the response of the mass spectrometer) of the mass intensity was too long (about 20 seconds). Later, Wolter et al improved the configuration and technique to reduce the rise time of the mass intensity to 1 second, allowing the measurement of the time derivative of the amount of species produced (namely the rate of formation).[163] Therefore, this method was called differential electrochemical mass spectrometry (DEMS). Additionally, sufficient fast time response allowed the mass intensity of a product to be measured as a function of the applied potential analogous to cyclic voltammetry, called mass spectrometric cyclic voltammetry (MSCV). In the past several decades, many new types of DEMS setup were developed based on conventional design to be used for different detecting conditions including the thin layer cell allowing the use of massive electrodes,[164, 165] the dual thin layer cell for continuous flow through of electrolyte,[166] rotating electrode inlet system[167, 168] and the pinhole inlet system[169, 170]. The DEMS cell could be a static cell[171] or flow cell[172] depending on the requirement of the design as shown in **Figure 1.11**. Also, some

special DEMS designs worked for CO_2 measurement in an electrochemical full cell system with wide temperature window[173] and in both acidic and alkaline solutions[174].

The key part of the DEMS is the membrane inlet system connecting the electrochemical cell to the high vacuum system of mass spectrometer as shown in **Figure 1.11** a. If the porous working electrode is together with the membrane, the volatile products generated on catalyst will be transported through the membrane to the vacuum system of the mass spectrometer. If the working electrode is separated from the membrane, the volatile products generated on the catalyst first diffuse into the thin layer and then are transported through the membrane to the vacuum system of mass spectrometer, resulting in longer response time caused by slow diffusion in the liquid as shown in **Figure 1.11** c. Through calibration by known species, these products can be detected quantitatively, and thus the faradaic current of the desired products can be calculated. Hence, detailed kinetic information such as the current efficiency and Tafel slope of the generation of products can be obtained. But only the volatile species can be detected such as carbon dioxide and acetaldehyde during the EOR, so the less volatile species such as acetic acid as a main product will be largely overlooked.

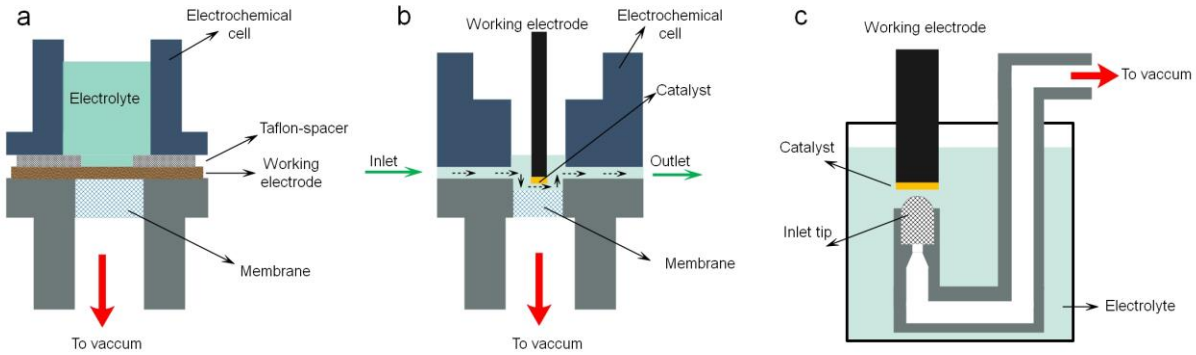

Figure 1.11 (a) DEMS with the inlet membrane back of the catalyst. (b) DEMS with a thin layer cell in flow system. (c) DEMS with a pinhole inlet

1.7 MOTIVATION, GOALS AND OBJECTIVES OF STUDY

One bottleneck of the implementation of the DEFCs is the lack of a cost-effective catalyst for the EOR, the anode reaction of DEFCs, which suffers from slow kinetics and poor selectivity toward CO_2 generation. Therefore, it is very important to develop efficient anode catalysts to oxidize ethanol completely into CO_2 and hence achieve a twelve-electron transfer, compared with partial oxidation of ethanol to acetaldehyde/acetic acid with only a two-/four-electron transfer, respectively.

Carbon-supported Pt is one of the most studied catalysts for EOR. However, various spectroscopic measurements have shown that Pt has slow kinetics for generating CO_2 through breaking the C-C bond of ethanol. The main products of EOR on the Pt surface are acetic acid and acetaldehyde.[33, 44, 175, 176] Even though a small portion of ethanol undergoes C-C bond splitting on Pt, resulting C_1 fragments, e.g. CH_x and CO, poison active sites on the Pt surface because of their strong interaction with Pt, impeding the subsequent adsorption of ethanol and/or oxidation of reaction intermediates, and hence slow down the overall charge transfer rate drastically.[177-179] Efforts to improve the reactivity (charge transfer rate) and selectivity (CO_2 generation) of the EOR, including the formation of binary or ternary Pt-based catalysts and the investigation of other types of catalysts beyond Pt (e.g., Ir and Pd), have been reported.[138, 180, 181]

Among various studies, improved C-C bond splitting over Pt by formation of ternary Pt/Rh/Sn catalysts has been reported, pioneered by the research from Adzic's group.[78, 119, 120, 160, 182] It is generally accepted that a synergetic effect among Rh, Pt and Sn contributes to the supremacy of Pt/Rh/Sn toward EOR. In such a ternary system, Pt strongly dehydrogenates the ethanol molecules and resulting reaction intermediates, Rh

facilitates C-C bond splitting via promoting β-hydrogenation of ethanol, and oxophilic Sn promotes the dissociative adsorption of water to form adsorbed OH (*OH) on the catalyst surfaces to assist the oxidization of the reaction intermediates.

Despite the extensive theoretical and experimental work that has been carried out for studying the EOR on various catalysts, a clear understanding of the inhibiting factors for CO_2 generation remains unclear. This can be attributed to, at least partially, the complexity of the reaction pathways and reaction environments of the EOR for realistic computational modeling. For example, theoretical studies of rate-limiting steps for the EOR show some controversies. Some research work suggests the rate-limiting step depends on the surface: on Pt (111) surface C-C bond splitting is the rate-limiting step during EOR, while on Rh (111) surface β-dehydrogenation of $*CH_3CH_2O$, the dissociative product of ethanol, is the rate-limiting step.[182] Computational results from work by Sheng *et al* and Sutton *et al* have also demonstrated that Rh supported on Pt (111) is a better model catalyst than Pt (111) for C-C bond splitting, a rate-limiting step for the EOR.[134, 183] Notably, Hu *et al* have intensively studied CO_2 generation on various platinum-group-metal surfaces using DFT calculations,[134, 179] showing that although Pt is a sufficiently active catalyst for CO_2 production, the EOR is in fact limited by *CO removal on the surface.[179]

On the other hand, the lack of clear understanding of CO_2 generation and selectivity can also be attributed to experimental difficulty in characterizing the atomic structure of the catalysts and detecting CO_2 generation. For example, various spectroscopic techniques have been used to understand the reaction mechanism of the EOR via qualitatively detecting the species adsorbed on catalyst surfaces and/or diffused into bulk

solution. Through those studies, acetic acid, acetaldehyde and carbon dioxide have been identified qualitatively as main products of the EOR, along with various reaction intermediates as *CO, *CH_3CHO, and *CH_x.[78] Quantitative analyses of CO_2 generation and selectivity have been conducted using FTIR analysis through integrating the signal intensity of each species.[20, 133] However, the measurements often suffer from the interference of CO_2 diffused into bulk solution and the neglecting of byproducts generation except acetic acid and acetaldehyde. In addition, DEMS has been applied to analyze quantitatively CO_2 current efficiency (CCE), quantified as the ratio between the current generated during the complete oxidation of ethanol into CO_2 and the overall current of the EOR.[86, 176, 184, 185] However, the signal of CO_2 overlaps with that of CH_3CHO (m/z = 44). The analysis of a particular fragment CO_2^{2+} (m/z = 22) is typically used to estimate the CO_2 generation with less signal intensity.[184] Moreover, FTIR and DEMS often provide controversial results for the CCE, which vary from 0.08% to 40% under similar reaction conditions.[77, 86, 133, 184, 186, 187]

Regardless of the many spectroscopic studies reported previously, the underlying reason behind the low CO_2 selectivity during the EOR is still missing. Comprehensive understanding of the electrokinetics of CO_2 generation and therefore the reaction pathway for CO_2 formation via C-C bond-breaking is not only a fundamental question for electro-catalysis, but also a key technological challenge since practical implementation of DEFC technology is contingent on its ability to selectively oxidize ethanol into CO_2 to achieve exceptional energy density through a 12-electron transfer reaction. Different from FTIR and DEMS, a CO_2 microelectrode reported here has a minimal detectable CO_2 concentration of 0.2 μM, and a high resolution of data acquisition of five seconds.

Moreover, its CO_2 signal is not affected by the presence of acetaldehyde and acetic acid in typical experimental conditions as our previous studies showed.[66]

With the help of high quality CO_2 signal obtained from such a microelectrode, the comprehensive electro-kinetic details of CO_2 generation via C-C bond-breaking will be revealed. Hence, in this study, we combine the uniquely advantageous motif of a CO_2 microelectrode with the well-characterized, electrocatalytic advantages of ultrafine Pt-SnO_2 and PtRh-SnO_2 core-shell nanoparticles with sizes ranging from 2 to 3 nm, in order to study the activity and selectivity of the EOR, and thus understand the underlying mechanism of CO_2 generation via C-C bond breaking. Specifically, the use of ultrafine Pt-SnO_2 and PtRh-SnO_2 core-shell nanoparticles (2 to 3 nm) not only maximizes the surface-to-volume ratio of the catalyst, but also provides rational comparison with commercial carbon supported Pt (ETEK) which has the same size range. Moreover, the role of each component in EOR will be clarified and the potentiodynamics effects will be investigated resulting from various *OH formation on different metal sites at different potential regions.

CHAPTER 2

EXPERIMENTAL METHODS

2.1 SYNTHESIS OF CATALYSTS

2.1.1 SYNTHESIS OF $PtRhO_x$-SnO_2 CATALYSTS WITH PARTIALLY OXIDIZED PtRh CORES

A two-step process was used to synthesize $PtRhO_x$-SnO_2 core-shell particles. SnO_2 colloids were first synthesized. In a typical synthesis, 66.6 mg of $SnCl_2$ (Alfa Aesar, 99%) was initially dissolved in 20 mL of ethylene glycol (EG, Mallinckrodt Chemicals) with 2mL of deionized water. $SnCl_2$ solution was heated up to 180 °C in an open-air environment from room temperature (25 °C) for a duration of 1 hour. Cooling water jacket was applied to keep the water and EG in the reaction flask. After an hour of the reaction at 180 °C, the reaction is cooled to room temperature, the SnO_2 colloids were stored for the later use. The ratio of between Pt and Sn was fixed at 1:1 based on our previous work. Here, catalysts with different composition were synthesized by tuning the ratio between Pt and Rh. In a typical synthesis of $Pt_{37}Rh_{20}$-$(SnO_2)_{43}$ nanoparticles, $NaPtCl_4 \cdot xH_2O$ (0.06 mmol, 27.6 mg, Alfa Aesar, 99.95%) and $K_3RhCl_6 \cdot xH_2O$ (0.03 mmol, 13.3 mg, Alfa Aesar) were dissolved in the 1.5 mL of EG at room temperature, respectively. These two solutions were mixed together then injected into 8 mL of preheated SnO_2/EG solution (0.06 mmol SnO_2 colloids). The reaction proceeded for 30 min with stirring of 500 rpm under argon flow. These Pt/Rh/Sn nanoparticles were dispersed in the solution homogenously. To

prepare the carbon-supported catalysts, carbon black (87.7 mg, Vulcan XC-72) was added to the $Pt_{37}Rh_{20}O_x$-$(SnO_2)_{43}$ solution with vigorous stirring for 1 hour at room temperature. The resulting mixture was washed thoroughly with acetone and 95% ethanol and then the final product was collected after centrifugation. At last, the precipitation was dried in vacuum at room temperature, denoted as $Pt_{37}Rh_{20}O_{21}$-$(SnO_2)_{43}$/C with partially oxidized core and SnO_2 shell determined by several techniques. Similarly, the synthesis of Pt/SnO_2 followed the same procedure except for the addition of K_3RhCl_6. The nominal metal loadings were kept as 20 wt% (20% metal and 80% carbon by mass).

2.1.2 SYNTHESIS OF PtRh-SnO_2 CATALYSTS WITH Pt-Rh METALLIC CORE

The catalysts with metallic cores were obtained by the reduction of the catalysts with partially oxidized core in a tube furnace (Thermo scientific, Lindberg Blue/M) at 250 °C for 2 hours under Argon (95%)/H_2 (5%) flow. The resulting material was denoted as $Pt_{37}Rh_{20}$-$(SnO_2)_{43}$/C with metallic core and SnO_2 shell.

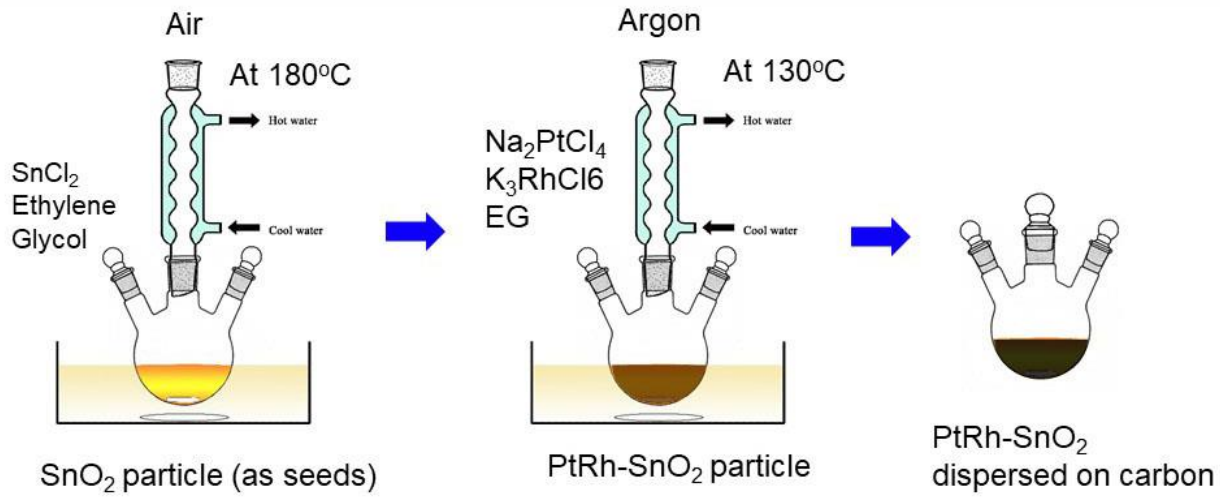

Figure 2.1 Synthetic route of carbon supported Pt/Rh/Sn nanoparticles

2.2 STRUCTURAL CHARACTERIZATIONS

2.2.1 TRANSMISSION ELECTRON MICROSCOPY

Regular transmission electron microscopy (TEM) images were collected on the Zeiss/LEO 922 Omega transmission electron microscope operated at 120 keV at the University Instrumentation Center at the University of New Hampshire in Durham, New Hampshire. The sample is exposed in the bright field with the magnification up to 100, 000. Image acquisition and analysis were performed using Gatan Digital Micrograph and ImageJ software. The statistical size calculation is based on the analysis of at least 200 particles.

High-resolution transmission electron microscopy (HRTEM) was used to define the edges of nanoparticles to obtain more accurate size distribution. The HRTEM images of all the nanoparticles were taken using a FEI Titan 80-300 microscope at 300 kV at the Center for Functional Nanomaterials (CFN) at the Brookhaven National Laboratory (BNL) in Upton, New York.

2.2.2 SCANNING TRANSMISSION ELECTRON MICROSCOPY COUPLED WITH ELECTRON ENERGY LOSS SPECTROSCOPY

High-angle annular dark-field (HAADF) scanning transmission electron microscope (STEM) images and electron energy loss spectroscopy (EELS) measurements were performed and collected using an aberration-corrected Hitachi HD 2700C equipped with a modified Gatan Enfina ER spectrometer at the Center for Functional Nanomaterials at the Brookhaven National Laboratory. STEM could focus the electron beam onto a narrow spot and scan the targeted area. Combed with EELS probe, the distribution of element in

targeted area could be obtained. The probe size was around 0.8 ~ 1.3 angstrom and the beam intensity on the sample varied from 100 to 200 pA depending on the testing conditions. The cold field emission gun gave an energy resolution of 0.35 eV. And the convergence angle was usually 27 mrad and the ADF and EELS collection angles were 45~242 and 20 mrad, respectively. The dwelling time for each pixel was about 10 s for the better EELS acquisition.

2.2.3 ENERGY DISPERSIVE SPECTROSCOPY

The energy dispersive X-ray spectroscopy (EDXS) was used to analyze the composition of the Pt/Rh/Sn and Pt/Sn particles by surveying 5 spots on the specimen. The sample holder was fully covered by samples with ~1 mm thickness. The EDXS is Tescan Lyra3 GMU Combined FE-SEM/FIB field emission microscope, operated 10 kV at the UIC.

2.2.4 SYNCHROTRON X-RAY POWDER DIFFRACTION

Synchrotron X-ray powder diffraction (XRD) patterns were collected at beamline 17-BM-B ($\lambda = 0.072768$ Å) of the Advanced Photon Source at Argonne National Laboratory. The resolution is $\Delta E/E = 1.5\times10^{-4}$. The two-theta angle shown in the main text was based on the wavelength of 1.54056 Å through the Bragg's law：

$$2d\sin\theta = n\lambda \qquad 2.1$$

where d is the lattice distance, n is a positive integer, θ is the angle of the incident wave and λ is the wavelength of the incident wave.

Through the Scherrer equation, the particle size of crystals can be calculated. The Scherrer equation can be written as

$$d = \frac{K\lambda}{\beta \cos\theta} \qquad 2.2$$

where d is the mean size of the crystalline domains; K is a dimensionless shape factor, typically 0.9; λ is the wavelength of X-ray in nanometer; β is the width at half the maximum intensity of the peak selected for calculation, in radians; and θ is the Bragg angle of the selected peak.

2.2.5 X-RAY ABSORPTION SPECTROSCOPY (XAS)

The XAS experiments were conducted at beam lines X18B at the National Synchrotron Light Source, Brookhaven National Laboratory. The samples were prepared by pressing 20~30 mg of carbon supported catalyst powders into disk shape pellets with a hydraulic press. The pellets were placed between respective ion chambers for data collection in transmission mode. The XAS measurements were carried out at the Pt L_3-edge (11564 eV), Rh K-edge (23220 eV) and Sn K-edge (29200 eV). Metal foils (Pt, Rh and Sn) and metal oxide powder (PtO_2, Rh_2O_3 and SnO_2) were used as references for X-ray energy calibration and data alignment. The IFEFFIT package was used to perform XAS data processing and analysis.

XAS is a technique that provides element specific information on the electronic and structural properties. It contains the information for the structure in the vicinity of the edge named as X-ray absorption near-edge structure (XANES). The oscillations above edge extended to 1000 eV or more named as extended X-ray absorption fine structure (EXAFS) as shown in **Figure 2.2**. The XANES region reflects the oxidation state and geometry,

and the EXAFS region can provide surrounding information of the target atoms, such as bond length and coordination number.

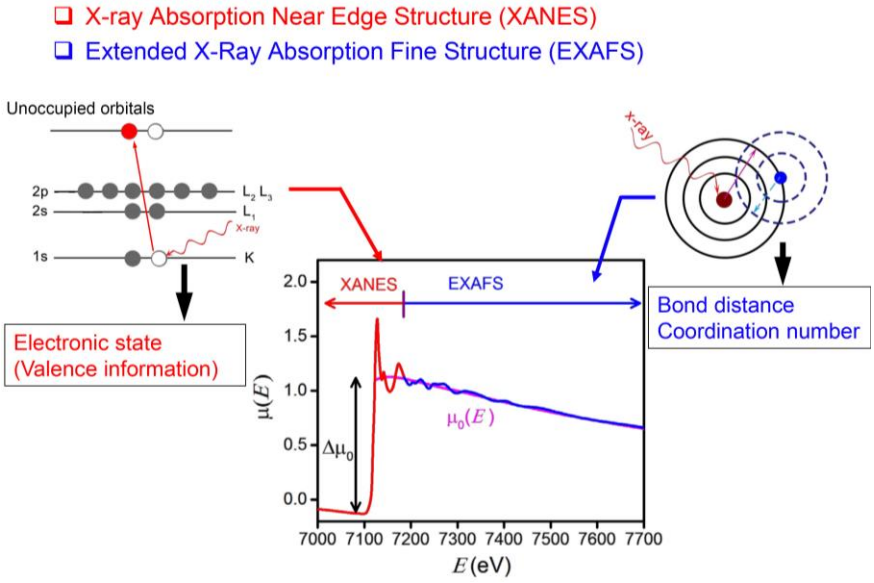

Figure 2.2 Schematic representations of XANES and EXAFS regions in X-ray aborption spectrum.

2.3 ELECTROCHEMICAL TESTS

2.3.1 CV AND CA TESTS IN THE THREE ELECTRODE HALF CELL

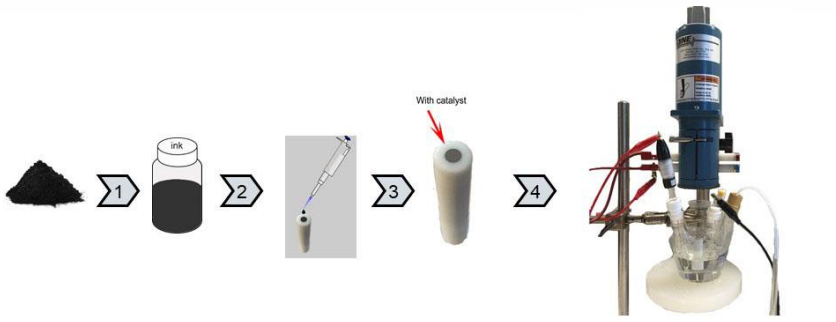

Figure 2.3 Procedure of the test in a three electrode half cell.

Only one cycle of CV was measured in a 0.5 M H_2SO_4 electrolyte for the electrochemically active surface area (ECASA) measurements under narrow potential

window between -0.2 and 0.3 V so that the catalyst would be neither reduced at low potential ranges nor oxidized at high potential ranges.

After ECASA measurements, 232.8 µL of ethanol was added into the electrolyte to form a 0.5 M ethanol solution. CV measurements were conducted a scan rate of 0.5 mV/s from 0.1 to 1.1 V (vs. Ag/AgCl) to test the EOR performance, while the CO_2 signals were collected *in situ* every 5 seconds through the CO_2 microelectrode. We studied the influence of *OH on CO_2 formation in the half-cell system using a CHI 660 single channel electrochemical workstation (CH Instruments). A three-electrode system was employed, which contains a working electrode which is a glassy carbon rotating disk electrode (RDE), a platinum wire counter electrode, and an Ag/AgCl (4 M KCl) reference electrode. The RDE working electrode (WE) was controlled at a rotation rate of 1000 rpm throughout the study. Catalyst ink was prepared by dispersing 10 mg catalyst into 5 ml of deionized water (18.2 MΩ · cm). The homogeneous catalyst ink was prepared through sonication of the dispersion and 10 µL of the well-mixed ink suspension was drop-casted onto the glassy carbon working electrode and vacuum dried. Upon drying, 10 µL of Nafion solution with volume ratio of 0.5% (volume ratio: V_{Nafion}/V_{Water} = 0.05 mL: 10 mL, Nafion 117 purchased from Aldrich) was added to cover the catalyst. Before the electrochemical test, the 0.5 M sulfuric acid (99.999%, Sigma-Aldrich) electrolyte was purged with argon for at least 30 minutes. Linear scanning voltammetry was first conducted from -0.22 to 0.28 V (vs Ag/AgCl) at a scan rate of 50 mV/s. Secondly, a chronoamperometry measurement was conducted for 30 minutes at 1.0 V. After that, 3 consecutive cycles of CV were conducted between -0.22 and 0.28 V.

2.3.2 ELECTROCHEMICALLY ACTIVE SURFACE AREA (ECASA) MEASUREMENT

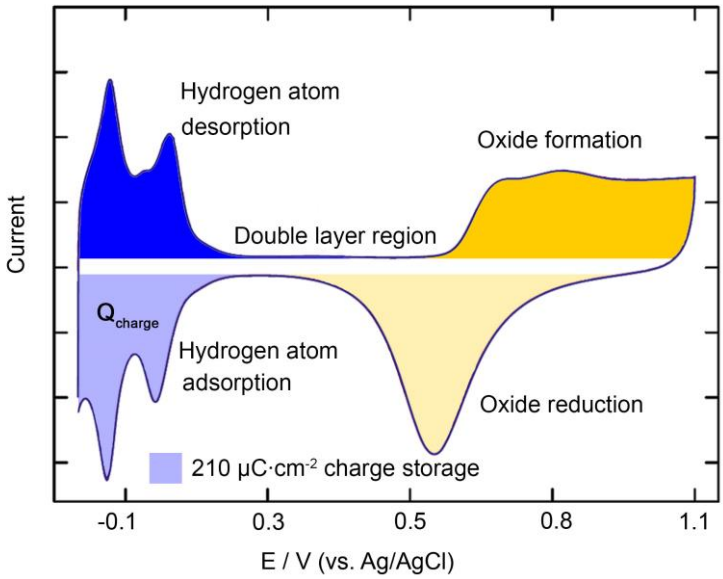

Figure 2.4 Electrochemically active surface area (ECASA) of a typical Pt catalyst

Figure 2.4 shows a typical CV curves of Pt nanoparticle in sulfuric acid electrolyte including: hydrogen atom adsorption/desorption region, double layer region, and Pt oxide formation/reduction region. H_{upd}(hydrogen underpotentially deposition)-based ECASA values were calculated by integrating the CV in the hydrogen atom adsorption region. Here the assumption is each Pt surface atom adsorbs one hydrogen atom, so the theoretical Q_{charge} value is 210 μC/cm^2 based on a one-electron transfer.

Take the Pt/C as an example for the ECASA calculation. Firstly, to integrate the shaded area (current × time) to calculate the charge Q_{charge} as shown in **Figure 2.4**. Secondly, the ECASA can be calculated by using the following equation

$$ECASA\left(H_{UPD}\right)\left(m^2 \cdot g^{-1}\right) = \frac{Q_{Charge}\left(C\right)}{210\left(\mu C \cdot cm^{-2}\right) \times m_{Pt}\left(g\right)} \times 100 \qquad 2.3$$

when we calculate the ECASA (cm^2/g), only the mass (g) of noble metals such as Pt and Rh in Pt/SnO_2 and $Pt/Rh/SnO_2$ have been considered. It is generally accepted that the conversion factors of Pt and Rh for hydrogen adsorption are very similar.[188] Therefore, we use the factor of 210 $\mu C/cm^2$ for calculating the contribution of the Rh to hydrogen absorption.

2.3.3 *OH ADSORBATES FORMATION EXPERIMENT

The influence of *OH on the EOR was conducted by a three-electrode half-cell system using a CHI 660 single channel electrochemical workstation (CH Instruments). The three-electrode system contains a glassy carbon rotating disk electrode (RDE, diameter of the disc: 5.0 mm) as a working electrode, a platinum wire counter electrode, and an Ag/AgCl (4 M KCl) reference electrode. Catalyst ink was prepared by dispersing 10 mg of the catalysts into 5 ml of deionized water (18.2 MΩ · cm). The homogeneous catalyst ink was prepared through the sonication, and 10 µL of the well-mixed ink suspension was drop-casted onto the glassy carbon working electrode and vacuum dried. After that, 10 µL of Nafion solution with volume ratio of 0.5% (volume ratio: V_{Nafion}/V_{water}= 0.05 mL: 10 mL, Nafion 117 purchased from Aldrich) was added to cover the catalysts. And the resulting working electrode was dried in vacuum prior to the final electrochemical half-cell test. In a typical test, the RDE working electrode was controlled at a rotation rate of 1000 rpm. The 100 mL of 0.5 M sulfuric acid (99.999%, Sigma-Aldrich) electrolyte was first added to the electrochemical cell, and then the working electrode was mounted, and a rotation rate of 1000 rpm was applied and maintained throughout the test. Before starting the test, the electrolyte was purged with argon for at least 30 minutes. After that, one LSV was first conducted from -0.2 to 0.3 V (vs Ag/AgCl) at a scan rate of 50 mV/s. And then, CA

measurement was conducted for 30 minutes at 1.0 V, followed by 3 consecutive cycles of CV conducted between -0.2 and 0.3 V. The schematic procedure is shown in **Figure 2.5**. During the electrochemical tests, argon gas was purged throughout the test.

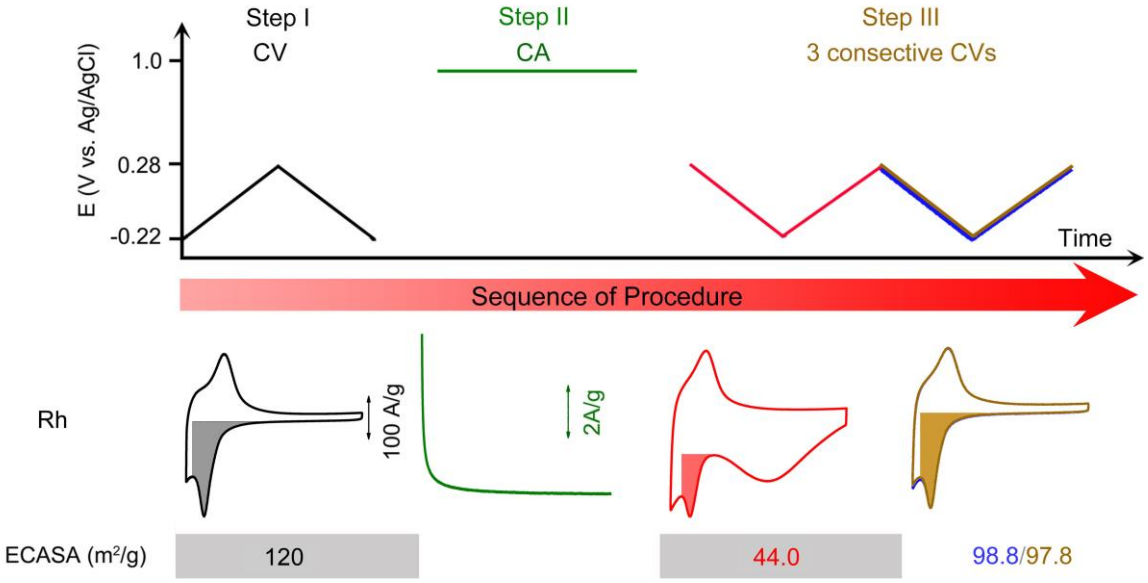

Figure 2.5 *OH adsorbates on commercial Rh/C(Premetek).

2.4 *IN SITU* CO_2 MEASUREMENTS

The catalyst slurry was prepared by mixing catalyst powder (4 mg) with ethanol (1 ml, 190 proof) and a small amount of Nafion 117 solution (5 μL, Aldrich). Through drop-casting, a thin layer of catalyst (~ 2.0 mg) was deposited on the platinum foil (working electrode). 8 ml of 0.5 M H_2SO_4 (99.999%, Sigma-Aldrich) electrolyte was placed in the reactor before applying the test procedure. The CO_2 microelectrode was calibrated with standard 0.5% and 1% CO_2 gases in N_2 (Airgas) before every measurement. The electrolyte was bubbled with argon for 1h before testing, and the electrolyte was protected by argon during measurements. One cycle of cyclic voltammetry (CV) was performed in argon-purged 0.5 M sulfuric acid electrolyte scanning from -0.2 to 0.3 V (vs. Ag/AgCl) at

a scan rate of 20 mV/s to calculate the electrochemically active surface areas (ECASAs). More detailed information is described in Chapter 3.

2.5 DENSITY FUNCTIONAL THEORY (DFT) CALCULATIONS

All density functional theory calculations were performed with the CP2K package by the collaborator Prof. Deskins at the Worcester Polytech institute.[189-191] The PBE exchange correlation functional[192] was used and a k-point mesh consisted only of the Γ point. Valence electrons were modeled by a double-zeta Gaussian basis set,[193] while core electrons were treated by Goedecker-Teter-Hutter pseudopotentials.[194, 195] CP2K is a periodic code, so the slab approach was used to model several catalysts. A Pt(111) surface with a [6×6] cell that was four layers deep (144 total Pt atoms) was modeled. Calculations were non-spin-polarized except when species with unpaired electrons were involved. Test results showed differences between spin-polarized and non-spin-polarized calculations to be small (< 0.04 eV). Then the C-C bond breaking over various surfaces was modeled for potential intermediates, CH_3CO, CH_2CO, and CHCO ($*CH_xCO \rightarrow *CH_x + *CO$). These three species have all been proposed key intermediates for C-C bond breaking.[179, 182, 183, 196-198] Due to the large number of reactions and surfaces, activation energies were calculated with the linear scaling method of Wang et al.[199] This method was developed for metal surfaces, and may not strictly hold for complex systems, such as metal oxide/metal interfaces. Nonetheless we hold the assumption that more negative reaction energies will produce lower activation barriers, and this linear scaling method provides a qualitative way to easily compare different surfaces.

To model interfaces between Pt and SnO_2, or PtRh and SnO_2, the “rod” approach was used, as described in Molina et al.[200] We used a similar approach in previous work[66]. This approach forms an interface between a metal rod and metal oxide support, with (111) facets exposed on the metal rod. Such facets are the most stable surface of Pt, and this rod represents a potential Pt-SnO_2 interface. A three-layer (9 atomic layers) SnO_2 surface with dimensions of 13.7 Å and 16.4 Å, or [5×2], (180 atoms) was used as a support for either Pt or PtRh rods. The Pt-SnO_2 and PtRh-SnO_2 systems had 216 total atoms. The atoms in alloys may arrange in several possible ways, such as well mixed, or with a preference of one atom type for different surface locations. To consider these different cases we modeled three different PtRh-SnO_2 systems: one with Rh atoms on a (111) facet, one with Rh concentrated away from the SnO_2 surface, and one with Rh more evenly distributed through the alloy. The PtRh rods had 18 Pt atoms and 18 Rh atoms in DFT calculations. Over all the surfaces adsorption of different species at many different initial sites was modeled. Only the final, most stable results are presented herein.

CHAPTER 3

DEVELOPMENT OF FOUR-ELECTRODE CELL FOR *IN SITU* CO_2 MEASUREMENT

3.1 INTRODUCTION

To date, *in situ* FTIR and DEMS are the most commonly used techniques in detecting CO_2 generation during the electrochemical test. *In situ* FTIR is powerful for analyzing products qualitatively. Quantitative measurement can also be achieved by integrating the signal intensity during *in situ* FTIR. But the accuracy of the quantitative calculation determined by the ratio of signal/noise of the products of interest. The most important limitation is to obtain an accurate calibration curve for each species. So only the relative ratio of CO_2 to byproducts is available.

DEMS can obtain the absolute amount of each product. But in the electro-oxidation of ethanol, the products including carbon dioxide, acetaldehyde and acetic acid limited the use of DEMS. Issues are listed: (i)The strongest signal (m/z =44) of CO_2 overlaps with the signal of CH_3CHO. The unique signal of CO_2 is CO_2^{2+} (m/z =22) different from CH_3CHO (CH_3CHO^+, m/z=44), but it is too weak to be used as quantitative analysis. (ii) Acetic acid is less volatile, so its signal is underestimated by DEMS.

Since FTIR and DEMS can be applied in different reactor designs, the former is generally a static cell while the latter is a flow cell in many cases. Results do not always agree with each other very well. CO_2 current efficiency in terms of DEMS were 2.7% by Wang et al,[176] 0.8% by Colmeanares et al[187], 3.5% by Cantane et al[77], 0.08% by

Bergamaski et al[186], 5% by Delpeuch et al[86] and ~40% by Rao et al[184] in 0.1 M ethanol solution. However, they were ~10% by Camara et al[44] and ~12% by Li et al[133] in terms of FTIR.

A flow cell is usually used for DEMS measurement to reduce the contact time of intermediates weakly adsorbed on the catalyst surface, probably preventing the further oxidation to CO_2. Also, Chen et al stated that the mass signal of CO_2 varied dramatically with different ethanol concentrations, indicating that this technique still had limitation for accurate analysis in this system even after the signal correction.[201]

We reported the design of a four-electrode electrochemical cell for monitoring the CO_2 concentration *in situ,* where the interference of acetaldehyde and acetic acid can be neglected. However, only P_{CO2} as a function of time for CA measurements was achieved. However, P_{CO2} of potential-dependency is unknown. We updated the design to measure P_{CO2} as a function of the electrical potential.

3.2 DESIGN OF THE FOUR-ELECTRODE ELECTROCHEMICAL CELL

The *in situ* CO_2 measurement system contains a Pt foil working electrode (width× length: 15 mm × 15 mm), a Pt foil counter electrode (width× length: 2 mm × 20 mm), an Ag/AgCl (3 M KCl) reference electrode (RE, MI 402, Microelectrodes), and a CO_2 microelectrode (Model MI-720, Microelectrodes Inc.), which is called a four-electrode electrochemical cell as shown in **Figure 3.1**. The catalyst slurry was prepared by mixing catalyst powder (4 mg) with ethanol (1 mL, 190 Proof, Pharmco Aaper) and a small amount of Nafion 117 solution (5 µL, Aldrich). Through drop-casting, a thin layer of catalyst (~2.0 mg) was deposited on the platinum foil (working electrode). The

electrochemical cell was firmly supported by a stand. The working electrode was located on the center of the Teflon support, the edge of which was fixed by the top Teflon ring. The CO_2 microelectrode was connected to the stand via a tubular adapter and mounted to the electrochemical cell. By controlling the distance between the working electrode and the stand, as well as the distance between the CO_2 microelectrode and the stand, the distance between working electrode and microelectrode can be accurately tuned and kept as 1 mm during the EOR measurements.

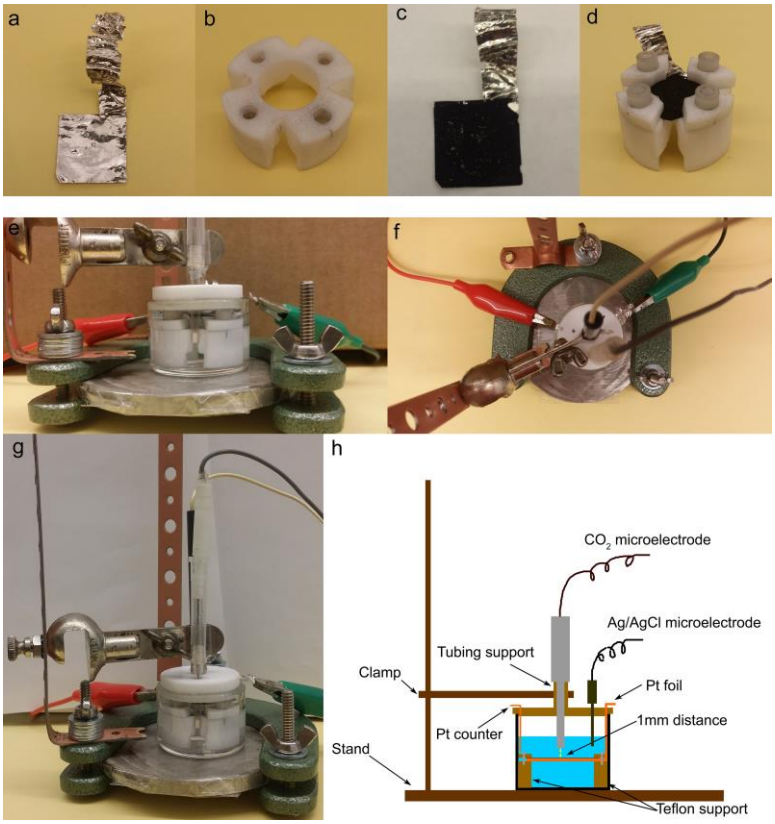

Figure 3.1 (a) Clean Pt foil. (b) Teflon support. (c) Pt foil with catalyst layer as the working electrode. (d) The working electrode sandwiched by the Teflon support and covers. (e) Front view and (f) top view of the *in situ* CO_2 measurement cell. (g) The real picture of the *in situ* CO_2 measurement cell. (h) The schematic of the *in situ* CO_2 measurement

3.3 EFFECTS OF POSITION OF CO_2 ELECTRODE AND STIRRING ON CO_2 SIGNAL

In general, the well-stirred reactor is ideal for kinetic analysis due to the homogenous concentration of products without diffusion limitation. But in the current CO_2 microelectrode system, the concentration of CO_2 was too dilute to be detected precisely if CO_2 distributed evenly in solution in a well-stirred system. The experiment was conducted on the Pt/C commercial catalyst for EOR at a constant potential. The distance between the CO_2 microelectrode and the catalyst surface was fixed at 1 mm. When the CO_2 signal was steady which is normalized as 1 without stirring, and then magnetically stirring was applied at 1000 rpm. CO_2 signal showed a quick decrease and finally down to 0.015 as shown in **Figure 3.2** a.

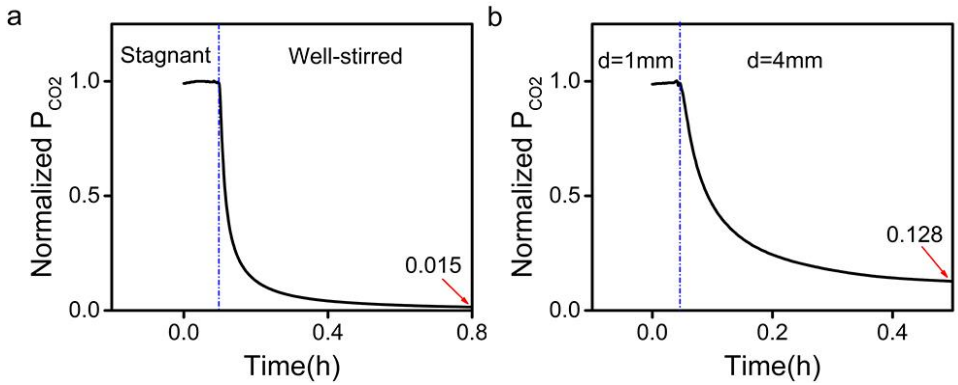

Figure 3.2 (a) The effects of stagnant and well-stirred system on CO_2 signal at the distance of 1mm, (b) the effects of distance between the CO_2 microelectrode tip and the catalyst surface on CO_2 signal.

Similarly, when the CO_2 signal reached steady state at 1 mm (distance between the catalyst and the CO_2 microelectrode) without stirring, lifting the CO_2 microelectrode up to 4 mm resulted in a sharp decrease in CO_2 signal, equivalent to an 87.2% loss as shown

in **Figure 3.2** b. To obtain strong CO_2 signal for further kinetic analysis, the distance between the CO_2 microelectrode and the catalyst surface was fixed at 1 mm and the reaction was kept in a stagnant condition.

3.4 CALCULATION OF CO_2 CONCENTRATION AT THE ELECTRODE SURFACE

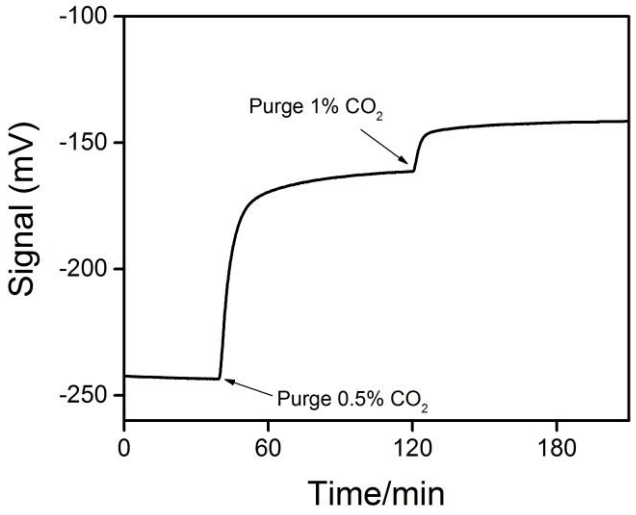

Figure 3.3 Procedure to obtain working curve of CO_2.

Before the calculation of CO_2 concentration, the working curve was required. First, the solution was purged with argon to remove air dissolved in aqueous phase until the steady state (The reading of signal does not change within 1 minute). Then, 0.5% CO_2 gas was purged until the steady state. Last, 1.0% CO_2 gas was purged until the steady state as shown in **Figure 3.3**. The electric signal (mV) of the CO_2 microelectrode is proportional to the CO_2 partial pressure (P_{CO2}). According to the working curve, P_{CO2} of interest can be

calculated. And the concentration of CO_2 in solution can be calculated by the conversion formula:

$$S = \frac{a}{22.414} \times \frac{760 - P_{water}}{760} \times \frac{r\%}{100} = \frac{a}{22.414} \times \frac{P_{CO_2}}{760} \quad 3.1$$

where P_{CO_2} is the partial pressure of CO_2 in mm of Hg, S is the concentration of CO_2 (mol/L), a is the absorbtion coefficient of CO_2 at the temperature listed in the Appendix table (0.759 at 25 ^oC), P_w is the vapor pressure of water at the temperature listed in **Appendix table**.

To calculate the CO_2 concentration at the catalyst surface, we build a mass transfer partial differential equation.

$$\frac{\partial c}{\partial t} = D\frac{\partial^2 c}{\partial z^2} \quad 3.2$$

where $D_{CO_2-H_2O} = 1.92 \times 10^{-5} cm^2 \cdot s^{-1}$

Within every 5 seconds, the following assumptions can be made (1) constant concentration at the Pt surface; (2) no leakage at the boundaries; (3) steady state.

It becomes

$$0 = D\frac{\partial^2 c}{\partial z^2} \quad 3.3$$

with the following boundary conditions (B.C.)

$$\text{B.C.1: } z = 0\ mm, \quad c = c_0 \quad 3.4$$

$$\text{B.C.1: } z = 7\ mm, \quad c = 0 \quad 3.5$$

The concentration at 1 mm is known, so the concentration profile in every 5 seconds is solved as

$$c = Az + B \quad 3.6$$

where

$$A = -\frac{1}{6}c_1 \quad \text{and} \quad B = \frac{7}{6}c_1 \tag{3.7}$$

Here the CO_2 concentration at 1 mm is known, so the concentration of CO_2 at the working electrode is

$$c_0 = \frac{7}{6}c_1 \tag{3.8}$$

Integrating each concentration curve with respect to z and then multiplying the cross-section area (geometric area of working electrode) gives the total amount of CO_2:

$$N_{CO_2} = S\int_0^7 \int_{c_0}^{0} dcdz$$

$$= \frac{1}{2} \times \underbrace{\frac{7}{6}c_1\left(mol \cdot L^{-1}\right)}_{\substack{CO_2 \text{ concentration} \\ \text{at working electrode}}} \times \underbrace{7mm}_{\text{Depth of solution}} \times \underbrace{15mm \times 15mm}_{\text{Area of working electrode}}$$

$$= 0.919 \times 10^{-3} c_1 \left(mol\right) \tag{3.9}$$

Once the total generation of CO_2 can be obtained, the total charges to form CO_2 from ethanol can be calculated

$$Q_{CO_2} = \underbrace{6}_{\substack{\text{Number of} \\ \text{charge transfer}}} \times \underbrace{0.919 \times 10^{-3} c_1}_{\text{Mole of } CO_2} \times \underbrace{6.022 \times 10^{23}}_{\text{Avogadro constant}} \times \underbrace{1.602 \times 10^{-19}}_{\text{area of working electrode}}$$

$$= 532 c_1 \left(C\right) \tag{3.10}$$

Based on the known curve of charge (Q_{CO2}) from CO_2 generation versus time, we could take derivative for Q_{CO2} with respect to time, thus the CO_2 generation rate j_{CO2} was obtained:

$$j_{CO_2} = \frac{dQ_{CO_2}}{dt} \tag{3.11}$$

Hence the CO_2 selectivity (S_{CO2}) can be obtained as follows.

$$j_{Total} = current\ for\ generating\ all\ of\ proucts\left(CO_2, CH_3CHO, CH_3COOH, etc\right)$$

$$= measured\ overall\ current \qquad 3.12$$

$$S_{CO_2} = \frac{CO_2\ generation\ rate}{byproducts\ generation\ rate}$$

$$= \frac{current\ from\ generating\ CO_2}{current\ from\ generating\ byproducts}$$

$$= \frac{j_{CO_2}}{j_{Total} - j_{CO_2}} \qquad 3.13$$

3.5 EFFECT OF THE PLATINUM FOIL AS THE SUPPORT FOR MEASUREMENT

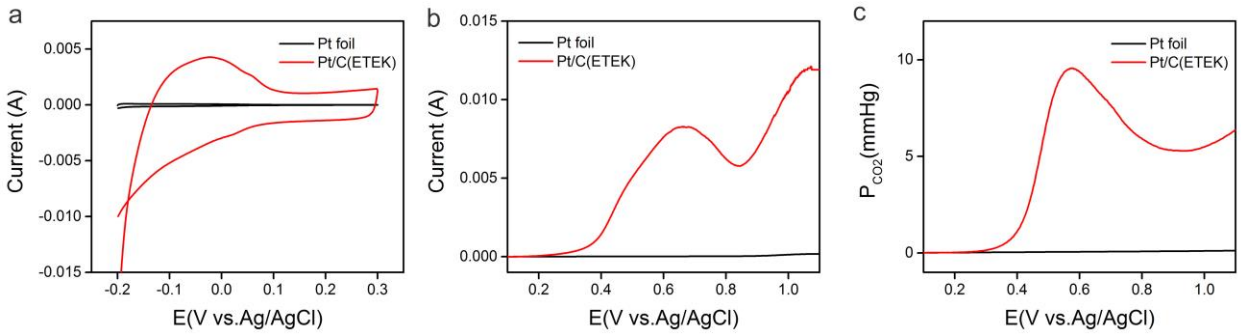

Figure 3.4 (a) CV curves of Pt foil and 1.5 mg Pt/C(ETEK) from -0.2 to 0.3 V at the scan rate of 20 mV/s in 0.5 M H_2SO_4 solution; (b) CV curves of Pt foil and Pt/C(ETEK) from 0.1 to 1.1 V at the scan rate of 0.5 mV/s in 0.5 M H_2SO_4 /0.5 M ethanol solution; (c) Partial pressure curves corresponding to CVs shown in (b).

Here we choose Pt foil as the working electrode to support nanoparticle catalysts, but Pt metal is electrocatalytically active for EOR. To confirm that the electrical current and CO_2 signal obtained during the electrochemical oxidation of ethanol were primarily

resulting from catalyst materials instead of platinum foil substrate, the blank experiment was conducted using platinum foil without active material as shown in **Figure 3.4**. The comparison between the blank platinum foil and the platinum foil fully covered with Pt/C catalyst shows that the former only contributed ~3% to surface area, ~1.5% to overall current and ~2% to CO_2 signal when the Pt foil was completely exposed to the electrolyte. Considering nearly complete surface of Pt foil was covered by the carbon supported catalysts, the contribution of the Pt foil toward the current and CO_2 signal is expected to be far below 1.5%.

3.6 DISCUSSION

In this chapter, we designed an *in situ* CO_2 measurement four-electrode cell using a CO_2 microelectrode as a sensor. Considering the transport issue of CO_2 in the electrolyte from the catalysts interface to the CO_2 sensor, the effects of position of CO_2 microelectrode and the type of reactor (with/without stirring) were investigate. Through the design, the distance between the interface of the electrocatalyst and the CO_2 probe was controlled in the range of mm level. The result shows that closer distance generates stronger CO_2 signals. Because of the small amount of CO_2 products, the stirring reactor cannot present reliable signals due to so diluted CO_2 concentration.

Through a reasonable approximation, the CO_2 concentration can be calculated at the surface of the electrocatalyst. Thereafter, the CO_2 generation rate and the CO_2 selectivity can be obtained in terms of a series of formulas.

CHAPTER 4

THE EFFECT OF LATTICE OXGEN ON CO_2 GENERATION ON PLATINUM-RHODIUM-TIN OXIDE CATALYSTS

4.1 INTRODUCTION

EOR via the C-C bond-cleavage pathway leads to the production of CO_2 through a complete oxidation of ethanol with a twelve-electron transfer, while cleavages of C-H, O-H and/or C-O bonds without C-C bond cleavage lead to incomplete oxidation with the production of acetaldehyde (two-electron transfer) or acetic acid (four-electron transfer).[35, 44, 176, 202-204]

Bi-phase PtRh-SnO_2 materials with a PtRh alloy and a segregated SnO_2 phase have been synthesized for EOR,[78, 117-122] due to the lower energy barrier in the presence of Rh.[134] The intermediates after the C-C bond splitting can be oxidized by oxygenated species on the catalyst surface (OH_{ads}) on Sn sites adjacent to Pt and Rh sites. [62] Attributed to this bifunctional effect, Pt/Rh/Sn ternary catalysts have been generally considered as the most effective materials towards EOR, especially at higher overpotential. However, fuel cells generally tend to operate at an external potential close to their equilibrium potential. At low overpotential at the anode, the Pt/Rh/Sn components have a weak dissociative adsorption of water, and the resulting low OH_{ads} coverage on the catalyst surface may not be adequate to remove the strongly adsorbed reaction intermediates especially CO that poisons the active sites. Therefore, finding an optimal catalytic structure that can effectively dissociate ethanol via C-C splitting at low

overpotential and consequently remove the CO intermediates is of great importance for the implementation of DEFC technology.

In the past decade, studies have shown that the kinetics of the CO oxidation reaction on surfaces of Ru, Pt, Pd, Rh and PtRh increases significantly in conjunction with the formation of a thin oxide film on the surface of metal or alloy catalysts.[205-209] It has been found that the active phase for CO oxidation is oxidized rather than metallic. Although these results obtained from solid/gas phase reaction are expected to be relevant for general heterogeneous catalysis, reactivity of noble metal oxides towards electro-catalysis, especially EOR, has not been well studied. Particularly, most of the studies on Pt-based EOR catalyst have only focused on non-noble metal oxides, such as SnO_2 and CeO_2.[210] However, the role of Pt or Rh oxides on the electro-kinetics of EOR, especially C-C splitting, has not been reported.

Table 4.1 Summary of the structural properties of different PtRhSn catalysts

Catalysts	EDS (Pt:Rh:Sn) molar ratio[a]	Size(nm)[b]	Size(nm)[c]
$Pt_1/Rh_{0.25}/Sn_1$_Reduced	39:12:49	5.4±1.3	4.4
$Pt_1/Rh_{0.25}/Sn_1$_As-made		2.6±0.6	2.7
$Pt_1/Rh_{0.5}/Sn_1$_Reduced	37:20:43	6.5±2.3	3.5
$Pt_1/Rh_{0.5}/Sn_1$_As-made		2.8±0.9	2.6
Pt/C(ETEK)	100:0:0	2.7±0.6	2.7

a.Molar ratio of PtRhSn by EDS analysis; b. Calculated by TEM images statistically; c. calculated by XRD patterns based on (220) plane.

4.2 STRUCTURAL CHARACTERIZATION OF PLATINUM-RHODIUM-TIN OXIDE MATERIALS

The molar ratio between Pt and SnO_2 was kept as 1:1, while ratio between Pt and Rh varied from 2:1 to 4:1. **Table 4.1** summarizes the results from energy-dispersive X-ray spectroscopy measurement of the resulting catalysts, confirming the atomic ratio of Pt:Rh:Sn as 37:20:43, and 39:12:49.

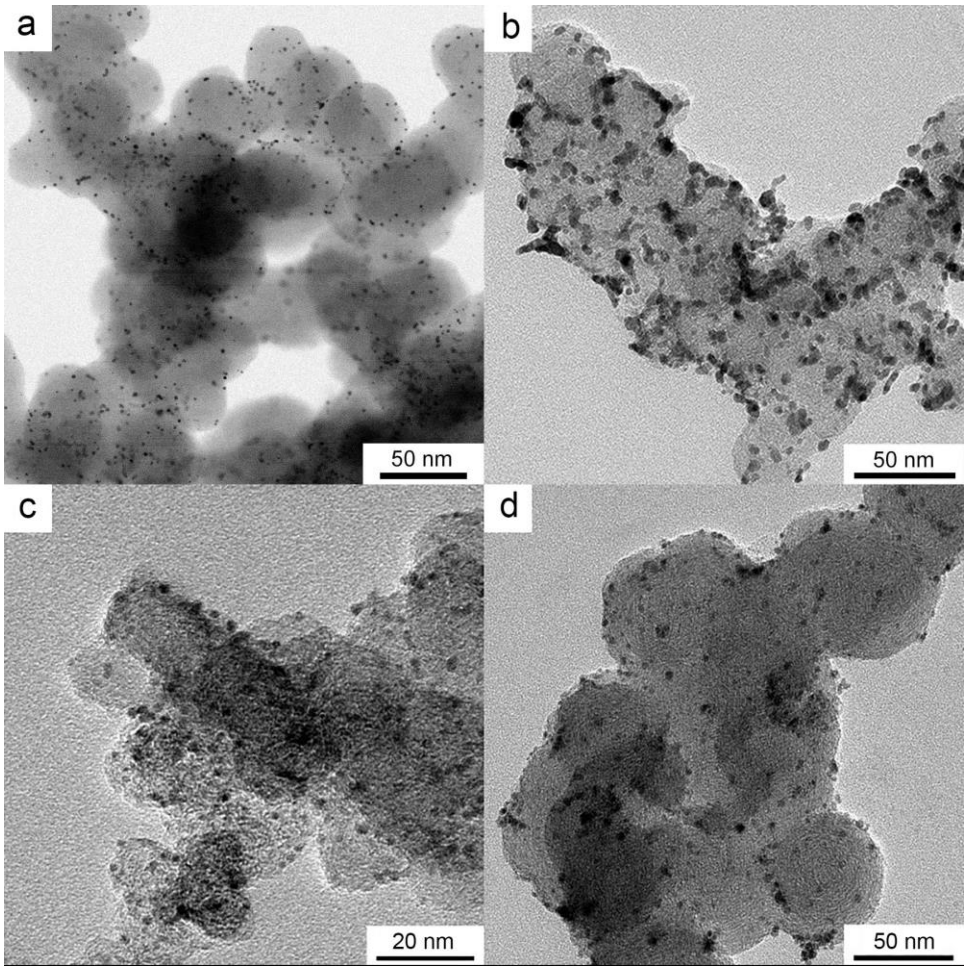

Figure 4.1 TEM images of (a) $Pt_{37}Rh_{20}O_x$-$(SnO_2)_{43}$/C, (b) $Pt_{37}Rh_{20}$-$(SnO_2)_{43}$/C, (c) $Pt_{39}Rh_{12}O_{21}$-$(SnO_2)_{49}$ and (d) $Pt_{39}Rh_{12}$-$(SnO_2)_{49}$.

Figure 4.1 shows transmission electron microscopy (TEM) images of as-made and reduced carbon supported $Pt_{37}/Rh_{20}/Sn_{43}$ and $Pt_{39}/Rh_{12}/Sn_{49}$ nanoparticles with average sizes of 2.8±0.9 nm, 6.5±0.9 nm, 2.6±0.6 nm and 5.4±1.3 nm, respectively. The large size of the reduced samples was due to coalescence of nanoparticles during the thermal treatment in H_2/Ar flow at 250 ^oC.

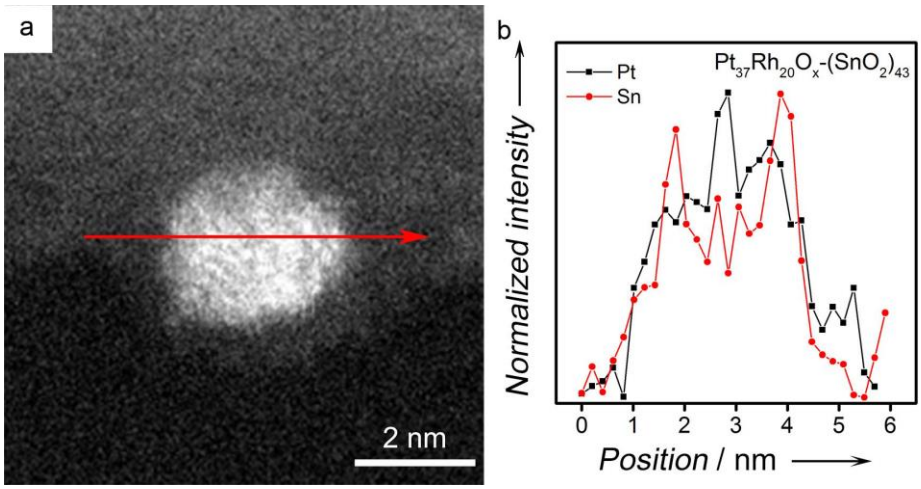

Figure 4.2 (b) EELS line scan across $Pt_{37}Rh_{20}O_x$-$(SnO_2)_{43}$ particle as indicated by the arrow in (a)

Figure 4.2 shows the scanning transmission electron microscope-electron energy loss spectroscopy (STEM-EELS) line scans of a typical as-made $Pt_{37}/Rh_{20}/Sn_{43}$ particle. Data show that Sn displayed strong signal at the edges of the particle, while Pt displayed strong signal in the center. The data provide unambiguous evidence of the core-shell structure with a Pt-core-rich and Sn-shell-rich heterogeneous structure at the atomic scale. The ionization energy of the Rh $M_{4/5}$ edge is in the range from 307 to 312 eV of energy loss, which is unfortunately overlapped by the residual signal from carbon K edge. Therefore, the EELS line scan was unable to measure the distribution of Rh within the catalysts, though the EDS spectra showed the existence of Rh with appropriate chemical composition close to the ratio of the precursors.

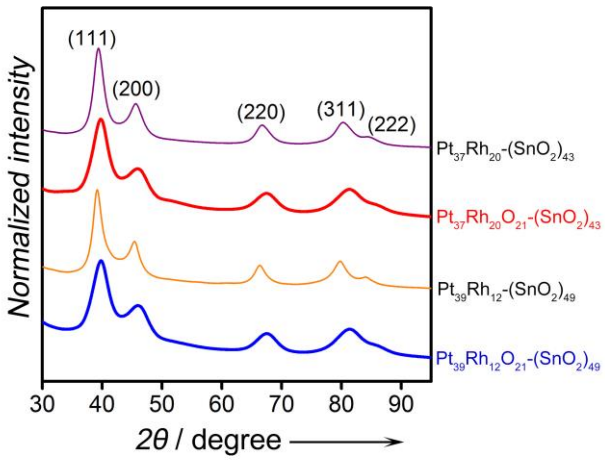

Figure 4.3 XRD patterns of carbon-supported $Pt_{37}Rh_{20}$-$(SnO_2)_{43}$, $Pt_{37}Rh_{20}O_{21}$-$(SnO_2)_{43}$, $Pt_{39}Rh_{12}$-$(SnO_2)_{49}$, and $Pt_{39}Rh_{12}O_{21}$-$(SnO_2)_{49}$.

Figure 4.3 shows the XRD patterns of carbon-supported $Pt_{37}Rh_{20}$-$(SnO_2)_{43}$, $Pt_{37}Rh_{20}O_{21}$-$(SnO_2)_{43}$, $Pt_{39}Rh_{12}$-$(SnO_2)_{49}$, and $Pt_{39}Rh_{12}O_{21}$-$(SnO_2)_{49}$. The diffraction peaks of around 39.5º, 45.9º, 67.2º, 81.8º and 86.0º were assigned to the (111), (200), (220), (311) and (222) planes, respectively, corresponding to a face centered cubic (FCC) structure, suggesting the formation of the cubic structure. The average sizes were calculated to be 2.6 nm, 3.5 nm, 2.7 nm, and 4.4 nm for $Pt_{37}Rh_{20}$-$(SnO_2)_{43}$, $Pt_{37}Rh_{20}O_{21}$-$(SnO_2)_{43}$, $Pt_{39}Rh_{12}$-$(SnO_2)_{49}$, and $Pt_{39}Rh_{12}O_{21}$-$(SnO_2)_{49}$, respectively, by the Scherrer equation, which are similar to the sizes obtained from TEM images. Diffraction peaks of SnO_2 were not observed in as-made or reduced samples, although the STEM-EELS line scan showed Sn-rich shell in both samples. This could be attributed to the fact that Sn or SnO_2 existed in the form of very small nanoparticle or of an amorphous phase.

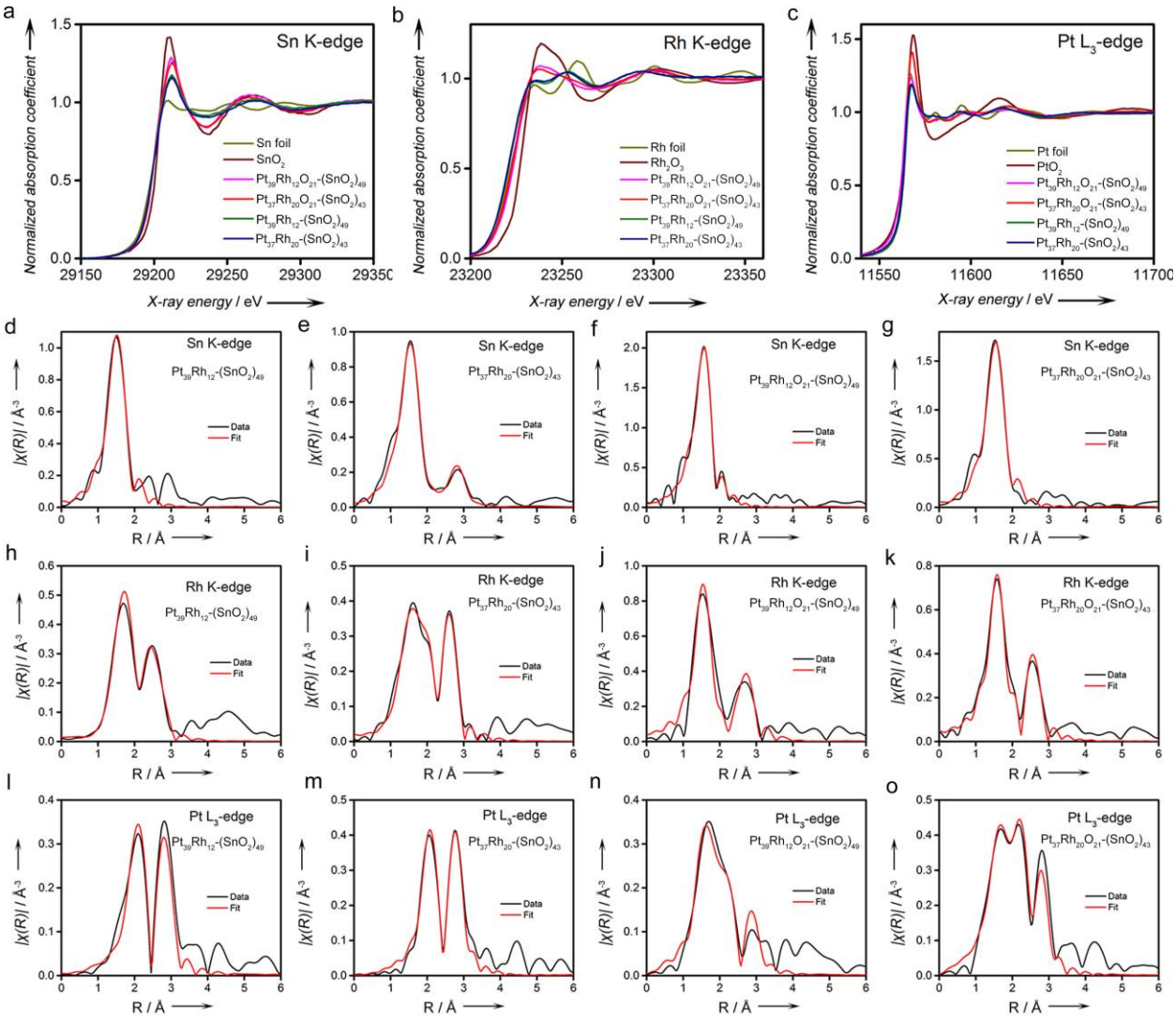

Figure 4.4 XANES data of (a) Sn K edge, (b) Rh K edge, and (c) Pt L_3 edge. And EXAFS fitting curves for the as-made and reduced catalysts: (d, e, f and g) Sn K-edge; (h, i, j and k) Rh K-edge; and (l, m, n and o) Pt L_3-edge.

X-ray absorption (XAS) measurements were used to investigate the electronic states and local atomic environment of the Pt, Rh and Sn in the as-made and reduced $Pt_{37}/Rh_{20}/Sn_{43}$ catalysts. **Figure 4.4** shows the XAS data of K-edges of Sn and Rh, and L_3-edge of Pt of Pt/Rh/Sn catalysts, together with the standard materials such as metallic Sn, Pt and Rh foils, as well as their oxides SnO_2, PtO_2 and Rh_2O_3. **Figure 4.4** a shows

that the Sn K-edge data of the as-made and reduced Pt/Rh/Sn were very similar to those of SnO_2, suggesting that Sn was predominantly oxidized in all Pt/Rh/Sn samples. Combined with the structural information obtained from the STEM-EELS line scan, it has been suggested that SnO_2 primarily existed as a shell in both as-made and reduced samples.

Table 4.2 EXAFS fitting results of Pt/Rh/Sn catalysts

	Pt foil	Rh foil	Sn foil	SnO_2	$Pt_{39}Rh_{12}$-$(SnO_2)_{49}$	$Pt_{39}Rh_{12}O_{21}$-$(SnO_2)_{49}$	$Pt_{37}Rh_{20}$-$(SnO_2)_{43}$	$Pt_{37}Rh_{20}O_{21}$-$(SnO_2)_{43}$
N_{Pt-Pt}	12				3.7 ± 1.4	5.6 ± 1.7	3.7 ±0.5	7.4±1.5
N_{Pt-Rh}					2.69		2.5	
N_{Pt-O}						0.9 ±0.3		1.2 ±0.5
N_{Rh-Rh}		12			2.8 ± 1.2	1.6 ± 1.4	4.7 ±1.1	1.7±1.1
N_{Rh-Pt}					8.8 ± 3.2		4.6 ± 0.6	
N_{Rh-O}					0.83±0.34	2.7 ± 0.8	0.9 ±0.6	2.2 ±0.6
N_{Sn-Sn}			4	2			5.8 ± 2.5	
N_{Sn-O}				6	2.8± 0.5	5.1 ±0.5	3.3±0.4	4.9 ±0.5
R_{Pt-Pt} (Å)	2.764± 0.003				2.73±0.02	2.68 ± 0.02	2.73±0.01	2.67 ± 0.01
R_{Pt-Rh}(Å)					2.72±0.03		2.72±0.01	
R_{Pt-O}(Å)						2.00 ±0.02		1.99 ±0.02
R_{Rh-Rh}(Å)		2.685± 0.002			2.65±0.03	2.83 ±0.03	2.68±0.01	2.80±0.03
R_{Rh-O}(Å)					2.00±0.04	2.06 ±0.03	1.96±0.02	2.07±0.02
R_{Sn-Sn}(Å)			3.001± 0.004				3.10 ± 0.05	
R_{Sn-O}(Å)				2.03±0.0 1	2.03 ±0.01	2.045±0.008	2.05±0.01	2.05± 0.01

On the other hand, the Pt L_3- and Rh K- edge absorption data suggested that Pt and Rh had very different electronic structures between the reduced and the as-made

samples (**Figure 4.4** b and c). For the reduced samples, Pt and Rh existed as predominantly a metallic phase, evidenced by the similar white line (the intense peak at the K absorption edge) compared with their metal foil counterparts. For the as-made catalysts, Pt and Rh data resembled those of PtO_2 and Rh_2O_3 indicating the existence of oxidized phases, though there were still discernable metallic Pt and Rh phases observed in both as-made samples.

The Fourier transform magnitudes of extended X-ray absorption fine structure (EXAFS) data and theoretical fits for Pt, Sn and Rh of Pt/Rh/Sn catalysts are shown in **Figure 4.4** and **Table 4.2**. For the reduced sample, the obtained first-nearest-neighbor Pt-metal (N_{Pt-M}= N_{Pt-Pt} + N_{Pt-Rh}) and Rh-metal (N_{Rh-M}= N_{Rh-Rh} + N_{Rh-Pt}) coordination numbers all had reasonably similar values within the uncertainties (6.2 ± 0.5 and 9.3 ± 1.6, respectively). That fact, and the other observation that the Pt-Rh and Rh-Pt contributions were required for both Pt and Rh edge analyses, in addition to the Pt-Pt and Rh-Rh contributions, respectively, demonstrated unambiguously the formation of a Pt-Rh alloy. For the as-made sample, however, Pt and Rh appeared to be the segregated phases without alloy formation, evidenced by the fact that only Pt-Pt ($N_{Pt–Pt}$ = 7.4 ± 1.5) and Rh-Rh ($N_{Rh–Rh}$ =1.7 ± 1.1) coordinations had been observed without Pt-Rh and Rh-Pt coordinations. Moreover, discernable Pt-O and Rh-O coordinations indicated the existence of oxidized Pt and Rh phases. Strong Pt-Pt and Rh-Rh coordinations, weak but discernable Pt-O and Rh-O coordinations, and non-detectable Pt-Sn and Rh-Sn coordinations corroborated well the XANES analyses concluding that the as-made $Pt_{37}/Rh_{20}/Sn_{43}$ catalysts were comprised of partially oxidized Pt and Rh cores.

Independent evidence towards similar conclusions could be concluded from the information of bond distances. **Table 4.2** indicates that Pt and Rh exists mainly in the metallic phase in the reduced $Pt_{37}/Rh_{20}/Sn_{43}$ sample, compared with the as-made one. In the former sample, the Pt-Pt bond distance (2.73 ± 0.01 Å) and the Rh-Rh bond distance (2.68 ± 0.01 Å) are more similar to that in a pure Pt (2.764 ± 0.003 Å) and Rh (2.685 ± 0.002 Å). In the as-made sample, the Pt-Pt bond distance (2.67 ± 0.01 Å) and Rh-Rh bond distance (2.80 ± 0.03 Å) are rather different from pure metallic Pt and Rh. Meanwhile, the strong Sn-O coordination from both the as-made and the reduced sample suggested the formation of tin oxide clusters, confirmed by the results obtained independently from STEM-EELS and XANES.

Therefore, we concluded the coexistence of bi-phase throughout the reduced $Pt_{37}/Rh_{20}/Sn_{43}$ catalyst expressed as $Pt_{37}Rh_{20}$-$(SnO_2)_{43}$: homogenous alloys core containing Pt and Rh, and SnO_2 clusters segregated on the shell; while the as-made sample showed a tri-phase feature expressed as Pt_{37}-Rh_{20}-O_x-$(SnO_2)_{43}$: partially oxidized Pt and Rh core with segregated Pt and Rh phases, and SnO_2 clusters on the shell. Similar structural details can also be found in as-made and reduced $Pt_{39}/Rh_{12}/Sn_{49}$ catalysts. Moreover, the degree of oxidation (value of x) for both Pt and Rh components in Pt_{37}-Rh_{20}-O_x-$(SnO_2)_{43}$ catalysts can be estimated by the following equation:

$$x = \frac{N_{Pt-O} + N_{Rh-O}}{N_{Pt-Pt} + N_{Rh-Rh}} \times (37 + 20) = \frac{1.2 + 2.2}{7.4 + 1.7} \times 57 = 21 \qquad 4.1$$

where $N_{Pt\text{-}O}$ is the coordinating number of Pt-O from EXAFS fitting data, similarly to $N_{Rh\text{-}O}$, $N_{Pt\text{-}Pt}$, and $N_{Rh\text{-}Rh}$.

Therefore, the exact formula of partially oxidized catalysts can be expressed as Pt_{37}-Rh_{20}-O_{21}-$(SnO_2)_{43}$.

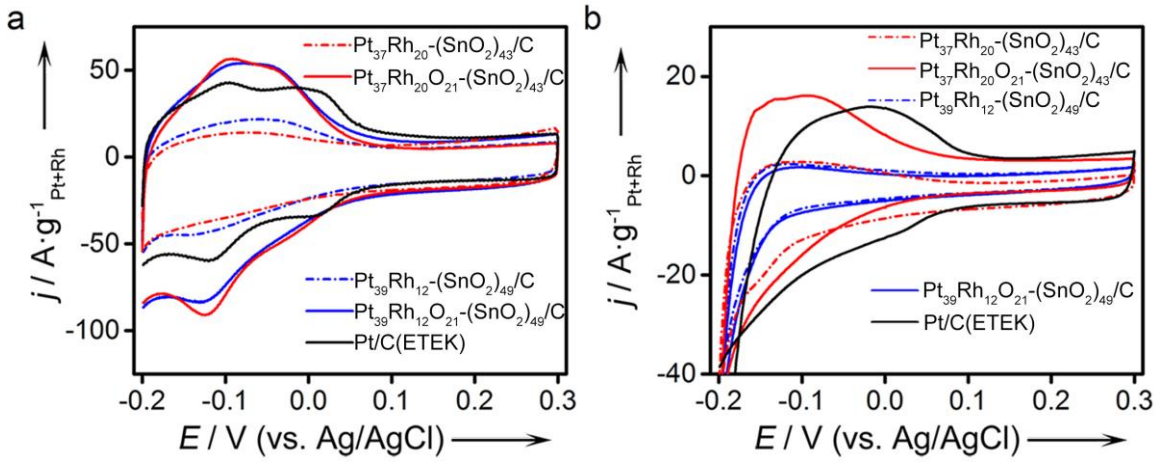

Figure 4.5 CVs of Pt/Rh/Sn catalysts and commercial Pt/C in (a) three-electrode half-cell and (b) four-electrode *in situ* cell.

Table 4.3 Summary of the electrochemical properties of Pt/Rh/Sn catalysts

Catalysts	Half-cell Measurement			CO_2 measurement				
	ECASA (m^2/g PtRh)[a]	j(mA/cm^2)[b]	j(μA/cm^2)[c]	ECASA (m^2/g PtRh)[d]	j(μA/cm^2)[e]	P_{CO2}(mmHg/m^2) at 0.35V	j_{CO2}(μA/cm^2) at 0.35V	Selectivity of CO_2 at 0.35V (%)
$Pt_{39}Rh_{12}$-$(SnO_2)_{49}$/C	43±2.4	0.19±0.04	36±7.8	26±4.5	22±8.7	26±22	0.35	1.6
$Pt_{39}Rh_{12}O_{21}$-$(SnO_2)_{49}$/C	81±3.1	0.18±0.06	39±15	32±6.6	11±5.0	20±13	0.28	2.8
$Pt_{37}Rh_{20}$-$(SnO_2)_{43}$/C	27±3.2	0.31±0.13	74±23	36±7.3	18±5.4	46±24	0.75	4.3
$Pt_{37}Rh_{20}O_{21}$-$(SnO_2)_{43}$/C	87±10	0.12±0.03	26±13	56±10	21±5.4	101±73	2.03	10.2
Pt/C(ETEK)	97±8.5	0.10±0.01	6.9±3.6	61±7.6	3.8±0.08	30±5	0.83	17.9

a. ECASA calculated by H_{upd} area in half-cell reactor; b. Data recorded from CV at 0.35 V vs. Ag/AgCl in half-cell reactor; c. data recorded at 1hr reaction of CA at 0.35 V vs. Ag/AgCl in half-cell reactor; d. ECASA calculated by H_{upd} area in CO_2 measurement reactor; e. Data recorded from CV at 0.35 V vs. Ag/AgCl in CO_2 measurement reactor.

Figure 4.5 shows CVs of Pt/Rh/Sn catalysts and commercial Pt/C in (a) the three-electrode half-cell and (b) the four-electrode *in situ* cell, where the hydrogen electrochemical active surface areas of $Pt_{37}Rh_{20}$-$(SnO_2)_{43}$/C, $Pt_{37}Rh_{20}O_{21}$-$(SnO_2)_{43}$/C, $Pt_{39}Rh_{12}$-$(SnO_2)_{49}$/C, $Pt_{39}Rh_{12}O_{21}$-$(SnO_2)_{49}$/C, and Pt/C(ETEK) catalysts were tested (a) in 0.5 M of H_2SO_4 at the potential scan rate of 50 mV/s in the three-electrode half-cell and (b) at the potential scan rate of 20 mV/s in the four-electrode cell. The surface areas are summarized in **Table 4.3**. The discrepancy of ECASA values is mainly due the different loading of the catalysts. [211] In the four-electrode cell test, the catalyst loading density (~ 0.89 mg/cm^2) was much larger than the one (~ 0.1 mg/cm^2) in the three-electrode system with the rotating disc electrode.

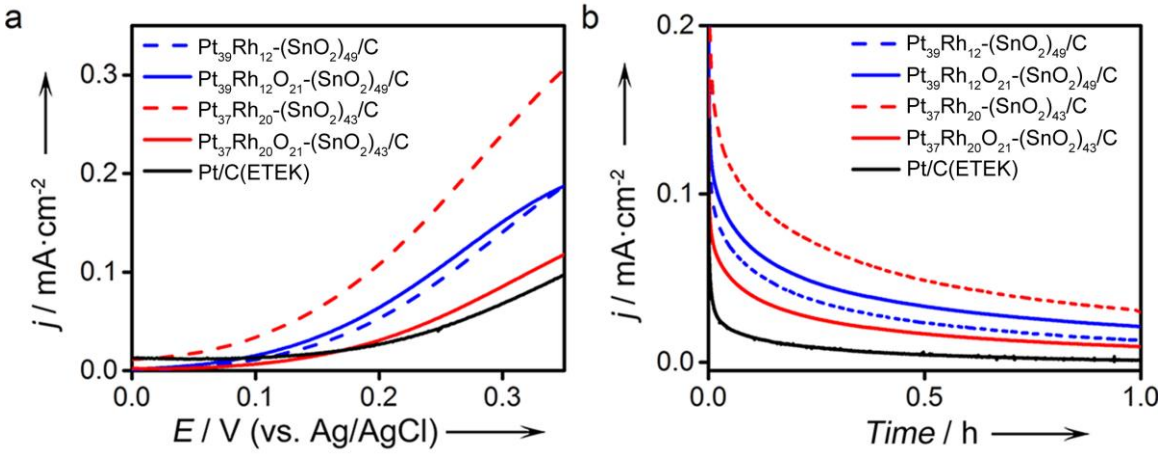

Figure 4.6 Electrochemical measurements in the three-electrode half-cell: (a) CVs from 0 to 0.35 V by the scan rate of 50 mV/s; (b) CAs of catalysts conducted at 0.35 V.

Figure 4.6 a shows the CV analyses of various catalysts measured in 0.5 M H_2SO_4 and 0.5 M ethanol electrolyte at a scan rate of 50 mV/s in the three electrode half cell. Reduced $Pt_{37}Rh_{20}$-$(SnO_2)_{43}$/C catalyst exhibited the superior current density, normalized

by its ECASAs. For $Pt_{37}Rh_{20}Sn_{43}$ catalyst, the current densities at 0.35 V obtained from CVs measurement are shown in **Table 4.3**, following the order as: $Pt_{37}Rh_{20}$-$(SnO_2)_{43}$ > $Pt_{37}Rh_{20}O_{21}$-$(SnO_2)_{43}$ > Pt. The same order was also observed from chronoamperometry (CA) as shown in **Table 4.3** and **Figure 4.6** b. These results indicated that $Pt_{37}Rh_{20}$-$(SnO_2)_{43}$ with a metallic PtRh alloy core increased the overall charge-transfer kinetics of EOR. High current density observed from $Pt_{37}Rh_{20}$-$(SnO_2)_{43}$ catalysts could be attributed to the bi-functional effect (as Pt/Rh atoms provide active sites for dehydrogenation of ethanol, while Sn provide oxygenated species to oxidize the intermediates). Such synergistic interaction made $Pt_{37}Rh_{20}$-$(SnO_2)_{43}$ a better catalyst with fast kinetics for adsorption and dehydrogenation of the ethanol molecule.

4.3 ELECTROKINETICS ANALYSES OF $PtRhO_X$-SnO_2 AND PtRh-SnO_2

CV measurement with a scan rate of 0.5 mV/s was conducted for the EOR using the four-electrode cell. The total amount of CO_2 generation N_{CO2} was then calculated, as well as the generation rate of CO_2. The current density resulting from the generation of CO_2 (j_{CO_2}) is expressed as:

$$j_{CO_2} = \frac{d_{N_{CO_2}}}{dt} \times 6 \times F \qquad 4.2$$

where F is Faraday constant, 6 represents the number of electron transfer upon forming one CO_2 molecule. Finally, selectivity of CO_2 generation is calculated by:

$$S_{CO_2} = \frac{j_{CO_2}}{j_{Total} - j_{CO_2}} \qquad 4.3$$

where j_{Total} is the total current, obtained from CV measurement, which represents the current resulting from the formation of all products.

Many studies have been reported to study the CO_2 generation *in situ* using Fourier transform infrared spectroscopy, differential electrochemical mass spectrometry or gas chromatography,[185, 212] from which the concentrations of CO_2 as a function of potential were presented. However, to our best knowledge, the electro-kinetics details about CO_2 formation, such as CO_2 generation rate and/or selectivity of CO_2 generation have not been reported. Thanks to the high sensitivity (towards CO_2 concentration of 0.2 μM) and short data acquisition time (five seconds) of the CO_2 microelectrode, in this study we were able to provide the comprehensive electro-kinetic details of CO_2 generation via C-C splitting, which has never been reported before.

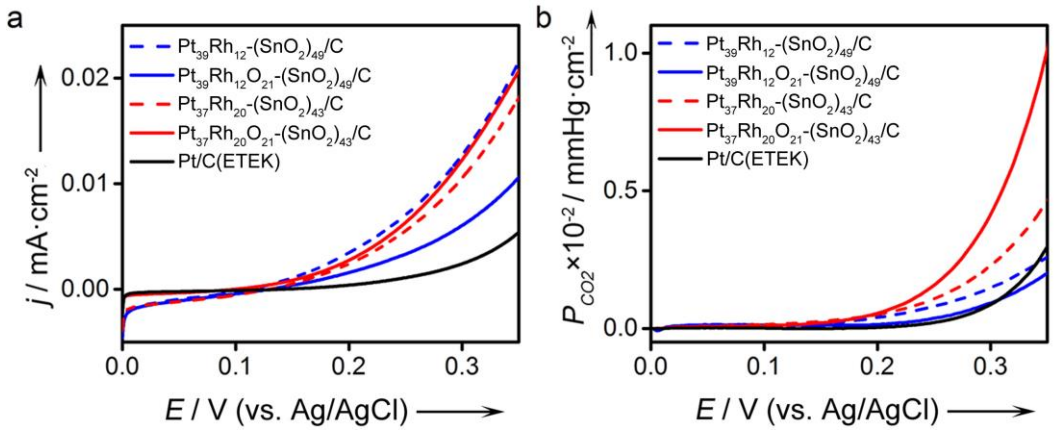

Figure 4.7 (a) Current density and (b) P_{CO2} in the four-electrode electrochemical cell.

Figure 4.7 shows the current density and CO_2 partial pressure of Pt/Rh/Sn catalysts by the scanning rate of 0.5 mV/s from 0 to 0.35 V in the four-electrode *in situ* cell. The electrochemical properties and kinetics analyses for all the catalysts are summarized in **Table 4.3**. Because the $Pt_{37}Rh_{20}O_{21}$-$(SnO_2)_{43}$ catalyst shows the best CO_2 generation,

$Pt_{37}Rh_{20}O_{21}$-$(SnO_2)_{43}$ and its counterpart of $Pt_{37}Rh_{20}$-$(SnO_2)_{43}$ are the focus in the following analysis. **Figure 4.9** shows the CO_2 generation of carbon supported $Pt_{37}Rh_{20}O_{21}$-$(SnO_2)_{43}$, $Pt_{37}Rh_{20}$-$(SnO_2)_{43}$ and Pt (ETEK) catalysts during CV measurements, including (a) partial pressure (P_{CO2}), (b) current density resulting from CO_2 generation (j_{CO2}), (c) onset potential for CO_2 generation, and (d) CO_2 selectivity.

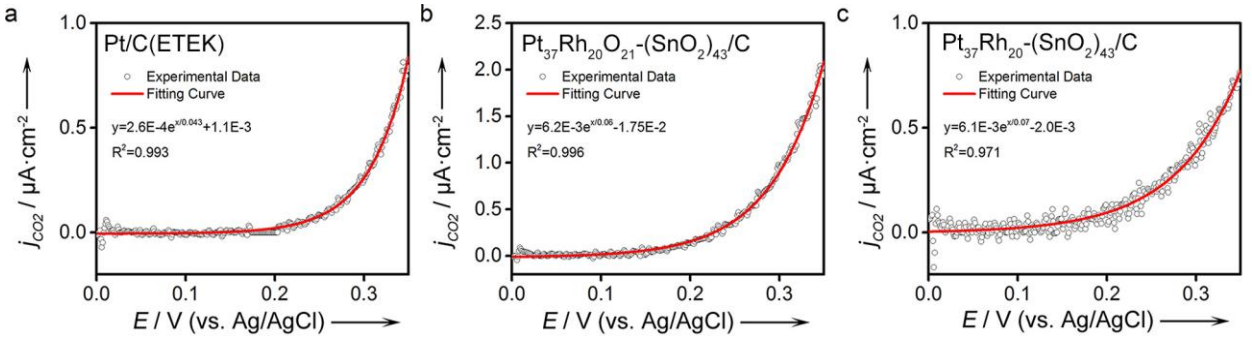

Figure 4.8 Fitting curves of current density from CO_2 generation over (a) Pt/C(ETEK), (b) $Pt_{37}Rh_{20}O_{21}$-$(SnO_2)_{43}$/C, and (c) $Pt_{37}Rh_{20}$-$(SnO_2)_{43}$/C catalysts.

$Pt_{37}Rh_{20}O_{21}$-$(SnO_2)_{43}$ catalysts showed 2.2 and 3.3 times higher P_{CO2}, as well as 2.5 times higher CO_2 generation rate than $Pt_{37}Rh_{20}$-$(SnO_2)_{43}$ and commercial Pt catalysts at 0.35V as shown in **Figure 4.9** b, respectively. Also, onset potential of CO_2 generation for $Pt_{37}Rh_{20}O_{21}$-$(SnO_2)_{43}$, calculated through fitting **Figure 4.8**, was about 37 and 61 mV lower than that of $Pt_{37}Rh_{20}$-$(SnO_2)_{43}$ and commercial Pt as shown in **Figure 4.9** c. **Figure 4.9** d shows that $Pt_{37}Rh_{20}O_{21}$-$(SnO_2)_{43}$ displayed higher CO_2 selectivity than $Pt_{37}Rh_{20}$-$(SnO_2)_{43}$ from 0.2 to 0.35 V, demonstrating 2.8 times higher CO_2 selectivity at 0.35 V. These results showed that CO_2 generation via C-C bond splitting of ethanol was enhanced on tri-phase $Pt_{37}Rh_{20}O_{21}$-$(SnO_2)_{43}$ with a partially oxidized Pt and Rh core. We note that though $Pt_{37}Rh_{20}O_{21}$-$(SnO_2)_{43}$ displayed a superior CO_2 generation rate,

commercial Pt has the highest CO_2 selectivity, largely due to the low overall current density (j_{Total}).

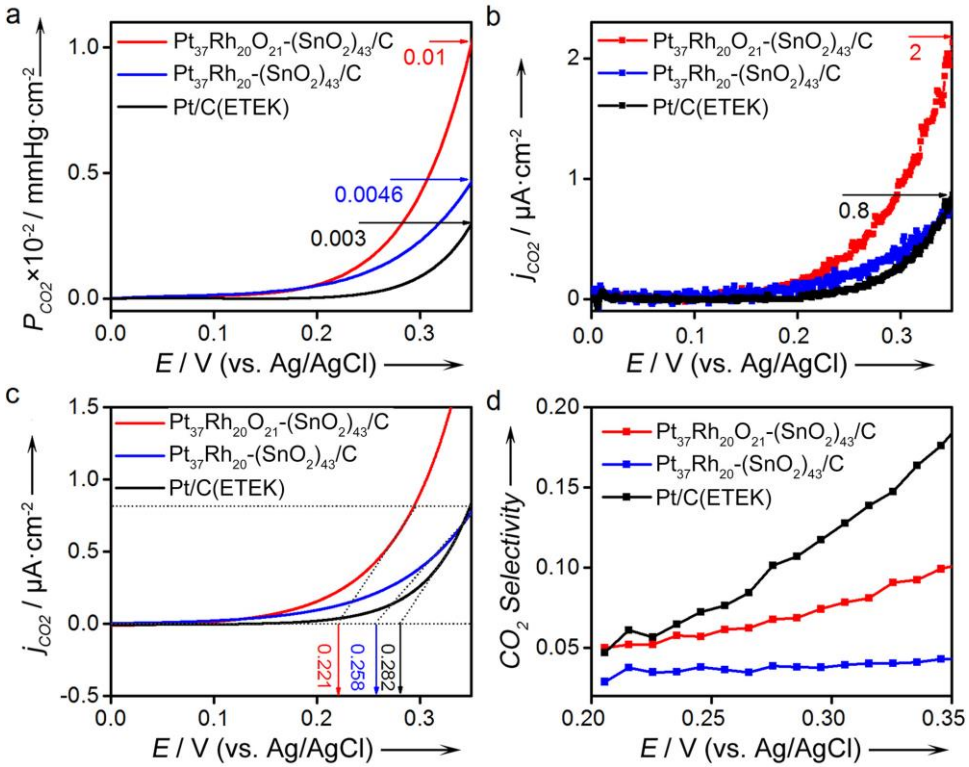

Figure 4.9 Electrokinetics analyses of carbon supported $Pt_{37}Rh_{20}O_{21}$-$(SnO_2)_{43}$, $Pt_{37}Rh_{20}$-$(SnO_2)_{43}$ and Pt (ETEK).

4.4 STABILITY TESTS OF $Pt_{37}Rh_{20}O_{21}$-$(SnO_2)_{43}$

To evaluate the stability of the core-shell structure during EOR. The catalyst was tested at 0.35 V for an hour in the three-electrode half cell. The TEM image showed that $Pt_{37}Rh_{20}O_{21}$-$(SnO_2)_{43}$ catalysts after one-hour CA measurement had very similar sizes and distribution compared with fresh catalysts without discernible particles dissolution or agglomeration, and the STEM-EELS line scan demonstrated a similar core-shell structure with a Pt-Rh-rich core and a SnO_2-rich shell in **Figure 4.10**. Moreover, $Pt_{37}Rh_{20}O_{21}$-$(SnO_2)_{43}$ only showed a 14% loss of ECASA after one-hour CA measurement, much lower

than that of commercial Pt/C (20% loss) as shown in **Figure 4.11**. All these results pointed to the fact that $Pt_{37}Rh_{20}O_{21}$-$(SnO_2)_{43}$ catalysts have a superior chemical stability even compared with commercial Pt catalysts.

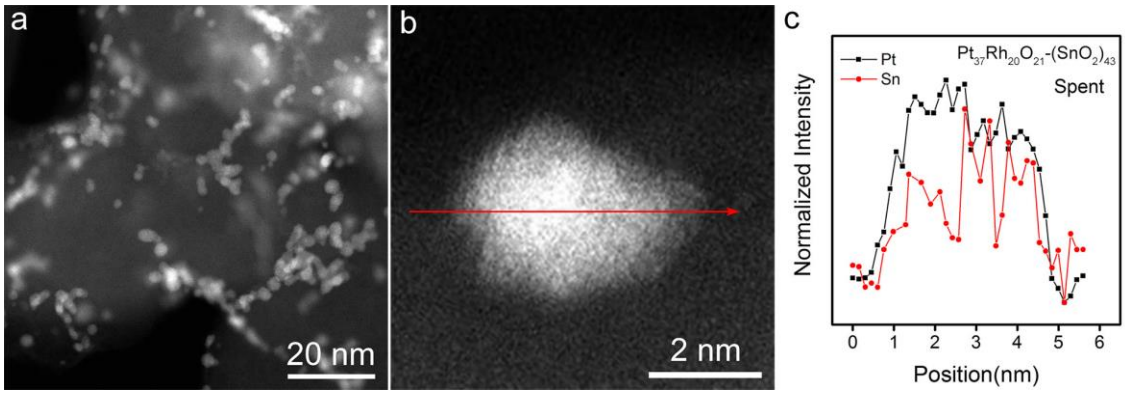

Figure 4.10 (a) TEM images of the spent-$Pt_{37}Rh_{20}O_{21}$-$(SnO_2)_{43}$/C after one hour CA measurement. (b, c) EELS line scan across the spent-$Pt_{37}Rh_{20}O_{21}$-$(SnO_2)_{43}$ particle as indicated by the arrow.

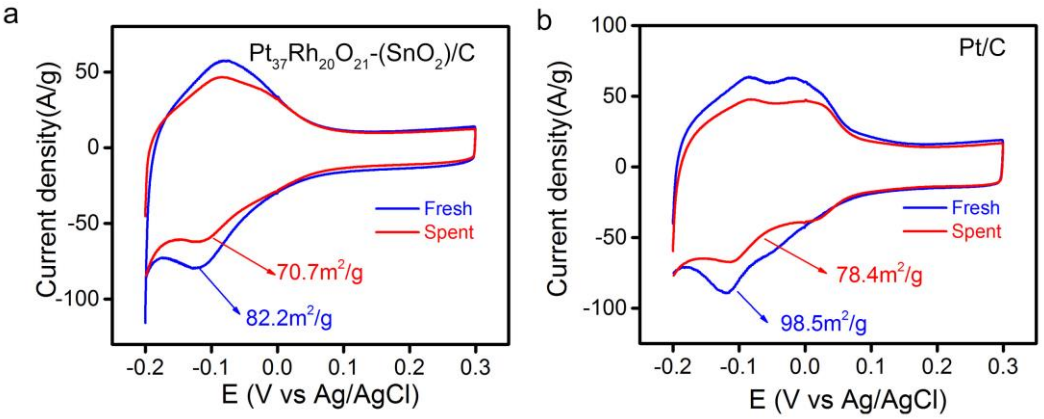

Figure 4.11 Comparison of ECASAs between the fresh and spent samples after one hour CA measurements. (a) $Pt_{37}Rh_{20}O_{21}$-$(SnO_2)_{43}$/C and (b) Pt(ETEK).

4.5 DISCUSSION AND CONCLUSION

In addition to the discovery of unexpected promotional effect of partially oxidized Pt and Rh core on the CO_2 generation, we also found that the chemical composition of Pt

and Rh also played a role in the electro-kinetics of CO_2 generation. Pt/Rh/Sn materials with different Pt and Rh composition were synthesized, indexed as $Pt_{39}/Rh_{12}/Sn_{49}$. Our electrochemical data showed the similar results: in term of CO_2 generation $Pt_{39}/Rh_{12}/Sn_{49}$ underperform $Pt_{37}/Rh_{20}/Sn_{43}$ summarized in **Table 4.3**, but tri-phase $Pt_{39}Rh_{12}O_{21}$-$(SnO_2)_{49}$ with a partially oxidized Pt and Rh core indeed outperform bi-phase $Pt_{39}Rh_{12}$-$(SnO_2)_{49}$ with a PtRh alloy core. The former suggests a Pt to Rh ratio of nearly 2:1 was the optimal composition for the CO_2 generation, and the latter confirms that a partially oxidized Pt and Rh core has a better CO_2 generation kinetics than Pt-Rh alloy core. Although our results demonstrated that oxidation states of Pt and Rh, and chemical compositions of Pt/Rh/Sn play important roles in the activity and selectivity of EOR, however, other factors which are not covered in this study may also be critical. For example, single crystal noble metal nanoparticles with high-index facets have demonstrated a high activity (charge-transfer rate) towards EOR.[41, 42] However, the role of high-index facets of noble metal catalysts on the C-C bond-breaking of ethanol has been rarely reported, and therefore deserves further studies in the future.

In this study, we synthesized two types of carbon supported Pt/Rh-SnO_2 core-shell nanoparticles: one was tri-phase $PtRhO_x$-SnO_2 with a partially oxidized Pt and Rh core (segregated Pt and Rh phases) and a SnO_2 shell, and the other was bi-phase PtRh-SnO_2 with a PtRh alloy core and a SnO_2 shell. Using our newly designed four-electrode electrochemical cell equipped with a CO_2 microelectrode, we comprehensively studied the electro-kinetics of the CO_2 generation, including CO_2 generation rate and CO_2 selectivity, on both types of catalysts. Our studies showed that, for the first time, while the

PtRh-SnO_2 with a PtRh alloy core was still active, the formation of a partially oxide Pt and Rh core coincides with a 2.5-fold increase in the CO_2 generation rate towards EOR.

The exact mechanism of the promotional effect of the partially oxidized Pt and Rh core found in $Pt_{37}Rh_{20}O_{21}$-$(SnO_2)_{43}$ on the CO_2 generation kinetics via C-C splitting is still under investigation. However, it is clear that the ensemble effect, associated with particular arrangements of the Pt, Rh and O constituents, have played an important role towards the C-C splitting of ethanol. In lieu of ethanol dissociation, co-existing metallic and oxidized Pt and Rh might show special advantage towards C-C splitting. According to DFT calculations conducted on the process of $CO+\frac{1}{2}O_2 \rightarrow CO_2$, the reaction barrier of CO_2 formation is significantly lower if O atoms from the edge of the surface oxide are involved in the CO oxidation, compared with the reaction only involved with chemisorbed O atoms.[209] Thus, co-existence of metallic and oxidized Pt and Rh on the surface is expected to facilitate the CO_2 formation, whereas metallic phase provides large and available site for dissociative adsorption of ethanol via C-C splitting and oxidized Pt and Rh phases provide mobile O atoms for the oxidation of reaction intermediates such as CO and CH_x. Our findings of the partially oxidized core-shell catalysts, $Pt_{37}Rh_{20}O_{21}$-$(SnO_2)_{43}$, are of major importance for understanding complete electro-oxidation of ethanol on a fundamental level, and will help the design of a new genre of electro-catalysts that have a partially oxidized noble metal core for various reactions.

CHAPTER 5

POTENTIODYNAMICS STUDY OF CO_2 GENERATION DURING EOR: *OH ADSORBATES EFFECT

5.1 INTRODUCTION

Carbon-supported Pt is one of the most studied catalysts for EOR but is limited by the slow kinetics for generating CO_2 via breaking the C-C bond of C_2 species, producing more acetic acid and acetaldehyde.[33, 44, 175, 176] Moreover, small amounts of CH_x and CO could poison Pt and impede the subsequent reactions.[177-179] The formation of binary or ternary Pt-based catalysts has been reported,[138, 180, 181] among which ternary Pt/Rh/Sn was the best for CO_2 generation.[78, 119, 120, 160, 182] In such a ternary system, Pt strongly dehydrogenates the ethanol molecules and the resulting reaction intermediates, Rh facilitates C-C bond splitting via promoting β-hydrogenation of ethanol, and oxophilic Sn promotes the dissociative adsorption of water to form adsorbed OH (*OH) on catalyst surfaces to assist the oxidization of the reaction intermediates.

Two steps of C-C bond splitting and *CO removal by *OH oxidant resulting from water dissociation are generally accepted as crucial steps for EOR. [134, 179, 182, 183] Clearly characterizing the atomic structure of the catalysts and accurately detecting CO_2 generation will be helpful to understand the contributions of the reaction steps mentioned above. Regardless of the many studies reported previously, the underlying reason behind the low CO_2 selectivity during the EOR is still missing.

Hence, in this chapter, we combine the uniquely advantageous motif of a CO_2 microelectrode with the well-characterized, electrocatalytic advantages of ultrafine Pt-SnO_2 and PtRh-SnO_2 core-shell nanoparticles with sizes ranging from 2 to 3 nm, in order to study the activity and selectivity of the EOR, and thus understand the underlying mechanism of CO_2 generation via C-C bond-breaking. Specifically, the use of ultrafine Pt-SnO_2 and PtRh-SnO_2 core-shell nanoparticles (2 to 3 nm) not only maximizes the surface-to-volume ratio of the catalyst, but also provides a rational comparison with commercial carbon supported Pt (ETEK) which has the same size range. Moreover, noble metals show a distinctive surface strain when their diameter is decreased below a critical value of a few nanometers, which often results in a shift of the electronic band structure of noble metals and changes the interaction between reaction intermediates, and therefore could augment the inherent catalytic activity.[213-215] In this study, we have reported the synthesis and the characterization of Pt/Rh/SnO_2 and Pt/SnO_2 core-shell nanoparticles with sizes of 2.1±0.5 nm and 2.5±0.6 nm, compared with commercial Pt (ETEK) of 2.7±0.6 nm, using transmission electron microscopy (TEM), scanning transmission electron microscope-electron energy loss spectroscopy (STEM-EELS), X-ray absorption near edge structure (XANES), energy dispersive spectroscopy (EDS) and X-ray diffraction (XRD). The electrochemical activity towards EOR, especially CO_2 generation, was tested on these catalysts, along with commercial Pt. A four-electrode half-cell is used to detect *in situ* CO_2 generation during the EOR using linear sweep voltammetry (LSV) measurements, through which the CO_2 partial pressure, CO_2 generation rate and selectivity have been obtained to reveal the potentio-kinetic behaviors of these catalysts. Therefore, insight into the influence of *OH adsorbates on the CO_2

generation rate and selectivity has been obtained. Density functional theory (DFT) was used to model surface reactions and species over relevant catalyst surfaces.

5.2 STRUCTURAL CHARACTERIZATIONS OF CORE-SHELL PARTICLES

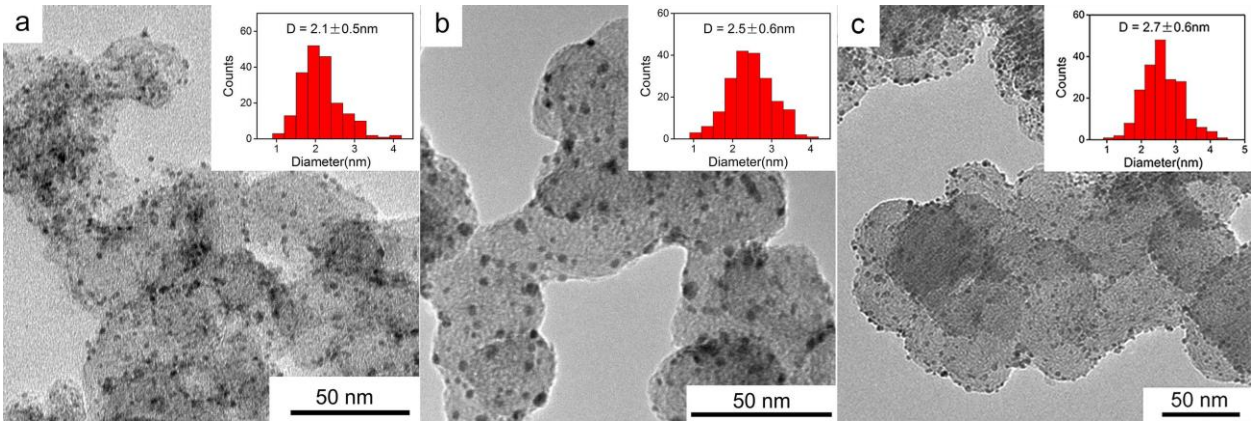

Figure 5.1 TEM images of (a) Pt/Rh/Sn, (b) Pt/Sn, (c) Pt/C(ETEK) nanoparticles.

Figure 5.1 shows TEM images of carbon-supported Pt/Rh/Sn, Pt/Sn, and commercial Pt (ETEK), showing evenly dispersed nanoparticles on active carbon. On the basis of 200 particles counted from TEM images, the average particle sizes of Pt/Rh/Sn, Pt/Sn and Pt (ETEK) are 2.1±0.5 nm, 2.5 ±0.6 nm, and 2.7±0.6 nm, respectively. **Figure 5.2** shows the EELS line scans of Pt and Sn from a typical Pt/Rh/Sn and Pt/Sn particle, acquired from an aberration-corrected STEM. In **Figure 5.2** b and d, the Sn element showed stronger signals at the particle edge than those at the center. In contrast, the Pt element showed a “volcano-like” distribution across the particle. These results indicate a core-shell structure with Pt-rich-core and Sn-rich-shell. Unfortunately, the ionization energy of the Rh $M_{4/5}$ edge is in the range of from 307 to 312 eV of energy loss, which overlaps with

the signal (from 280 to 340 eV) of the carbon K edge. Therefore, EELS could not detect the Rh distribution within the Pt/Rh/Sn nanoparticle.

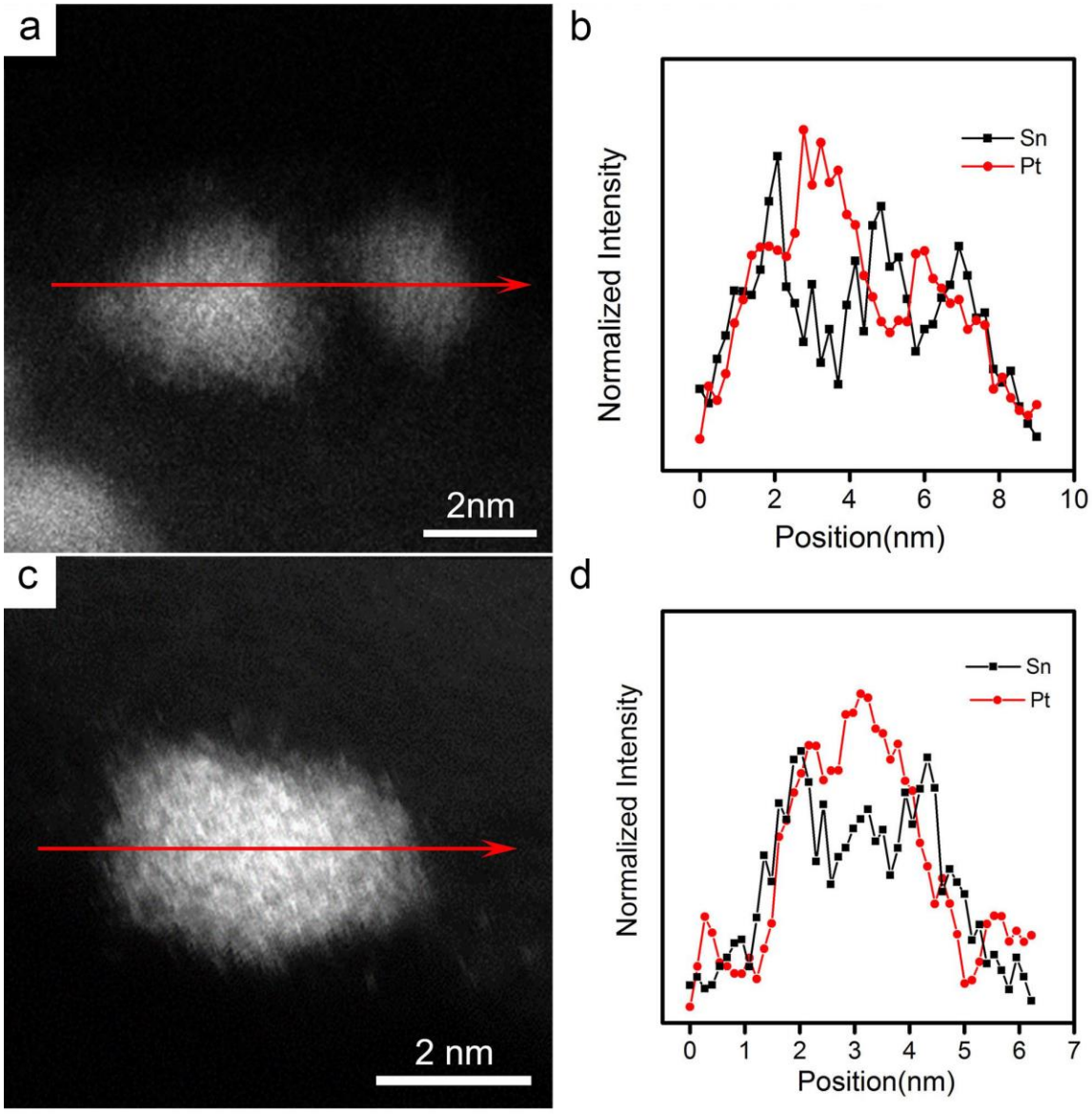

Figure 5.2 EELS line scan across (b) Pt/Rh/Sn and (d) Pt/Sn particles as indicated by the arrows in (a) and (c), respectively.

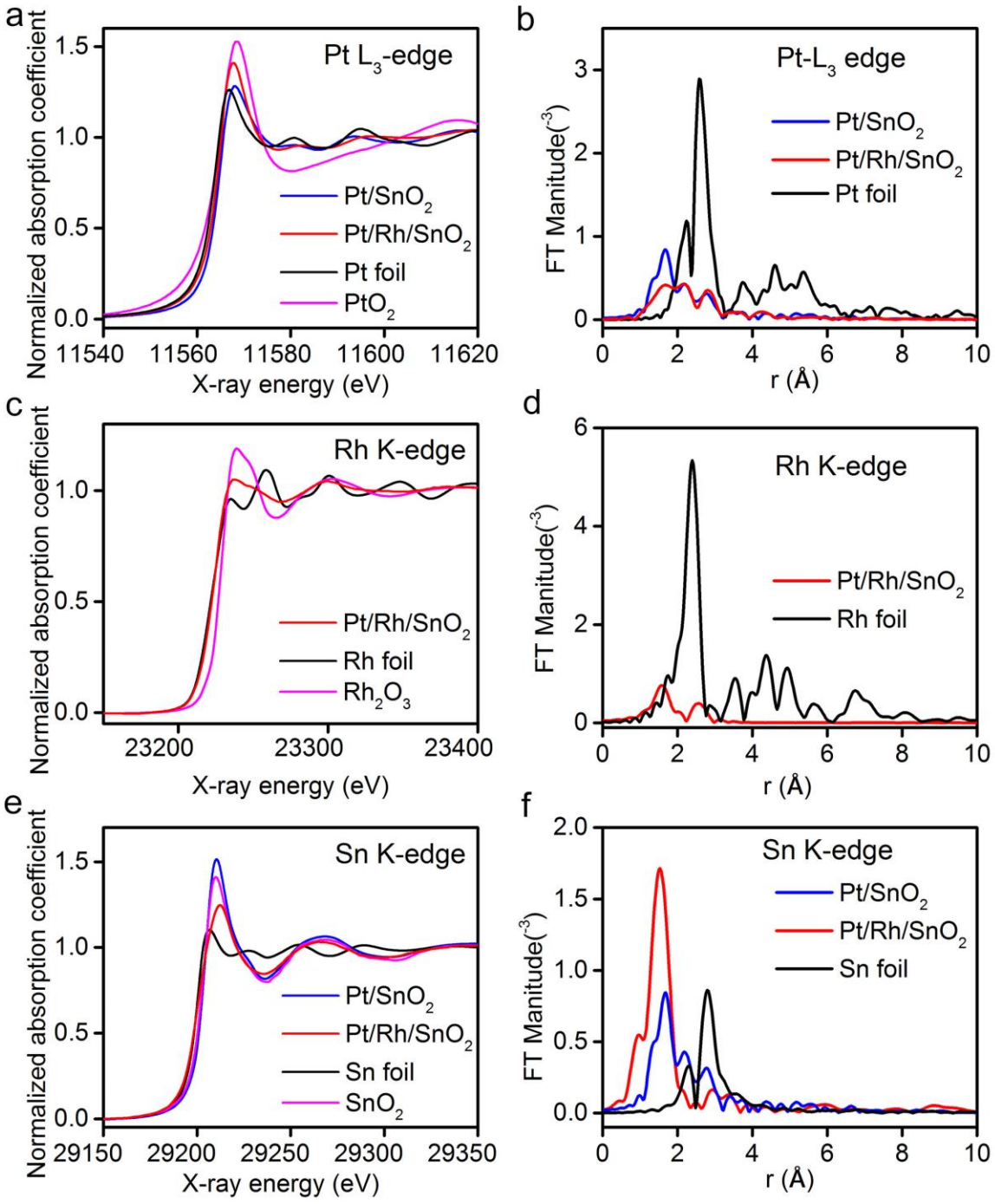

Figure 5.3 XANES data of (a) Pt L_3-edge (c) Rh K-edge. (e) Sn K-edge. R-space of (b) Pt L_3-edge (d) Rh K-edge. (f) Sn K-edge.

XANES measurements were used to investigate the electronic states of the Pt, Rh and Sn in catalysts. **Figure 5.3** shows the K-edges of Sn and Rh, and L_3-edge of Pt of

commercial Pt/C, and home-made Pt/Rh/Sn and Pt/Sn catalysts, together with the standard materials including Sn, Pt and Rh metal foils, and SnO_2, PtO_2 and Rh_2O_3 oxide powders. The Sn K-edge features of Pt/Rh/Sn and Pt/Sn as shown in **Figure 5.3** e was very different from those of metallic Sn foil, but similar to those of SnO_2 standard. It therefore strongly suggested that Sn was predominantly oxidized in Pt/Rh/Sn and Pt/Sn catalysts, denoted as Pt/SnO_2 and $Pt/Rh/SnO_2$, respectively. **Figure 5.3** a shows that Pt L_3-edge features (e.g. white line and oscillation of absorption features at higher energy) of Pt, Pt/Rh/Sn and Pt/Sn were very different from, PtO_2, the oxide standard, but similar to Pt foil, suggesting that Pt was predominantly metallic in Pt, Pt/Rh/Sn and Pt/Sn catalysts. Moreover, Pt/Rh/Sn and Pt/Sn showed slightly shifted white lines toward higher energy positions, mainly attributed to the interaction between the Pt and O atoms of adjacent SnO_2 clusters on the shell. On the other hand, in **Figure 5.3** c the Rh K-edge of Pt/Rh/Sn showed mixed features resembling the Rh foil and Rh_2O_3, indicating that a mixture of metallic and oxidized Rh existed.

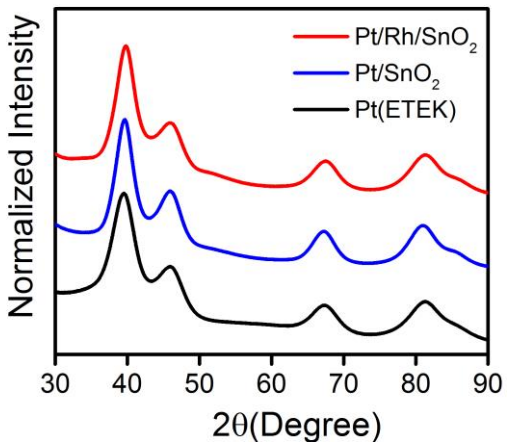

Figure 5.4 XRD patterns of carbon supported $Pt/Rh/SnO_2$, Pt/SnO_2, and Pt (ETEK).

Figure 5.4 shows the XRD patterns of Pt/Rh/SnO_2, Pt/SnO_2, and commercial Pt (ETEK). The diffraction peaks of Pt/C at 39.5º, 45.9º, 67.2º, 81.8º and 86.0º were assigned to the (111), (200), (220), (311) and (222) planes, respectively, corresponding to a face centered cubic (FCC) structure. Pt/Rh/SnO_2 and Pt/SnO_2 had nearly identical diffraction peaks compared with commercial Pt, suggesting that they kept a cubic structure. The averages sizes were calculated to be 2.6, 2.7 and 2.2 nm for Pt/Rh/SnO_2, Pt/SnO_2, and Pt by the Scherrer equation, agreeing well with the values obtained from TEM images. No discernable peak shift between Pt/Rh/SnO_2, Pt/SnO_2 and Pt were observed. It is possible that the Pt alloyed with the Rh in the Pt/Rh/SnO_2 catalyst. However, due to the similar lattice constants of the Pt (0.392 nm) and the Rh (0.380 nm) and the peak broadening from the finite size effect, the peaks shift in the diffractograms may not be observed even if there was a formation of a PtRh alloy in the Pt/Rh/SnO_2 catalyst. On the other hand, it is also possible that the Pt and Rh were in separated phases (segregated Pt metal and Rh metal within 2.1 nm for the Pt/Rh/SnO_2 catalyst). Due to the similar reasons (similar lattice constants and finite size effect), the diffraction peaks from the Pt and the Rh components were overlapped and indiscernible. Diffraction peaks from SnO_2, PtO_2 or Rh_2O_3 were not observed in either Pt/Rh/SnO_2 or Pt/SnO_2 catalysts, though XANES and STEM-EELS strongly suggested that Sn existed primarily as a SnO_2 phase on the shell region, as well as the coexistence of metallic and oxidized Pt and Rh components. It is possible that SnO_2, PtO_2 or Rh_2O_3 components were very small crystalline clusters or highly disordered materials, so that they couldn't be detected by XRD due to the lack of long-range order.

5.3 ELECTROKINECTICS ANALYSES

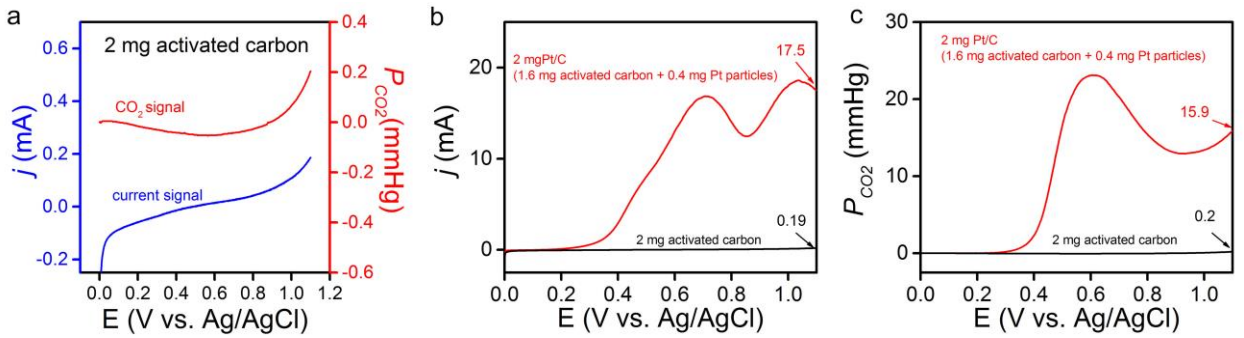

Figure 5.5 (a) LSV and CO_2 generation curves of 2 mg activated carbon with respect to potential at the scan rate of 0.5 mV/s in 0.5 M H_2SO_4 electrolyte. (b) LSV curves on 2 mg carbon supported Pt in 0.5 M ethanol/ 0.5 M H_2SO_4 electrolyte and 2 mg activated carbon in 0.5 M H_2SO_4 electrolyte.

Electrochemical activities of Pt/Rh/SnO_2, Pt/SnO_2 and Pt(ETEK) toward EOR were evaluated in an electrochemical cell equipped with a CO_2 microelectrode for *in situ* CO_2 detection. To confirm that the electrical current and CO_2 signal obtained during the electrochemical oxidation of ethanol were primarily from the catalyst materials instead of the platinum foil substrate, the blank experiment was conducted using platinum foil without active material as shown in **Figure 5.5**. The comparison between blank platinum foil and platinum foil fully covered with Pt/C catalyst shows that the former only contributed ~3% to surface area, ~1.5% to overall current and ~2% to CO_2 signal when the Pt foil was completely exposed to the electrolyte. Considering the complete surface of the Pt foil was nearly covered by the carbon supported catalysts, the contribution of Pt foils toward the current and CO_2 signal is expected to be far below 1.5 %.

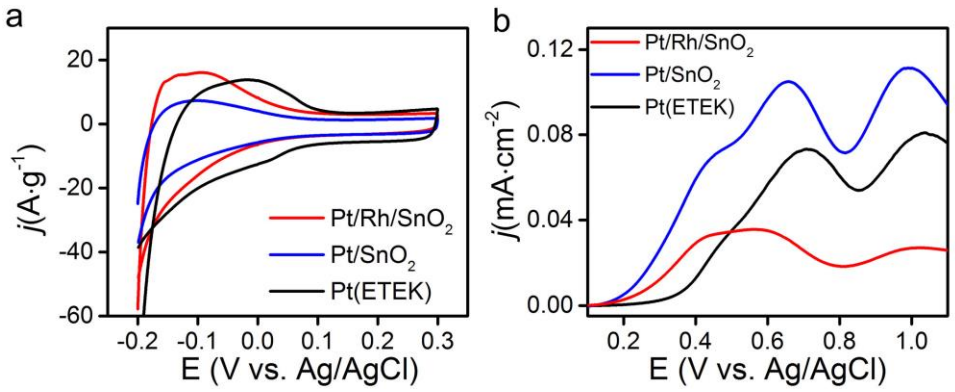

Figure 5.6 (a) CV scans in the 0.5 M of H_2SO_4 electrolyte at the potential scan rate of 20 mV/s and (b) CV forward scans in the 0.5 M H_2SO_4/ 0.5 M ethanol solution at the potential scan rate of 0.5 mV/s over carbon supported Pt/Rh/SnO_2, Pt/SnO_2 and Pt (ETEK).

The CVs were first conducted in 0.5 M H_2SO_4 electrolyte (**Figure 5.6**), from which the electrochemically active surface area (ECASAs) of the Pt/Rh/SnO_2, Pt/SnO_2 and Pt(ETEK) catalysts were calculated to be 56, 39 and 61 m^2/g, respectively. **Figure 5.6** b shows the current densities of the EOR, averaged by ECASAs, as a function of external potential obtained from the LSV measurements at a scan rate of 0.5 mV/s in 0.5 M H_2SO_4 and 0.5 M ethanol. Pt/SnO_2 exhibited the highest current density throughout a potential window from 0.1 to 1.1 V (vs. Ag/AgCl). At 0.65 V, Pt/SnO_2 showed a current density around 3.4 and 1.6 times higher than those of Pt/Rh/SnO_2 and Pt. The results showed that the addition of SnO_2 to Pt increased the overall charge transfer rate of EOR, mainly due to the bifunctional effect in which the *OH was formed from water dissociation on SnO_2 and further reacted with the intermediates resulting from the α-dehydrogenation of ethanol. On the other hand, addition of Rh to Pt/SnO_2 resulted in a decreased charge transfer rate of the EOR. It has been generally accepted that the main products of the EOR are acetaldehyde and acetic acid, resulting from the α-dehydrogenation of ethanol.[176] Therefore, the α-dehydrogenation process, through the incomplete oxidation

of ethanol, in fact mainly contributed to the overall current density (charge transfer rate) of EOR. However, α-dehydrogenation was less favored on Rh sites, demonstrating that lower current density was observed on the Rh-containing catalyst of $Pt/Rh/SnO_2$ compared with Pt/SnO_2. It is also possible that in $Pt/Rh/SnO_2$ catalysts, the Rh component facilitates the C-C bond splitting favoring the formation C_1 fragments such as CO and CH_x, which poison the active Pt sites and account for the low current density observed.

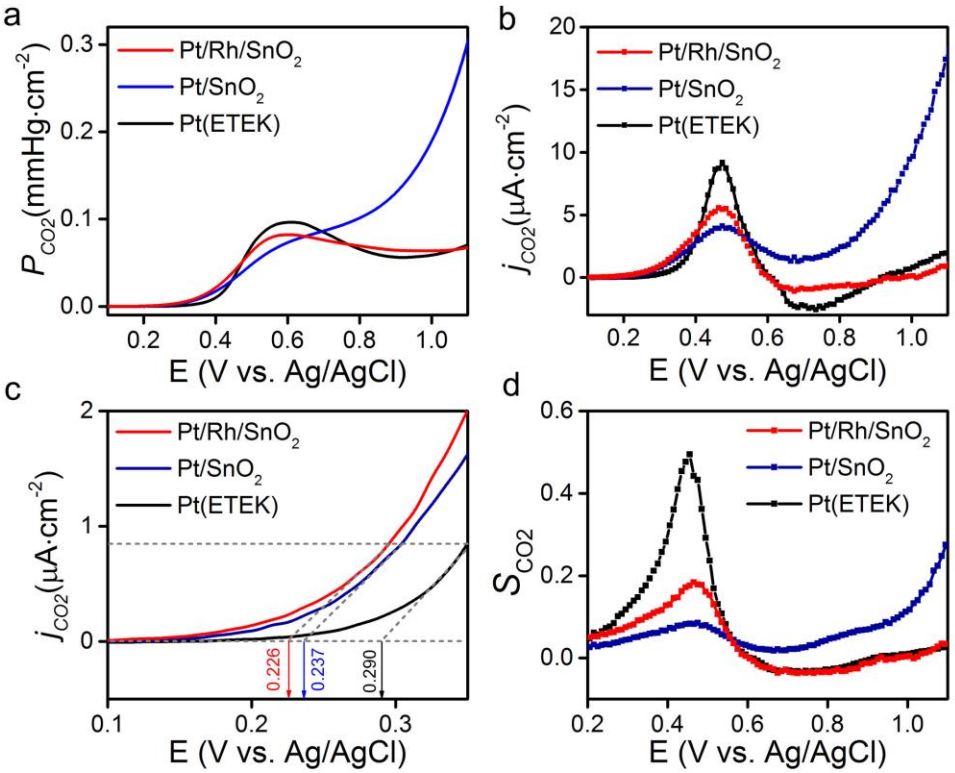

Figure 5.7 (a) Partial pressure of CO_2 (P_{CO2}), (b) current density from CO_2 generation (j_{CO2}), and (c) onset potential of CO_2 generation (enlarged from b) and (d) selectivity of CO_2 (S_{CO2}) with respect to potential at potential scan rate of 0.5 mV/s.

Figure 5.7 a shows the partial pressure of CO_2 (P_{CO2}) resulting from the generation of CO_2 during the EOR over Pt/SnO_2, $Pt/Rh/SnO_2$ and Pt using our four-electrode electrochemical cell. In previous EOR studies, *in situ* CO_2 measurements conducted

using FTIR and DEMS,[77, 86, 177, 178, 198] the CO_2 partial pressure (and/or concentration) was usually plotted as a function of reaction time or external potential. However, to better describe the electro-kinetics of EOR (e.g, CO_2 generation rate and selectivity), the time-resolved CO_2 production, namely accumulation rate, as a function of external potential is needed. In this study, the P_{CO2} measured *in situ* was used to calculate the total molar amount of generated CO_2 (N_{CO2}), and the CO_2 generation rate could be obtained by taking a derivative of CO_2 generation with respect to time.

Our results show that both P_{CO2} and j_{CO2} were strongly dependent on the external potential. At potentials ranging from 0.2 to 0.46 V, the P_{CO2} and j_{CO2} followed the order: Pt/Rh/SnO_2 > Pt/SnO_2 > Pt, indicating promotional effects of Rh and SnO_2 on CO_2 generation at low potentials. **Figure 5.7** c shows the onset potential of CO_2 generation follows the order of Pt/Rh/SnO_2 (0.226 V) < Pt/SnO_2 (0.237 V) < Pt (0.290 V). However, when the potential increased to the range from 0.46 to 0.56 V, P_{CO2} and j_{CO2} of Pt increased more considerably than Pt/SnO_2 and Pt/Rh/SnO_2, showing an order of Pt > Pt/Rh/SnO_2 > Pt/SnO_2; when the potential continued to increase beyond 0.56 V, P_{CO2} and j_{CO2} of Pt and Pt/Rh/SnO_2 decreased sharply, while Pt/SnO_2 showed continuously increasing P_{CO2} and j_{CO2}. At 1.1 V, the P_{CO2} of Pt/SnO_2 was about 4.3 and 4.5 times higher than those of Pt and Pt/Rh/SnO_2, and the j_{CO2} of Pt/SnO_2 was about 9.0 and 19.7 times higher than those of Pt and Pt/Rh/SnO_2. The distinct potential dependent P_{CO2} and j_{CO2} strongly indicated that the C-C bond splitting mechanism depends on potential range and chemical compositions. Our CO_2 generation results obtained from the CO_2 microelectrode are consistent with the reported results using *in situ* DEMS. For example, Behm's group observed discernable CO_2 generation over Pt_3Sn/C up to 0.64 V(vs.

Ag/AgCl) [178]. Delpeuch et al reported that Pt-SnO_2/C showed a decreased CO_2 signal when potential increased from 0.55 to 0.75 V, followed by an increase of CO_2 as potential further increased from 0.75 to 1.0 V(vs. Ag/AgCl), which is consistent with what we observed in the current study on Pt/SnO_2 [78]. It is also worth mentioning that although the amount of CO_2 generation at the low potential range (0.1 - 0.7 V) is strongly depended on the chemical compositions, following the trend as Pt > Pt/Rh/SnO_2 > Pt/SnO_2 (**Figure 5.7** b), all three catalysts showed the first peaks of C-C scission at similar potential values (~ 0.5 V), independent on the chemical compositions. Similar results have been reported recently by Pastor and Garcia et al in Pt/Sn systems, where FTIR and DEMS analyses showed C-C scission all happened at similar potential values independent of Sn loading [216].

Figure 5.7 d shows CO_2 selectivity (S_{CO2}). A similar potential-dependent CO_2 selectivity was observed. From 0.2 to 0.56 V, S_{CO2} followed the order Pt > Pt/Rh/SnO_2 > Pt/SnO_2, while in the potential window from 0.56 to 1.1 V, S_{CO2} followed the order Pt/SnO_2 > Pt/Rh/SnO_2 ≈ Pt. Commercial Pt showed the highest S_{CO2} value of 51% at 0.47 V, corresponding to a CCE value of 34% based on the formula:

$$CCE = \frac{S_{CO_2}}{1 + S_{CO_2}} \qquad 5.1$$

It should be noted that a CCE value of 34% observed from commercial Pt in this study is slightly higher than those reported from DEMS measurements from which CCE values ranged from 12% to 26% [133, 217]. The difference between the DEMS results reported elsewhere and our own results is not just attributed to the experimental conditions such as ethanol concentration and catalysts loading [184, 218].

5.4 DFT CALCULATIONS

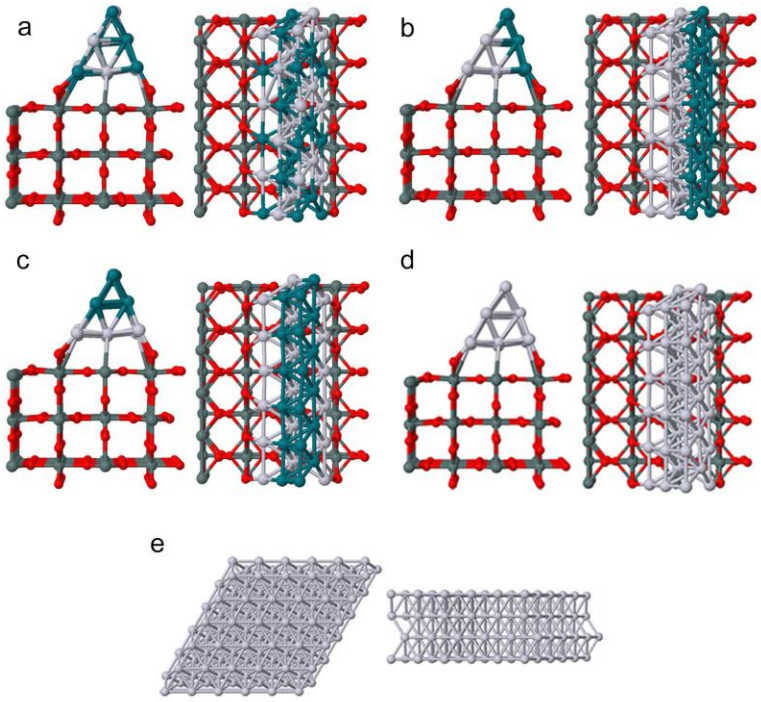

Figure 5.8 Configuration of each model for the DFT calculations: (a) 1st PtRh-SnO_2 model, (b) 2nd PtRh-SnO_2 model, (c) 3rd PtRh-SnO_2 model, (d) Pt-SnO_2 model, and (e) Pt(111).

DFT calculations were conducted on the surfaces of Pt, Pt-SnO_2 and PtRh-SnO_2 to understand how the Rh and SnO_2 affected the C-C bond splitting of ethanol. We modeled the step of C-C bond splitting from three possible C_2 intermediates (*CH_3CO, *CH_2CO, and *CHCO) as shown in the following pathways:

$$*CH_3CO \rightarrow *CH_3 + *CO \quad (5.2)$$

$$*CH_2CO \rightarrow *CH_2 + *CO \quad (5.3)$$

$$*CHCO \rightarrow *CH + *CO \quad (5.4)$$

In this study, three different PtRh-SnO_2 models were considered, in comparison to a Pt-SnO_2 model. The top and side views of each model are shown in **Figure 5.8**. The Pt atoms are light grey, oxygen atoms are red, Sn atoms are dark grey, and Rh atoms are blue-green. In the 1st PtRh-SnO_2 model, the Rh atoms are distributed through the PtRh alloy; in the 2nd model, the Rh atoms are located on a (111) facet of Pt; in the 3rd model, the Rh atoms are concentrated away from the SnO_2 surface. **Table 5.1** shows the calculated reaction energies for C-C bond splitting, from which activation energies were estimated in accordance with the Brønsted-Evans-Polanyi relation. More details of the calculations over each surface are shown in **Appendix**. Taking the precursor *CHCO as an example, we calculated the reaction energies over Pt-SnO_2, PtRh-SnO_2 (1st model), PtRh-SnO_2 (2nd model), and PtRh-SnO_2 (3rd model) surfaces to be -1.07, -1.36, -1.62 and -1.34 eV, respectively. All of the Rh-containing models had lower reaction energies than Pt-SnO_2, demonstrating that Rh facilitates C-C bond splitting as shown in **Figure 5.9** and **Table 5.1**. These calculations agreed well with our experimental data especially obtained at lower potentials.

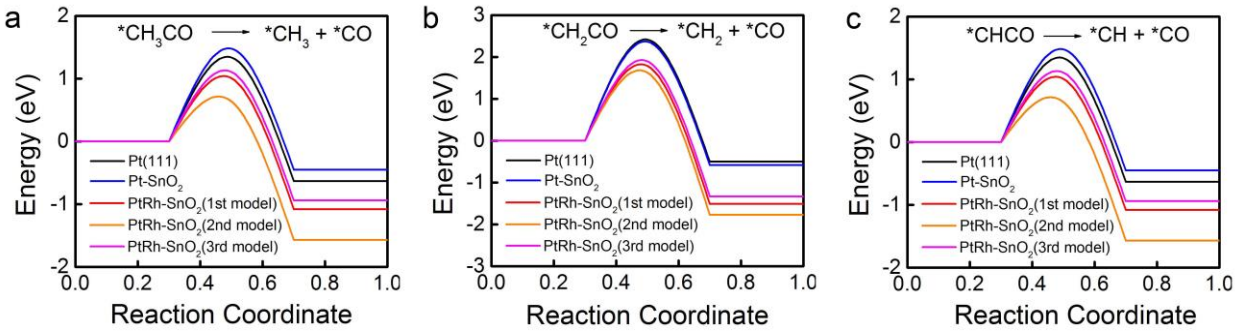

Figure 5.9 Structures of three different PtRh-SnO_2 models ((a) 1st model, (b) 2nd model, and (c) 3rd model), (d) Pt-SnO_2 model and (e) Pt(111)model. Reaction energies for C-C bond splitting of (f) *CH_3CO, (g) *CH_2CO, and (h) *CHCO over the Pt(111), Pt-SnO_2, and PtRh-SnO_2 surfaces.

Table 5.1 Calculated reaction energies (eV) for C-C bond splitting over various catalyst surfaces ($*CH_xCO \rightarrow *CH_x + *CO$).

Catalyst	Reaction Energy (eV)[a]		
	*CHCO	*CH_2CO	*CH_3CO
Pt(111)	-1.08	-0.5	-0.63
Pt-SnO_2	-1.07	-0.58	-0.45
PtRh-SnO_2(1st model)	-1.36	-1.51	-1.08
PtRh-SnO_2(2nd model)	-1.62	-1.77	-1.57
PtRh-SnO_2(3rd model)	-1.34	-1.33	-0.94

a Reaction energy=the adsorption energy of CO on a catalyst + the adsorption energy of CH_x on a catalyst – the adsorption energy of CH_xCO on a catalyst. It can reflect the activation energy of C-C bond splitting.

Other promotional effects of Rh on C-C bond splitting could be due to the fact that Rh had strong ability to promote β-dehydrogenation of *CH_3CHO, a reaction intermediate after dehydrogenation of the α-carbon and hydroxyl group of an ethanol molecule, to form *CH_2CHO that was the preferable precursor of C-C bond splitting.[20, 86, 134] On the other hand, SnO_2 had a strong interaction with water and formed *OH via dissociative adsorption of water at a lower potential. The resulting *OH species would oxidize adjacent *CO or *CH_x occupied on Pt and/or Rh sites to CO_2 as reactions $*CH_x + *OH \rightarrow CO_2$ and $*CO + *OH \rightarrow CO_2$, evidenced by the fact that CO_2 was detected at lower potentials on Pt/Rh/SnO_2 and Pt/SnO_2 instead of Pt.

A comparative set of DFT calculations for H_2O and *OH adsorbates formation on the surfaces of Pt, SnO_2, Pt-SnO_2 and PtRh-SnO_2 were conducted. The adsorption energies of H_2O and *OH adsorbates on various surfaces are summarized in **Table 5.2**. The results

show that, firstly, the formation of *OH adsorbates is considerably more exothermic than that of H_2O on all the studied surfaces, indicating *OH more stable than H_2O on the catalysts. The *OH adsorption energies follow the order: Pt (-2.2 eV) > PtRh-SnO_2(1st model: -2.81 eV, 2nd model: -2.64 eV, and 3rd model: -2.95 eV) > Pt-SnO_2(-3.23 eV). It is important to point out that the DFT calculations describe the reaction mechanism under equilibrium state, corresponding more closely to the catalyst-OH interaction at low potentials.

Table 5.2 Calculated adsorption energies (eV) for water and *OH adsorption over various catalyst surfaces

Catalyst	Adsorbate	Adsorption energy (eV)[a]
Pt(111)	*H_2O	-0.34
	*OH	-2.2
SnO_2	*H_2O	-1.26
	*OH	-1.53
Pt-SnO_2	*H_2O	-0.94
	*OH	-3.23
PtRh-SnO_2(1st model)	*H_2O	-0.92
	*OH	-2.81
PtRh-SnO_2(2nd model)	*H_2O	-0.83
	*OH	-2.64
PtRh-SnO_2(3rd model)	*H_2O	-1.06
	*OH	-2.95

a.Adsorption energy= the energy for the free species (H_2O or OH) + the energy for the surface of the catalyst – the total energy of the adsorption system (H_2O-catalyst or OH-catalyst)

5.5 THE INFLUENCE OF *OH ADSORBATES

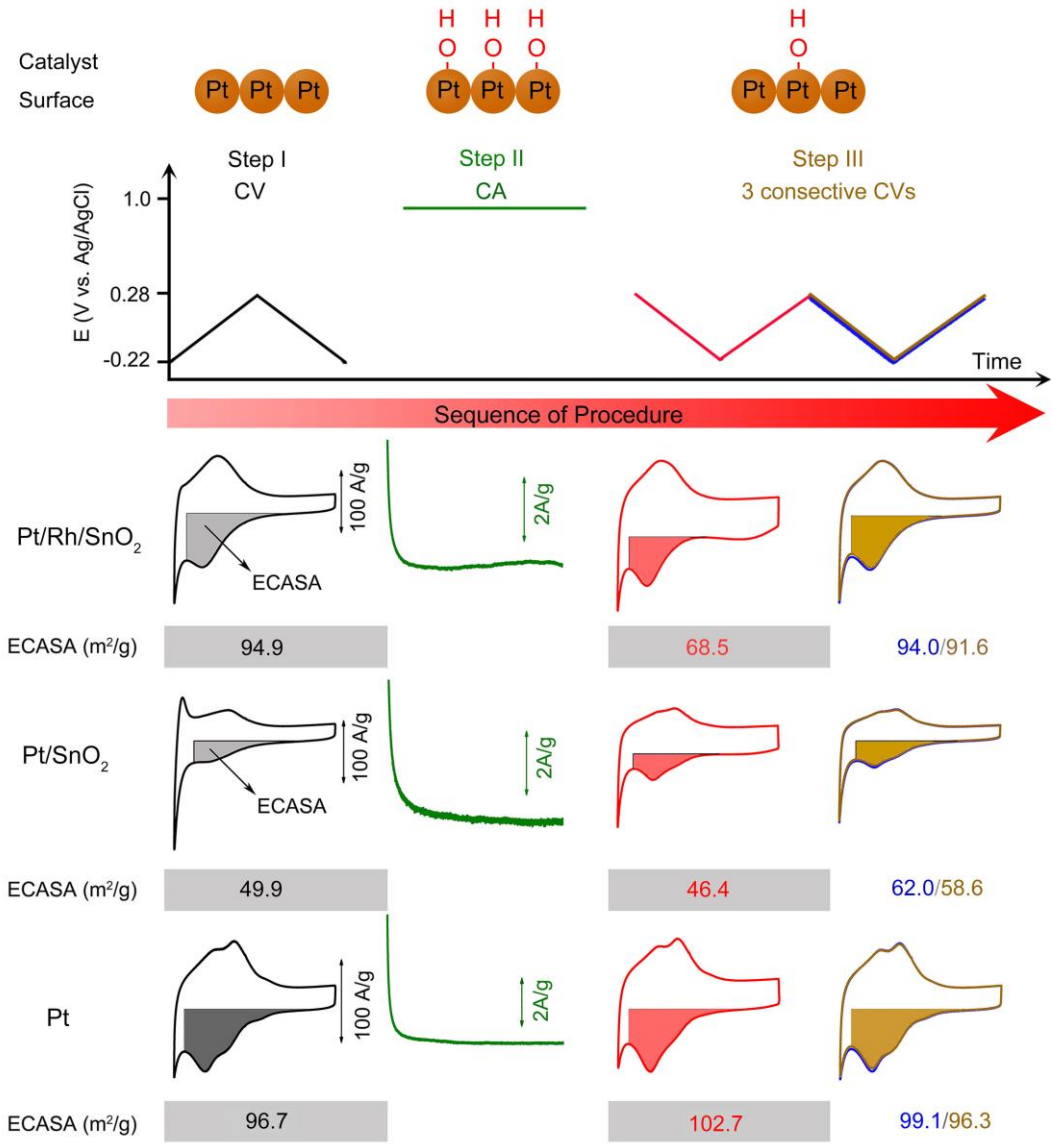

Figure 5.10 *OH formation and effect on the ECASA over $Pt/Rh/SnO_2$, Pt/SnO_2, and Pt/C.

The promotional effect of Rh and SnO_2 on the generation of CO_2 at lower potentials was observed experimentally and was confirmed by DFT calculations. However, the superior electro-kinetics of Pt/SnO_2 at higher potentials ranging from 0.46 to 1.1 V, such as CO_2 partial pressure (P_{CO2}), generation rate (j_{CO2}) and selectivity (S_{CO2}) compared with

Pt and Pt/Rh/SnO_2, has not been reported before. To understand this unexpectedly high electro-kinetics of Pt/SnO_2 at higher potentials (0.46 to 1.1 V), we conducted a well-designed series of experiments to show that the *OH adsorbates played an important role in determining the CO_2 generation as shown in **Figure 5.10**. The first row describes the sequence of the experimental procedure. Only one cycle of CV was conducted from -0.22 to 0.28 V in 0.5 M H_2SO_4 electrolyte at potential scan rate of 50 mV/s, and then CA at 1 V was conducted for 0.5 hour. After that, 3 cycles of CV were conducted; CVs, CA and ECASAs over (2nd row) Pt/Rh/SnO_2 and (3rd row) Pt/SnO_2 are shown by the sequence of the procedure. The shadowed area was used to calculate the ECASA.

Our data showed that Pt/Rh/SnO_2 had an initial ECASA of 94.9 m^2/g after the 1st CV (black). After formation of *OH adsorbates at 1.0 V, the ECASA calculated from the 2nd CV (red curve) was 68.5 m^2/g, corresponding to a 27.8% loss of ECASA compared with the value calculated from the first cycle of CV, indicating that the *OH coverage on the surface blocked considerable number of active sites. The values of ECASA from consecutive 3rd and 4th CVs increased to 94.0/91.6 m^2/g, very close to the initial ECASA value obtained from the first cycle of CV experiment (94.9 m^2/g). The recovered ECASA strongly suggested that the observed 27.8% loss of ECASA after CA measurements was indeed due to the coverage of *OH adsorbates instead of irreversible reconstruction of the surface. On the other hand, Pt/SnO_2 showed only a 7.0 % (from 49.9 to 46.4 m^2/g) loss of its initial ECASAs and Pt did not show any loss of ECASAs, after formation of *OH adsorbates from CA measurements. The results suggested that the Rh component had a much stronger susceptibility toward *OH coverage or poisoning compared to Pt or SnO_2, evident by the weak *OH tolerance found in Pt/Rh/SnO_2. To further confirm our results,

we also studied *OH coverage on commercial Rh/C using the same procedure as shown in **Figure 2.5**. The data showed that Rh had an almost 63.3% loss of initial ECASA after CA measurement at 1.0 V. It is worth mentioning that the values of ECASA of all three catalysts obtained from the three-electrode half-cell measurements are higher than the ones obtained from the four-electrode electrochemical cell reported previously.

5.6 DURABILITY TESTS OF Pt, Pt/SnO_2 AND $Pt/Rh/SnO_2$

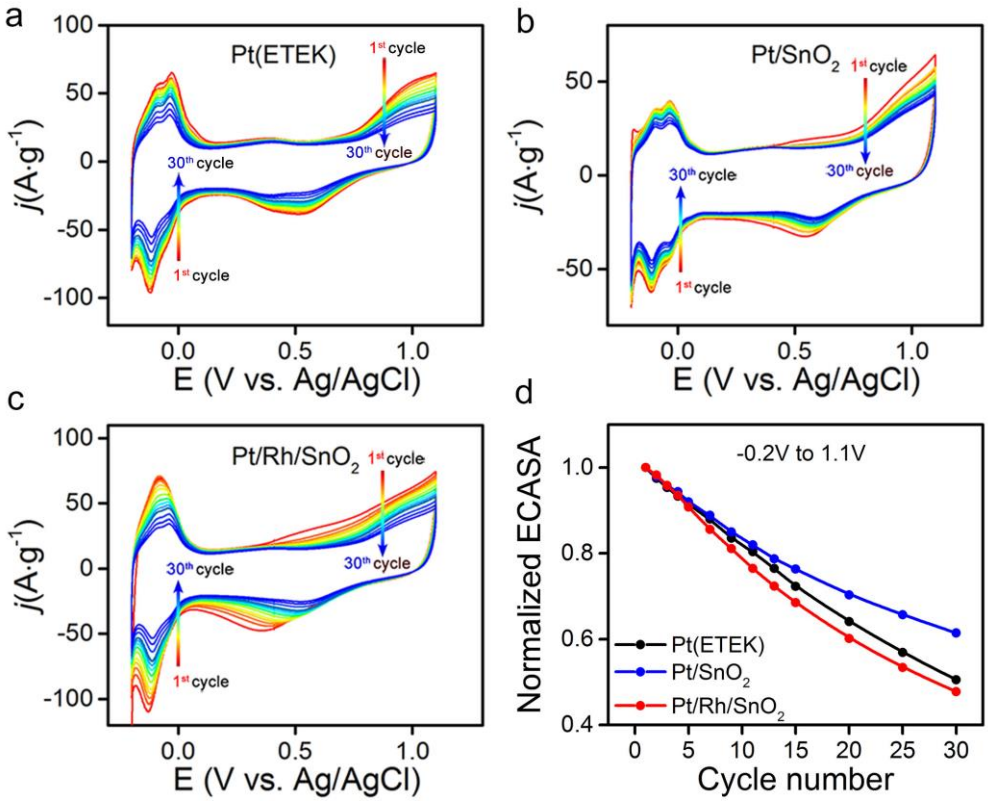

Figure 5.11 CVs of carbon supported (a) Pt(ETEK), (b) Pt/SnO_2 and (c) $Pt/Rh/SnO_2$ catalysts in 0.5 M H_2SO_4 solution at the scan rate of 50 mV/s from -0.2 to 1.1 V for 30 cycles. (d) Relative ECASAs at different cycles of each catalyst during cycling.

The durability of Pt-based catalysts is one of the main challenges to be overcome for the large-scale deployment of proton exchange membrane fuel cell technologies.

Particularly, recent work using inductively coupled plasma mass spectrometry (ICP–MS) and *in situ* Raman studies have unambiguously showed that Pt dissolution in an acidic environment happens either upon the formation of a transient oxide in an anodic process or via the reduction of the Pt oxide during a cathodic process [219, 220]. Here we have studied the durability of the Pt, Pt/SnO_2 and Pt/Rh/SnO_2 catalysts in an acidic environment during the high potential CV cycling and during the EOR processes.

Figure 5.11 shows the CVs of carbon supported Pt, Pt/SnO_2 and Pt/Rh/SnO_2 catalysts in a 0.5 M H_2SO_4 solution, cycling between -0.2 and 1.1 V for 30 cycles. It is clearly seen that all the catalysts show continuously decreasing peak intensities, including the hydrogen oxidation peak (from -0.2 to 0.1 V) and Pt oxidation peak (from 0.7 to 1.1 V) in the anodic scans as well as Pt reduction peaks (from 0.7 to 0.2 V) and a hydrogen absorption peak (from 0.3 to -0.2 V) in the cathodic scans. Intensity loss indicates that during the cycling in the acid electrolyte Pt and/or Rh dissolution and surface reconstruction happened for all three catalysts. Particularly, Pt/Rh/SnO_2 catalysts showed not only the biggest loss in current density, but also the most distinct changes of CV features in the Pt region (from 0.7 to 0.2 V) in the cathodic scans. As shown in **Figure 5.11** c, during the cathodic sweeps the peaks of the Pt reduction shifted from 0.36 to 0.54 V and finally reached a steady–state Pt–like CVs, indicating significant dissolution and/or poisoning of Rh via its strong interaction with *OH. On the other hand, Pt/SnO_2 showed the least changes of CV features during the cycling. **Figure 5.11** d summarizes the ECASAs of all three catalysts calculated from the hydrogen absorption range from -0.2 to 0.3 V during 30 cycles of sweeps between -0.2 and 1.1 V. All three catalysts showed very similar losses in ECASA within 5 cycles. Upon more cycling, Pt/SnO_2 showed the smallest

ECASA loss and retained 61.4% of with its original value after 30 cycles of CVs, while Pt/Rh/SnO_2 showed the largest ECASA loss and retained only 47.7% of its original value after cycling. This indicates (i) SnO_2 shell can prevent Pt from dissolution during the high potential cycling, and (ii) compared with Pt, the Rh components is more vulnerable to be poisoned and/or leached through interacting with the *OH species during the high potential sweeping. These results are congruent with the conclusion on influence of *OH adsorbates on the CO_2 generation shown in **Figure 5.7**, that the SnO_2 component protected the Pt from interacting with the *OH species and the Rh component was more easily dissolved during the high potential sweeping than Pt.

Figure 5.12 shows the durabilities of Pt, Pt/SnO_2 and Pt/Rh/SnO_2 catalysts during the EOR in a 0.5 M ethanol and 0.5 M H_2SO_4 solution via one-hour CA measurements at constant potentials of 0.5 and 1.0 V, respectively. **Figure 5.12** a and b show that current densities of the EOR drop continuously with time, which could be due to the poisoning of surface active sites. At a potential of 0.5 V, EOR current densities followed the order of Pt/SnO_2 > Pt ≈ Pt/Rh/SnO_2 after one-hour CA, while at 1.0 V the current densities followed the order of Pt/SnO_2 ≈ Pt > Pt/Rh/SnO_2. The long-term durabilities of all three catalysts from CA measurements largely followed similar trends as the CV results demonstrated in **Figure 5.6** b, where Pt/SnO_2 showed the highest EOR activities at various potentials and the Pt/Rh/SnO_2 showed the lowest activities. **Figure 5.12** c and d show the values of P_{CO2} during one-hour CA measurements of Pt, Pt/SnO_2 and Pt/Rh/SnO_2 catalysts at 0.5 V and 1.0 V, respectively. Slightly different from current density profiles shown in **Figure 5.12** a and b, the values of P_{CO2} increased rapidly within the first 5 minutes of the reaction and then decreased rather slowly till reaching quasi-steady states after 30 minutes of reaction.

Moreover, our results showed that Pt catalysts had the highest CO_2 generation ability at the low potential (0.5 V), while Pt/SnO_2 showed the highest CO_2 generation at the high potential (1.0 V). This result again supported our hypothesis that at low potentials the CO_2 generation could be limited by the supply of *OH from water dissociation, while at high potentials Rh strongly interacted with water and could resulted in the dissolution and/or poisoning of the Rh site. Thus, Pt/SnO_2 appeared to the best catalysts since the SnO_2 shell mitigated the *OH poisoning and/or leaching.

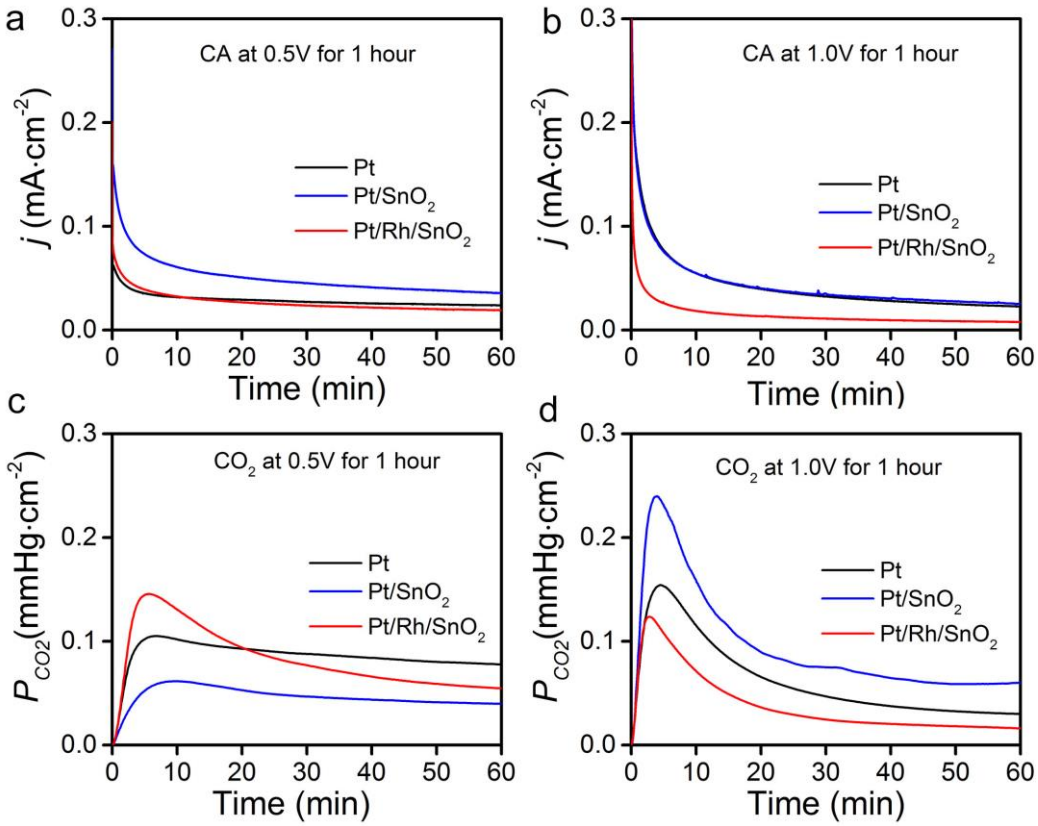

Figure 5.12 (a) CA and (c) CO_2 generation curves at 0.5 V for an hour of carbon supported Pt(ETEK), Pt/SnO_2 and $Pt/Rh/SnO_2$ catalysts. (b) CA and (d) CO_2 generation curves at 1.0 V for an hour of carbon supported Pt(ETEK), Pt/SnO_2 and $Pt/Rh/SnO_2$ catalysts.

It is important to point out that although Pt dissolution readily happens during the EOR at a constant high potential range with a dissolution rate of 2.2×10^{-14} g/(cm^2·s) as shown

from Mayrhofer's work recently [221]. **Figure 5.13** a and b show the time resolved dissolution profile of Pt during CV scans in 0.1 M $HClO_4$ at the scan rate of 10 mV/s. (Reprinted from Figure 1: Topalov, *et al*. *Angew. Chem. Int. Ed.* 51 (2012) 12613.) and the resulting current from the dissolution of Pt extracted from **Figure 5.13** a. **Figure 5.13** c shows the LSV curves of EOR on Pt/C(ETEK) at the scan rate of 0.5 mV/s (black curve) and 50 mV/s (purple curve) and the current resulted from the dissolution of Pt polycrystalline (anodic scan) in **Figure 5.13** b (blue curve), and electrochemical current on a Pt(111) electrode in 0.1 M $HClO_4$ at the scan rate of 50 mV/s(yellow curve). (Reprinted from Figure 2b: Huang, *et al*. *Nat. Commun.* 7 (2016) 12440). **Figure 5.13** d shows CA curves of EOR on Pt/C (ETEK) at 0.5 V (red curve) and 1.0 V (black curve); the calculated current from dissolution of Pt/C (4.8 nm) at 0.69 V in 0.1 M $HClO_4$ (blue curve). (Reprinted from Table 1: Cherevko, *et al*. *ChemElectroChem* 2 (2015) 1471.)

Our calculations showed that the observed EOR current densities in this study were nearly 6 orders of magnitude higher than the current density attributed to the Pt dissolution (**Figure 5.13**). We also compared our linear sweep voltammetry (LSV) data with the recent work from Koper's group, where the formation of OH on the surface of single crystal Pt (111) were related to the interaction of between ClO_4^- and the OH_{ads}. Taking the peak current density at ~ 0.8 V vs RHE (corresponding to 0.6 V vs Ag/AgCl) as a result of Pt dissolution as shown in Koper's work (of course this is a very rough approximation as the oxidized Pt upon anodic scan might not be completely dissolved, meanwhile a certain portion of the current should be attributed to the capacitive process), we found that the peak current density from the EOR measured at the same scan rate (50 mV/s) in our study was 7.7 times higher than the current density from the Pt dissolution as shown in

Figure 5.13 c. Therefore, our EOR results and the studies of *OH adsorbates on CO_2 generation were not affected by Pt dissolution during the high potential reaction.

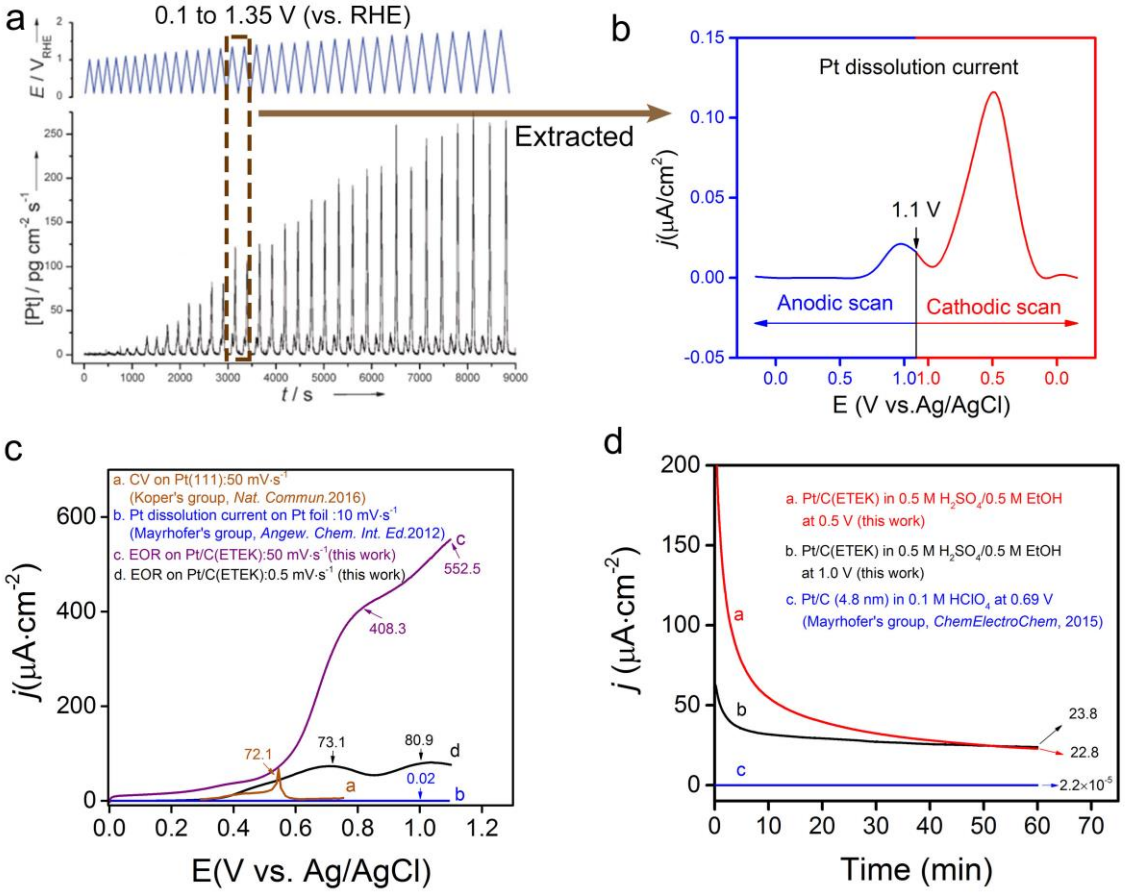

Figure 5.13 Comparative study of Pt dissolution from the related references. (Copyright 2012 WILEY - VCH VERLAG GMBH & CO. KGAA)

5.7 DISCUSSION

The scheme presented in **Figure 5.14** describes the comprehensive understanding of the mechanism underlying the formation of CO_2 during the EOR, where the influence of *OH adsorbates plays a very important role in the electro-kinetics of CO_2 generation. At low potentials (0.1 to 0.2 V), C-C bond splitting of ethanol could already take place. However, the resulting C_1 species (e.g. *CH_x and *CO) cannot be oxidized completely

into CO_2 since dissociative adsorption of water at low potentials was sluggish.[62] Therefore, the reaction intermediates (C_1 species) poisoned active sites, which explained the observed low current density and nearly zero CO_2 generation observed from the CVs below 0.2 V, as shown in **Figure 5.7**. When the potential increased (> 0.2 V), *OH started to be generated from the dissociation of water, which helped the oxidization of C_1 species and the generation of CO_2. The observed threshold for CO_2 generation at 0.2 V in this study was also reported previously through *in situ* FTIR studies.[35, 143, 203, 222] Therefore, we concluded that at low potentials (0.1 to 0.46 V), the limited supply of *OH adsorbates as a result of water dissociation was the rate limiting step, which resulted in the insufficient removal of C_1 species generated at low potentials. In this context, Pt/Rh/SnO_2 was a better catalyst for CO_2 generation than Pt and Pt/SnO_2, evidenced by fact that its onset potential for CO_2 generation was around 11 mV and 64 mV lower than Pt/SnO_2 and Pt, respectively. The superamacy of Pt/Rh/SnO_2 for EOR at low potentials is because Rh component faciliated the C-C splitting via promoting the dehydrogenation of the β-C-H bond, and SnO_2 component helped the dissociative adsorption of water to form *OH to remove the C_1 species generated from the C-C bond splitting. Our results on the CO_2 generation at the low potential range (0.1 to 0.46 V) are in agreement with recent EOR mechanistic studies on the mesoporous Pt electrode using a newly designed electrochemical mass spectrometer (EC-MS) by Pastor's group [223]. Their comprehensive EC-MS studies showed that at a relatively low potential region, CH_4 and even C_2H_6 were detected due to the lack of *OH species from water dissociation.

On the other hand, at higher potentials (0.46 to 1.1 V), the S_{CO2} values of Pt/Rh/SnO_2 and Pt were close to zero, in which region the presence of *OH adsorbates was

considerably enhanced due to the dissociative adsorption of water at higher potentials.[224] The resulting excess amount of *OH adsorbates could poison active sites. In particularly, Rh sites were more prone to be poisoned since they were more susceptible to *OH coverage than Pt. The poisoned Rh averted β-dehydrogenation of ethanol, and resulted in the sharp decrease in CO_2 generation. Meanwhile, the overall charge transfer rate was dominated by α-dehydrogenation primarily on Pt sites which were not severely blocked by *OH adsorbates. Consequently, j_{CO2} and S_{CO2} of Pt and Pt/Rh/SnO_2 decreased drastically when the potential was higher than 0.46 V. The higher j_{CO2} and S_{CO2} of Pt/SnO_2, compared with Pt and Pt/Rh/SnO_2 indicated that the addition of Sn (in the form of SnO_2) onto the Pt surface seemed to mitigate the *OH poisoning of the Pt sites since dissociative adsorption of water might prefer to take place at the Sn sites instead of Pt sites, while the Rh sites were much more vulnerable to *OH poisoning even in the presence of SnO_2.

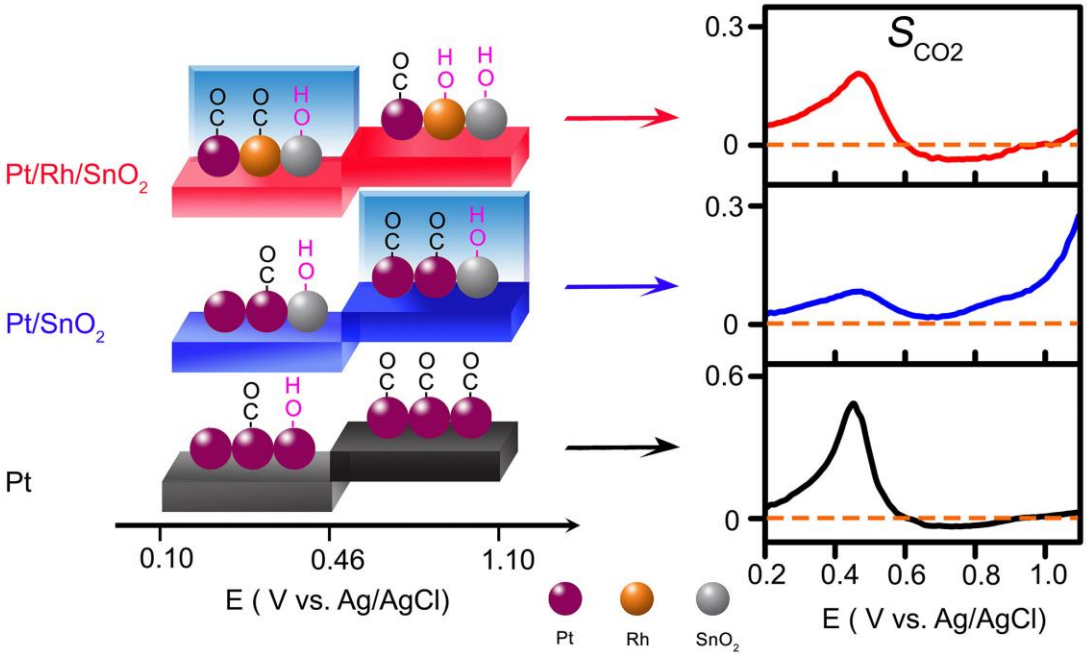

Figure 5.14 Schematic of the electrooxidation of ethanol on catalysts from 0.1 to 1.1 V.

The adsorption energies of H_2O and *OH adsorbates on various surfaces show that addition of SnO_2 to Pt or PtRh decreases the *OH adsorption energy dramatically to stabilize *OH. The results clearly indicate that a core-shell particle with a SnO_2 shell can offer more adsorption sites for *OH to enhance the oxidation of ethanol and/or reaction intermediates compared with Pt.

CHAPTER 6

SUMMARY

In this study, we first developed a four-electrode electrochemical cell for measuring CO_2 generation with high accuracy. Assisted by the high sensitivity of the CO_2 microelectrode and unique CO_2 *in situ* cell design, we obtained the high resolutionCO_2 signal during the electrooxidation of ethanol on the various catalysts. Hence, the kinetic information including the CO_2 generation rate and selectivity can be calculated, providing great insight on the reaction mechanisms of the EOR.

The Pt/Rh/Sn catalyst with a partially oxidized Pt and Rh core and a SnO_2 shell and the Pt/Rh/Sn catalyst with a Pt and Rh metallic core and a SnO_2 shell were synthesized with "surfactant free" method with/without post-treatment in hydrogen gas. Complementary characterization techniques including TEM, EDXS, STEM-EELS, XRD, EXAFS and XANES were used to identify the heterogeneous structure of $Pt_{37}Rh_{20}O_{21}$-$(SnO_2)_{43}$ and $Pt_{37}Rh_{20}O_{21}$-$(SnO_2)_{43}$. *In situ* CO_2 measurements and kinetic analyses show that, for the first time, the tri–phase $PtRhO_x$-SnO_2 catalysts with a partially oxidized Pt and Rh core and a SnO_2 shell coincided with a 2.5-fold increase in the CO_2 generation rate towards the ethanol oxidation reaction, compared with the bi-phase PtRh-SnO_2 catalysts with a metallic PtRh alloy core and commercial Pt. These studies provided insight on the design of a new genre of electro-catalysts with a partially oxidized noble metal.

Carbon-supported monometallic Pt, binary Pt/SnO_2, and ternary Pt/Rh/SnO_2 nanoparticles from 2 to 3 nm were prepared using a surfactant-free seeded growth approach. Several characterization techniques, including TEM, STEM-EELS, XRD,

XANES, EDXS, were employed to elucidate the heterogeneous structure of the catalyst as Pt or Pt-Rh core and SnO_2 shell core/shell particles. DFT calculations also provided insight on the surface reactions and intermediates.

A combination of electrochemical measurements and *in situ* CO_2 microelectrode was used to investigate the catalytic properties of the Pt, Pt/SnO_2, and Pt/Rh/SnO_2 electrocatalysts for the electro-oxidation of ethanol. A newly developed electrochemical cell equipped with a highly sensitive CO_2 microelectrode not only measured the catalytic activities of all three catalysts for the EOR, but also analyzed quantitatively the potentiodynamics of the EOR such as partial pressure, generation rate and selectivity towards CO_2 production. Our studies, for the first time, revealed the influences of *OH adsorbates on the CO_2 generation rate and selectivity: at low potentials (0.1 V to 0.46 V), the CO_2 generation was limited by water dissociation, Pt/Rh/SnO_2 was a better EOR catalyst than Pt and Pt/SnO_2 due to the promotional roles of the Rh component on C-C splitting and of the SnO_2 component on the formation *OH, showing much lower onset potential for CO_2 generation than Pt and Pt/SnO_2. On the other hand, at high potentials (0.46 to 1.1 V), the Rh component strongly interacted with water and could result in the dissolution and/or poisoning of the Rh site. Thus Pt/SnO_2 exhibited the best performance toward CO_2 generation, evidenced by our well designed *OH adsorbates experiments. The findings presented in this thesis provide fundamental insight on the EOR electro-catalysis and help in designing novel nanostructured materials with enhanced activity and selectivity in the ethanol electro-oxidation.

LIST OF REFERENCES

1. Adams, T.A.; Nease, J.; Tucker, D.; and Barton, P.I. Energy conversion with solid oxide fuel cell systems: A review of concepts and outlooks for the short- and long-term. *Industrial & Engineering Chemistry Research,* **2013**, 52(9), 3089-3111.

2. Bischoff, M. Molten carbonate fuel cells: A high temperature fuel cell on the edge to commercialization. *Journal of Power Sources,* **2006**, 160(2), 842-845.

3. Sammes, N.; Bove, R.; and Stahl, K. Phosphoric acid fuel cells: Fundamentals and applications. *Current Opinion in Solid State and Materials Science,* **2004**, 8(5), 372-378.

4. Merle, G.; Wessling, M.; and Nijmeijer, K. Anion exchange membranes for alkaline fuel cells: A review. *Journal of Membrane Science,* **2011**, 377(1), 1-35.

5. Ramírez-Salgado, J. Study of basic biopolymer as proton membrane for fuel cell systems. *Electrochimica Acta,* **2007**, 52(11), 3766-3778.

6. Pierluigi Barbaro and Bianchini, C. The direct ethanol fuel cell: A challenge to convert bioethanol cleanly into electric energy. *Catalysis for Sustainable Energy Production,* **2009**, 1-46.

7. C. Marie, G.L. Researches on the electrolytic oxidation of various organic substances. *Journal de Chimie Physique et de Physico-Chimie Biologique,* **1929**, 26(2), 237-249.

8. Bogdanovskii, G. and Shlygin, A.I. Mechanism for the electrooxidation of alcohols and aldehydes on platinum. III. Form of the polarization curves of the oxidation of ethyl alcohol. *Zhurnal Fizicheskoi Khimii,* **1960**, 34(1), 57-62.

9. Rightmire, R.A.; Rowland, R.L.; Boos, D.L.; and Beals, D.L. Ethyl alcohol oxidation at platinum electrodes. *Journal of the Electrochemical Society,* **1964**, 111(2), 242-247.

10. Blake, A.R.; Kuhn, A.T.; and Sunderla.Jg. Low potential oxidation of ethanol on bright platinum. *Journal of the Electrochemical Society,* **1973**, 120(4), 492-497.

11. Snell, K.D. and Keenan, A.G. Chloride inhibition of ethanol electrooxidation at a platinum electrode in aqueous acid solution. *Electrochimica Acta,* **1981**, 26(9), 1339-1344.

12. Liang, C. and Franklin, T.C. The electrolytic oxidation of simple aldehydes and alcohols at platinum electrodes. *Electrochimica Acta,* **1964**, 9(5), 517-530.

13. Sokolova, E. Einfluss der natur der alkohole auf den mechanismus ihrer elektrooxidation. *Electrochimica Acta,* **1975**, 20(5), 323-330.

14. Willsau, J. and Heitbaum, J. Elementary steps of ethanol oxidation on Pt in sulfuric acid as evidenced by isotope labelling. *Journal of Electroanalytical Chemistry and Interfacial Electrochemistry,* **1985**, 194(1), 27-35.

15. Iwasita, T. and Vielstich, W. The electrochemical oxidation of ethanol on platinum: A SNIFTIRS study. *Journal of Electroanalytical Chemistry and Interfacial Electrochemistry,* **1988**, 257(1), 319-324.

16. Caram, J.A. and Gutiérrez, C. Cyclic voltammetric and potential-modulated reflectance spectroscopic study of the electroadsorption of methanol and ethanol on a platinum electrode in acid and alkaline media. *Journal of Electroanalytical Chemistry,* **1992**, 323(1), 213-230.

17. Perez, J.; Paganin, V.A.; and Antolini, E. Particle size effect for ethanol electro-oxidation on Pt/C catalysts in half-cell and in a single direct ethanol fuel cell. *Journal of Electroanalytical Chemistry,* **2011**, 654(1), 108-115.

18. Sun, C.L.; Tang, J.S.; Brazeau, N.; Wu, J.J.; Ntais, S.; Yin, C.W.; Chou, H.L.; and Baranova, E.A. Particle size effects of sulfonated graphene supported Pt nanoparticles on ethanol electrooxidation. *Electrochimica Acta,* **2015**, 162, 282-289.

19. Dong, L.; Gari, R.R.S.; Li, Z.; Craig, M.M.; and Hou, S. Graphene-supported platinum and platinum–ruthenium nanoparticles with high electrocatalytic activity for methanol and ethanol oxidation. *Carbon,* **2010**, 48(3), 781-787.

20. Rao, L.; Jiang, Y.X.; Zhang, B.W.; Cai, Y.R.; and Sun, S.G. High activity of cubic PtRh alloys supported on graphene towards ethanol electrooxidation. *Physical Chemistry Chemical Physics,* **2014**, 16(27), 13662-13671.

21. Li, Y.Y.; Rao, L.; Jiang, Y.X.; Liu, Z.L.; He, C.L.; Zhang, B.W.; and Sun, S.G. Electrooxidation of ethanol on platinum nanocubes supported on multi-walled carbon nanotubes. *Chemical Journal of Chinese Universities-Chinese,* **2013**, 34(2), 408-413.

22. Ryan, S.H.; Drew, H.; and Zhongwei, C. Tin-oxide-coated single-walled carbon nanotube bundles supporting platinum electrocatalysts for direct ethanol fuel cells. *Nanotechnology,* **2010**, 21(16), 165705.

23. Gao, G.; Yang, G.; Xu, M.; Wang, C.; Xu, C.; and Li, H. Simple synthesis of Pt nanoparticles on noncovalent functional MWNT surfaces: Application in ethanol electrocatalysis. *Journal of Power Sources,* **2007**, 173(1), 178-182.

24. Chen, M.H.; Jiang, Y.X.; Chen, S.R.; Huang, R.; Lin, J.L.; Chen, S.P.; and Sun, S.G. Synthesis and durability of highly dispersed platinum nanoparticles supported on ordered mesoporous carbon and their electrocatalytic properties for ethanol oxidation. *The Journal of Physical Chemistry C,* **2010**, 114(44), 19055-19061.

25. Iwasita, T. and Pastor, E. A DEMS and FTIR spectroscopic investigation of adsorbed ethanol on polycrystalline platinum. *Electrochimica Acta,* **1994**, 39(4), 531-537.

26. Beden, B.; Morin, M.C.; Hahn, F.; and Lamy, C. “In situ” analysis by infrared reflectance spectroscopy of the adsorbed species resulting from the electrosorption of ethanol on platinum in acid medium. *Journal of Electroanalytical Chemistry and Interfacial Electrochemistry,* **1987**, 229(1), 353-366.

27. Holze, R. On the adsorption and oxidation of ethanol on platinum as studied with in-situ IR spectroscopy. *Journal of Electroanalytical Chemistry and Interfacial Electrochemistry,* **1988**, 246(2), 449-455.

28. Leung, L.W.H.; Chang, S.C.; and Weaver, M.J. Real-time FTIR spectroscopy as an electrochemical mechanistic probe: Electrooxidation of ethanol and related species on well-defined Pt (111) surfaces. *Journal of Electroanalytical Chemistry and Interfacial Electrochemistry,* **1989**, 266(2), 317-336.

29. Chang, S.C.; Leung, L.W.H.; and Weaver, M.J. Metal crystallinity effects in electrocatalysis as probed by real-time FTIR spectroscopy: Electrooxidation of formic acid, methanol, and ethanol on ordered low-index platinum surfaces. *The Journal of Physical Chemistry,* **1990**, 94(15), 6013-6021.

30. Shin, J.; Tornquist, W.J.; Korzeniewski, C.; and Hoaglund, C.S. Elementary steps in the oxidation and dissociative chemisorption of ethanol on smooth and stepped surface planes of platinum electrodes. *Surface Science,* **1996**, 364(2), 122-130.

31. Tarnowski, D.J. and Korzeniewski, C. Effects of surface step density on the electrochemical oxidation of ethanol to acetic acid. *Journal of Physical Chemistry B,* **1997**, 101(2), 253-258.

32. Tarnowski, D.J. and Korzeniewski, C. Amperometric detection with membrane-based sampling for percent-level determinations of ethanol. *Analytica Chimica Acta,* **1996**, 332(2-3), 111-121.

33. Lai, S.C.S. and Koper, M.T.M. The influence of surface structure on selectivity in the ethanol electro-oxidation reaction on platinum. *Journal of Physical Chemistry Letters,* **2010**, 1(7), 1122-1125.

34. Lai, S.C.S. and Koper, M.T.M. Electro-oxidation of ethanol and acetaldehyde on platinum single-crystal electrodes. *Faraday Discussions,* **2008**, 140, 399-416.

35. Xia, X.H.; Liess, H.D.; and Iwasita, T. Early stages in the oxidation of ethanol at low index single crystal platinum electrodes. *Journal of Electroanalytical Chemistry,* **1997**, 437(1), 233-240.

36. Colmati, F.; Tremiliosi-Filho, G.; Gonzalez, E.R.; Berna, A.; Herrero, E.; and Feliu, J.M. Surface structure effects on the electrochemical oxidation of ethanol on platinum single crystal electrodes. *Faraday Discussions,* **2008**, 140, 379-397.

37. Colmati, F.; Tremiliosi, G.; Gonzalez, E.R.; Berna, A.; Herrero, E.; and Feliu, J.M. The role of the steps in the cleavage of the C-C bond during ethanol oxidation on platinum electrodes. *Physical Chemistry Chemical Physics,* **2009**, 11(40), 9114-9123.

38. Ferre-Vilaplana, A.; Buso-Rogero, C.; Feliu, J.M.; and Herrero, E. Cleavage of the C-C bond in the ethanol oxidation reaction on platinum. Insight from experiments and calculations. *Journal of Physical Chemistry C,* **2016**, 120(21), 11590-11597.

39. Shin, J.W. and Korzeniewski, C. Step density effects on adsorption and reactivity of small molecules at platinum single crystal electrodes. *Proceedings of the Sixth International Symposium on Electrode Processes,* **1996**, 96(8), 291-302.

40. Busó-Rogero, C.; Brimaud, S.; Solla-Gullon, J.; Vidal-Iglesias, F.J.; Herrero, E.; Behm, R.J.; and Feliu, J.M. Ethanol oxidation on shape-controlled platinum nanoparticles at different pHs: A combined in situ IR spectroscopy and online mass spectrometry study. *Journal of Electroanalytical Chemistry,* **2016**, 763, 116-124.

41. Tian, N.; Zhou, Z.Y.; Sun, S.G.; Ding, Y.; and Wang, Z.L. Synthesis of tetrahexahedral platinum nanocrystals with high-index facets and high electro-oxidation activity. *Science,* **2007**, 316(5825), 732-735.

42. Zhou, Z.Y.; Huang, Z.Z.; Chen, D.J.; Wang, Q.; Tian, N.; and Sun, S.G. High-index faceted platinum nanocrystals supported on carbon black as highly efficient catalysts for ethanol electrooxidation. *Angewandte Chemie International Edition,* **2010**, 49(2), 411-414.

43. Liu, S.; Tian, N.; Xie, A.Y.; Du, J.H.; Xiao, J.; Liu, L.; Sun, H.Y.; Cheng, Z.Y.; Zhou, Z.Y.; and Sun, S.G. Electrochemically seed-mediated synthesis of sub-10 nm tetrahexahedral Pt nanocrystals supported on graphene with improved catalytic performance. *Journal of the American Chemical Society,* **2016**, 138(18), 5753-5756.

44. Camara, G.A. and Iwasita, T. Parallel pathways of ethanol oxidation: The effect of ethanol concentration. *Journal of Electroanalytical Chemistry,* **2005**, 578(2), 315-321.

45. Fujiwara, N.; Friedrich, K.A.; and Stimming, U. Ethanol oxidation on PtRu electrodes studied by differential electrochemical mass spectrometry. *Journal of Electroanalytical Chemistry,* **1999**, 472(2), 120-125.

46. Del Colle, V.; Berna, A.; Tremiliosi, G.; Herrero, E.; and Feliu, J.M. Ethanol electrooxidation onto stepped surfaces modified by Ru deposition: Electrochemical and spectroscopic studies. *Physical Chemistry Chemical Physics,* **2008**, 10(25), 3766-3773.

47. Datta, J.; Singh, S.; Das, S.; and Bandyopadhyay, N.R. A comprehensive study on the effect of Ru addition to Pt electrodes for direct ethanol fuel cell. *Bulletin of Materials Science,* **2009**, 32(6), 643-652.

48. Spinace, E.V.; Neto, A.O.; Vasconcelos, T.R.R.; and Linardi, M. Electro-oxidation of ethanol using PtRu/C electrocatalysts prepared by alcohol-reduction process. *Journal of Power Sources,* **2004**, 137(1), 17-23.

49. Chatterjee, M.; Chatterjee, A.; Ghosh, S.; and Basumallick, I. Electro-oxidation of ethanol and ethylene glycol on carbon-supported nano-Pt and -PtRu catalyst in acid solution. *Electrochimica Acta,* **2009**, 54(28), 7299-7304.

50. Neto, A.O.; Giz, M.J.; Perez, J.; Ticianelli, E.A.; and Gonzalez, E.R. The electro-oxidation of ethanol on Pt-Ru and Pt-Mo particles supported on high-surface-area carbon. *Journal of the Electrochemical Society,* **2002**, 149(3), A272-A279.

51. Neto, A.O.; Verjulio-Silva, R.W.R.; Linardi, M.; and Spinace, E.V. Preparation of PtRu/C electrocatalysts using citric acid as reducing agent and OH- ions as stabilizing agent for

direct alcohol fuel cell (DAFC). *International Journal of Electrochemical Science,* **2009**, 4(7), 954-961.

52. Camara, G.A.; de Lima, R.B.; and Iwasita, T. Catalysis of ethanol electrooxidation by PtRu: The influence of catalyst composition. *Electrochemistry Communications,* **2004**, 6(8), 812-815.

53. Lee, C.-G.; Ojima, H.; and Umeda, M. Electrooxidation of C_1 to C_3 alcohols with Pt and Pt–Ru sputter deposited interdigitated array electrodes. *Electrochimica Acta,* **2008**, 53(7), 3029-3035.

54. Velázquez-Palenzuela, A.; Brillas, E.; Arias, C.; Centellas, F.; Garrido, J.A.; Rodríguez, R.M.; and Cabot, P.-L. Carbon monoxide, methanol and ethanol electro-oxidation on Ru-decorated carbon-supported Pt nanoparticles prepared by spontaneous deposition. *Journal of Power Sources,* **2013**, 225, 163-171.

55. Sen, S.; Sen, F.; and Gokagac, G. Preparation and characterization of nano-sized Pt-Ru/C catalysts and their superior catalytic activities for methanol and ethanol oxidation. *Physical Chemistry Chemical Physics,* **2011**, 13(15), 6784-6792.

56. Pires, F.I.; Corradini, P.G.; Paganin, V.A.; Antolini, E.; and Perez, J. Effect of the degree of alloying of PtRu/C (1:1) catalysts on ethanol oxidation. *Ionics,* **2013**, 19(7), 1037-1045.

57. Zhao, Y.; Maswadeh, Y.; Shan, S.; Cronk, H.; Skeete, Z.; Prasai, B.; Luo, J.; Petkov, V.; and Zhong, C.-J. Composition–structure–activity correlation of platinum–ruthenium nanoalloy catalysts for ethanol oxidation reaction. *The Journal of Physical Chemistry C,* **2017**, 121(32), 17077-17087.

58. Simões, F.C.; dos Anjos, D.M.; Vigier, F.; Léger, J.M.; Hahn, F.; Coutanceau, C.; Gonzalez, E.R.; Tremiliosi-Filho, G.; de Andrade, A.R.; Olivi, P.; and Kokoh, K.B. Electroactivity of tin modified platinum electrodes for ethanol electrooxidation. *Journal of Power Sources,* **2007**, 167(1), 1-10.

59. Purgato, F.L.S.; Olivi, P.; Léger, J.M.; de Andrade, A.R.; Tremiliosi-Filho, G.; Gonzalez, E.R.; Lamy, C.; and Kokoh, K.B. Activity of platinum–tin catalysts prepared by the Pechini–Adams method for the electrooxidation of ethanol. *Journal of Electroanalytical Chemistry,* **2009**, 628(1), 81-89.

60. Zheng, Q.W.; Fan, C.J.; Zhen, C.H.; Zhou, Z.Y.; and Sun, S.G. Irreversible adsorption of Sn adatoms on basal planes of Pt single crystal and its impact on electrooxidation of ethanol. *Electrochimica Acta,* **2008**, 53(21), 6081-6088.

61. Mostafa, E.; Abd-El-Latif, A.E.; Ilsley, R.; Attard, G.; and Baltruschat, H. Quantitative DEMS study of ethanol oxidation: Effect of surface structure and Sn surface modification. *Physical Chemistry Chemical Physics,* **2012**, 14(46), 16115-16129.

62. Jin, J.M.; Sheng, T.; Lin, X.; Kavanagh, R.; Hamer, P.; Hu, P.; Hardacre, C.; Martinez Bonastre, A.; Sharman, J.; Thompsett, D.; and Lin, W.F. The origin of high activity but low CO_2 selectivity on binary PtSn in the direct ethanol fuel cell. *Physical Chemistry Chemical Physics,* **2014**, 16(20), 9432-9440.

63. Rizo, R.; Lázaro, M.J.; Pastor, E.; and Koper, M.T.M. Ethanol oxidation on Sn-modified Pt single-crystal electrodes: New mechanistic insights from on-line electrochemical mass spectrometry. *ChemElectroChem,* **2016**, 3(12), 2196-2201.

64. Wang, Q.; Sun, G.Q.; Jiang, L.H.; Xin, Q.; Sun, S.G.; Jiang, Y.X.; Chen, S.P.; Jusys, Z.; and Behm, R.J. Adsorption and oxidation of ethanol on colloid-based Pt/C, PtRu/C and Pt_3Sn/C catalysts: In situ FTIR spectroscopy and on-line DEMS studies. *Physical Chemistry Chemical Physics,* **2007**, 9(21), 2686-2696.

65. Rizo, R.; Arán-Ais, R.M.; Padgett, E.; Muller, D.A.; Lázaro, M.J.; Solla-Gullón, J.; Feliu, J.M.; Pastor, E.; and Abruña, H.D. Pt-rich core/Sn-rich subsurface/Pt skin nanocubes as highly active and stable electrocatalysts for the ethanol oxidation reaction. *Journal of the American Chemical Society,* **2018**, 140(10), 3791-3197.

66. Du, W.; Yang, G.; Wong, E.; Deskins, N.A.; Frenkel, A.I.; Su, D.; and Teng, X. Platinum-tin oxide core–shell catalysts for efficient electro-oxidation of ethanol. *Journal of the American Chemical Society,* **2014**, 136(31), 10862-10865.

67. Spinacé, E.V.; Linardi, M.; and Neto, A.O. Co-catalytic effect of nickel in the electro-oxidation of ethanol on binary Pt–Sn electrocatalysts. *Electrochemistry Communications,* **2005**, 7(4), 365-369.

68. Jiang, L.; Colmenares, L.; Jusys, Z.; Sun, G.Q.; and Behm, R.J. Ethanol electrooxidation on novel carbon supported $Pt/SnO_x/C$ catalysts with varied Pt:Sn ratio. *Electrochimica Acta,* **2007**, 53(2), 377-389.

69. López-Suárez, F.E.; Carvalho-Filho, C.T.; Bueno-López, A.; Arboleda, J.; Echavarría, A.; Eguiluz, K.I.B.; and Salazar-Banda, G.R. Platinum–tin/carbon catalysts for ethanol oxidation: Influence of Sn content on the electroactivity and structural characteristics. *International Journal of Hydrogen Energy,* **2015**, 40(37), 12674-12686.

70. Antoniassi, R.M.; Silva, J.C.M.; Oliveira Neto, A.; and Spinacé, E.V. Synthesis of $Pt+SnO_2/C$ electrocatalysts containing Pt nanoparticles with preferential (100) orientation for direct ethanol fuel cell. *Applied Catalysis B: Environmental,* **2017**, 218, 91-100.

71. Almeida, T.S.; Palma, L.M.; Leonello, P.H.; Morais, C.; Kokoh, K.B.; and De Andrade, A.R. An optimization study of PtSn/C catalysts applied to direct ethanol fuel cell: Effect of the preparation method on the electrocatalytic activity of the catalysts. *Journal of Power Sources,* **2012**, 215, 53-62.

72. Song, P.; Cui, X.; Shao, Q.; Feng, Y.; Zhu, X.; and Huang, X. Networked Pt-Sn nanowires as efficient catalysts for alcohol electrooxidation. *Journal of Materials Chemistry A,* **2017**, 5(47), 24626-24630.

73. Jiang, L.; Sun, G.; Sun, S.; Liu, J.; Tang, S.; Li, H.; Zhou, B.; and Xin, Q. Structure and chemical composition of supported Pt–Sn electrocatalysts for ethanol oxidation. *Electrochimica Acta,* **2005**, 50(27), 5384-5389.

74. de Tacconi, N.R.; Lezna, R.O.; Beden, B.; Hahn, F.; and Lamy, C. In-situ FTIR study of the electrocatalytic oxidation of ethanol at iridium and rhodium electrodes. *Journal of Electroanalytical Chemistry,* **1994**, 379(1), 329-337.

75. Caram, J.A. and Gutiérrez, C. Study by cyclic voltammetry and potential-modulated reflectance spectroscopy of the electroadsorption of methanol and ethanol on a rhodium electrode in acid and alkaline media. *Journal of Electroanalytical Chemistry,* **1992**, 336(1), 309-328.

76. Méndez, E.; Rodríguez, J.L.; Arévalo, M.C.; and Pastor, E. Comparative study of ethanol and acetaldehyde reactivities on rhodium electrodes in acidic media. *Langmuir,* **2002**, 18(3), 763-772.

77. Cantane, D.A.; Ambrosio, W.F.; Chatenet, M.; and Lima, F.H.B. Electro-oxidation of ethanol on Pt/C, Rh/C, and Pt/Rh/C-based electrocatalysts investigated by on-line DEMS. *Journal of Electroanalytical Chemistry,* **2012**, 681, 56-65.

78. Bach Delpeuch, A.; Maillard, F.; Chatenet, M.; Soudant, P.; and Cremers, C. Ethanol oxidation reaction (EOR) investigation on Pt/C, Rh/C, and Pt-based bi- and tri-metallic electrocatalysts: A DEMS and in situ FTIR study. *Applied Catalysis B: Environmental,* **2016**, 181, 672-680.

79. de Souza, J.P.I.; Queiroz, S.L.; Bergamaski, K.; Gonzalez, E.R.; and Nart, F.C. Electro-oxidation of ethanol on Pt, Rh, and PtRh electrodes. A study using DEMS and in-situ FTIR techniques. *The Journal of Physical Chemistry B,* **2002**, 106(38), 9825-9830.

80. Lima, F.H.B.; Profeti, D.; Lizcano-Valbuena, W.H.; Ticianelli, E.A.; and Gonzalez, E.R. Carbon-dispersed Pt–Rh nanoparticles for ethanol electro-oxidation. Effect of the crystallite size and of temperature. *Journal of Electroanalytical Chemistry,* **2008**, 617(2), 121-129.

81. Sen Gupta, S. and Datta, J. A comparative study on ethanol oxidation behavior at Pt and PtRh electrodeposits. *Journal of Electroanalytical Chemistry,* **2006**, 594(1), 65-72.

82. Fang, L.; He, J.; Saipanya, S.; and Huang, X. Preparation of Rh_5@Ptx/C core-shell nanoparticles for electrocatalytic oxidation of ethanol. *International Journal of Electrochemical Science,* **2015**, 10, 5350-5357.

83. Yuan, Q.; Zhou, Z.; Zhuang, J.; and Wang, X. Seed displacement, epitaxial synthesis of Rh/Pt bimetallic ultrathin nanowires for highly selective oxidizing ethanol to CO_2. *Chemistry of Materials,* **2010**, 22(7), 2395-2402.

84. Shen, Y.; Gong, B.; Xiao, K.; and Wang, L. In situ assembly of ultrathin PtRh nanowires to graphene nanosheets as highly efficient electrocatalysts for the oxidation of ethanol. *ACS Applied Materials & Interfaces,* **2017**, 9(4), 3535-3543.

85. Oliveira, R.T.S.; Santos, M.C.; Marcussi, B.G.; Nascente, P.A.P.; Bulhões, L.O.S.; and Pereira, E.C. The use of a metallic bilayer for the oxidation of small organic molecules. *Journal of Electroanalytical Chemistry,* **2005**, 575(2), 177-182.

86. Delpeuch, A.B.; Asset, T.; Chatenet, M.; and Cremers, C. Electrooxidation of ethanol at room temperature on carbon-supported Pt and Rh-containing catalysts: A DEMS study. *Journal of the Electrochemical Society,* **2014**, 161(9), F918-F924.

87. Brandalise, M.; Verjulio-Silva, R.W.R.; Tusi, M.M.; Correa, O.V.; Farias, L.A.; Linardi, M.; Spinace, E.V.; and Neto, A.O. Electro-oxidation of ethanol using PtRuBi/C electrocatalyst prepared by borohydride reduction. *Ionics,* **2009**, 15(6), 743-747.

88. Du, W.; Su, D.; Wang, Q.; Frenkel, A.I.; and Teng, X. Promotional effects of bismuth on the formation of platinum-bismuth nanowires network and the electrocatalytic activity toward ethanol oxidation. *Crystal Growth & Design,* **2011**, 11(2), 594-599.

89. Sahin, O.; Kivrak, H.; Karaman, M.; and Atbas, D. The effect of iridium addition to platinum on the alcohol electrooxidation activity. *American Journal of Materials Science and Engineering,* **2015**, 3(1), 15-20.

90. Tayal, J.; Rawat, B.; and Basu, S. Bi-metallic and tri-metallic Pt–Sn/C, Pt–Ir/C, Pt–Ir–Sn/C catalysts for electro-oxidation of ethanol in direct ethanol fuel cell. *International Journal of Hydrogen Energy,* **2011**, 36(22), 14884-14897.

91. Pacheco Santos, V.; Del Colle, V.; Batista de Lima, R.; and Tremiliosi-Filho, G. FTIR study of the ethanol electrooxidation on Pt(100) modified by osmium nanodeposits. *Langmuir,* **2004**, 20(25), 11064-11072.

92. Del Colle, V. and Tremiliosi-Filho, G. Electrochemical and spectroscopic studies of ethanol and acetaldehyde oxidation onto Pt(110) modified by osmium. *Electrocatalysis,* **2011**, 2(4), 285-296.

93. Pacheco Santos, V. and Tremiliosi-Filho, G. Effect of osmium coverage on platinum single crystals in the ethanol electrooxidation. *Journal of Electroanalytical Chemistry,* **2003**, 554-555, 395-405.

94. Tayal, J.; Rawat, B.; and Basu, S. Effect of addition of rhenium to Pt-based anode catalysts in electro-oxidation of ethanol in direct ethanol PEM fuel cell. *International Journal of Hydrogen Energy,* **2012**, 37(5), 4597-4605.

95. Zhang, B.W.; Sheng, T.; Wang, Y.X.; Qu, X.M.; Zhang, J.M.; Zhang, Z.C.; Liao, H.G.; Zhu, F.C.; Dou, S.X.; Jiang, Y.X.; and Sun, S.G. Platinum–cobalt bimetallic nanoparticles with Pt skin for electro-oxidation of ethanol. *ACS Catalysis,* **2017**, 7(1), 892-895.

96. Sulaiman, J.E.; Zhu, S.; Xing, Z.; Chang, Q.; and Shao, M. Pt–Ni octahedra as electrocatalysts for the ethanol electro-oxidation reaction. *ACS Catalysis,* **2017**, 7(8), 5134-5141.

97. Xu, C.; Shen, P.k.; and Liu, Y. Ethanol electrooxidation on Pt/C and Pd/C catalysts promoted with oxide. *Journal of Power Sources,* **2007**, 164(2), 527-531.

98. Murphin Kumar, P.S.; Thiripuranthagan, S.; Imai, T.; Kumar, G.; Pugazhendhi, A.; Vijayan, S.R.; Esparza, R.; Abe, H.; and Krishnan, S.K. Pt nanoparticles supported on mesoporous CeO_2 nanostructures obtained through green approach for efficient catalytic performance

toward ethanol electro-oxidation. *ACS Sustainable Chemistry & Engineering,* **2017**, 5(12), 11290-11299.

99. Santoro, T.A.B.; Neto, A.O.; Forbicini, C.A.L.G.d.O.; Linardi, M.; Rodríguez, J.L.; and Pastor, E. Ethanol electrooxidation on Pt with lanthanum oxide as cocatalyst in a DAFC. *International Journal of Electrochemistry,* **2012**, 2012, 6.

100. Guo, D.J.; Qiu, X.P.; Chen, L.Q.; and Zhu, W.T. Multi-walled carbon nanotubes modified by sulfated TiO_2 – A promising support for Pt catalyst in a direct ethanol fuel cell. *Carbon,* **2009**, 47(7), 1680-1685.

101. Song, H.; Qiu, X.; Li, X.; Li, F.; Zhu, W.; and Chen, L. TiO_2 nanotubes promoting Pt/C catalysts for ethanol electro-oxidation in acidic media. *Journal of Power Sources,* **2007**, 170(1), 50-54.

102. Salazar-Banda, G.R.; Suffredini, H.B.; Calegaro, M.L.; Tanimoto, S.T.; and Avaca, L.A. Sol–gel-modified boron-doped diamond surfaces for methanol and ethanol electro-oxidation in acid medium. *Journal of Power Sources,* **2006**, 162(1), 9-20.

103. Lima, F.H.B. and Gonzalez, E.R. Ethanol electro-oxidation on carbon-supported Pt–Ru, Pt–Rh and Pt–Ru–Rh nanoparticles. *Electrochimica Acta,* **2008**, 53(6), 2963-2971.

104. Nakagawa, N.; Kaneda, Y.; Wagatsuma, M.; and Tsujiguchi, T. Product distribution and the reaction kinetics at the anode of direct ethanol fuel cell with Pt/C, PtRu/C and PtRuRh/C. *Journal of Power Sources,* **2012**, 199, 103-109.

105. Ribadeneira, E. and Hoyos, B.A. Evaluation of Pt–Ru–Ni and Pt–Sn–Ni catalysts as anodes in direct ethanol fuel cells. *Journal of Power Sources,* **2008**, 180(1), 238-242.

106. Wang, Z.B.; Yin, G.P.; Zhang, J.; Sun, Y.C.; and Shi, P.F. Investigation of ethanol electrooxidation on a Pt–Ru–Ni/C catalyst for a direct ethanol fuel cell. *Journal of Power Sources,* **2006**, 160(1), 37-43.

107. Wang, Z.B.; Yin, G.P.; and Lin, Y.G. Synthesis and characterization of PtRuMo/C nanoparticle electrocatalyst for direct ethanol fuel cell. *Journal of Power Sources,* **2007**, 170(2), 242-250.

108. Zhou, W.J.; Li, W.Z.; Song, S.Q.; Zhou, Z.H.; Jiang, L.H.; Sun, G.Q.; Xin, Q.; Poulianitis, K.; Kontou, S.; and Tsiakaras, P. Bi- and tri-metallic Pt-based anode catalysts for direct ethanol fuel cells. *Journal of Power Sources,* **2004**, 131(1), 217-223.

109. Oliveira Neto, A.; Franco, E.G.; Aricó, E.; Linardi, M.; and Gonzalez, E.R. Electro-oxidation of methanol and ethanol on Pt–Ru/C and Pt–Ru–Mo/C electrocatalysts prepared by Bönnemann's method. *Journal of the European Ceramic Society,* **2003**, 23(15), 2987-2992.

110. García, G.; Tsiouvaras, N.; Pastor, E.; Peña, M.A.; Fierro, J.L.G.; and Martínez-Huerta, M.V. Ethanol oxidation on PtRuMo/C catalysts: In situ FTIR spectroscopy and DEMS studies. *International Journal of Hydrogen Energy,* **2012**, 37(8), 7131-7140.

111. Tanaka, S.; Umeda, M.; Ojima, H.; Usui, Y.; Kimura, O.; and Uchida, I. Preparation and evaluation of a multi-component catalyst by using a co-sputtering system for anodic oxidation of ethanol. *Journal of Power Sources,* **2005**, 152, 34-39.

112. Brandalise, M.; Tusi, M.M.; Piasentin, R.M.; Linardi, M.; Spinacé, E.V.; and Neto, A.O. PtRu/C and PtRuBi/C electrocatalysts prepared in two different ways by borohydride reduction for ethanol electro-oxidation. *International Journal of Electrochemical Science,* **2010**, 5, 39-45.

113. Li, H.; Kang, D.; Wang, H.; and Wang, R. Carbon-supported Pt-RuCo nanoparticles with low-noble metal content and superior catalysis for ethanol oxidization. *International Journal of Electrochemical Science,* **2011**, 6, 1058-1065.

114. Comignani, V.; Sieben, J.M.; Sanchez, M.D.; and Duarte, M.M.E. Influence of carbon support properties on the electrocatalytic activity of PtRuCu nanoparticles for methanol and ethanol oxidation. *International Journal of Hydrogen Energy,* **2017**, 42(39), 24785-24796.

115. Li, G. and Pickup, P.G. The promoting effect of Pb on carbon supported Pt and Pt/Ru catalysts for electro-oxidation of ethanol. *Electrochimica Acta,* **2006**, 52(3), 1033-1037.

116. Beyhan, S.; Coutanceau, C.; Léger, J.-M.; Napporn, T.W.; and Kadırgan, F. Promising anode candidates for direct ethanol fuel cell: Carbon supported PtSn-based trimetallic catalysts prepared by Bönnemann method. *International Journal of Hydrogen Energy,* **2013**, 38(16), 6830-6841.

117. Li, M.; Zhou, W.P.; Marinkovic, N.S.; Sasaki, K.; and Adzic, R.R. The role of rhodium and tin oxide in the platinum-based electrocatalysts for ethanol oxidation to CO_2. *Electrochimica Acta,* **2013**, 104, 454-461.

118. Kowal, A.; Li, M.; Shao, M.; Sasaki, K.; Vukmirovic, M.B.; Zhang, J.; Marinkovic, N.S.; Liu, P.; Frenkel, A.I.; and Adzic, R.R. Ternary Pt/Rh/SnO_2 electrocatalysts for oxidizing ethanol to CO_2. *Nature Materials,* **2009**, 8(4), 325-330.

119. Silva-Junior, L.C.; Maia, G.; Passos, R.R.; de Souza, E.A.; Camara, G.A.; and Giz, M.J. Analysis of the selectivity of PtRh/C and PtRhSn/C to the formation of CO_2 during ethanol electrooxidation. *Electrochimica Acta,* **2013**, 112, 612-619.

120. Erini, N.; Loukrakpam, R.; Petkov, V.; Baranova, E.A.; Yang, R.; Teschner, D.; Huang, Y.; Brankovic, S.R.; and Strasser, P. Ethanol electro-oxidation on ternary platinum-rhodium-tin nanocatalysts: Insights in the atomic 3D structure of the active catalytic phase. *ACS Catalysis,* **2014**, 4(6), 1859-1867.

121. Du, W.X.; Wang, Q.; LaScala, C.A.; Zhang, L.H.; Su, D.; Frenkel, A.I.; Mathur, V.K.; and Teng, X.W. Ternary PtSnRh-SnO_2 nanoclusters: synthesis and electroactivity for ethanol oxidation fuel cell reaction. *Journal of Materials Chemistry,* **2011**, 21(24), 8887-8892.

122. de Souza, E.A.; Giz, M.J.; Camara, G.A.; Antolini, E.; and Passos, R.R. Ethanol electro-oxidation on partially alloyed Pt-Sn-Rh/C catalysts. *Electrochimica Acta,* **2014**, 147, 483-489.

123. Yang, G.; Frenkel, A.I.; Su, D.; and Teng, X. Enhanced electrokinetics of C−C bond splitting during ethanol oxidation by using a Pt/Rh/Sn catalyst with a partially oxidized Pt and Rh core and a SnO_2 Shell. *ChemCatChem,* **2016**, 8(18), 2876-2880.

124. Chang, Y.W.; Liu, C.W.; Wei, Y.C.; and Wang, K.W. Promotion of PtRu/C anode catalysts for ethanol oxidation reaction by addition of Sn modifier. *Electrochemistry Communications,* **2009**, 11(11), 2161-2164.

125. Chu, Y.H. and Shul, Y.G. Combinatorial investigation of Pt–Ru–Sn alloys as an anode electrocatalysts for direct alcohol fuel cells. *International Journal of Hydrogen Energy,* **2010**, 35(20), 11261-11270.

126. Cunha, E.M.; Ribeiro, J.; Kokoh, K.B.; and de Andrade, A.R. Preparation, characterization and application of Pt–Ru–Sn/C trimetallic electrocatalysts for ethanol oxidation in direct fuel cell. *International Journal of Hydrogen Energy,* **2011**, 36(17), 11034-11042.

127. Liu, C.W.; Chang, Y.W.; Wei, Y.C.; and Wang, K.W. The effect of oxygen containing species on the catalytic activity of ethanol oxidation for PtRuSn/C catalysts. *Electrochimica Acta,* **2011**, 56(5), 2574-2581.

128. Wang, R.; Liu, Z.; Ma, Y.; Wang, H.; Linkov, V.; and Ji, S. Heterostructure core PdSn–SnO_2 decorated by Pt as efficient electrocatalysts for ethanol oxidation. *International Journal of Hydrogen Energy,* **2013**, 38(31), 13604-13610.

129. Zhu, W.; Ke, J.; Wang, S.B.; Ren, J.; Wang, H.H.; Zhou, Z.Y.; Si, R.; Zhang, Y.W.; and Yan, C.H. Shaping single-crystalline trimetallic Pt–Pd–Rh nanocrystals toward high-efficiency C–C splitting of ethanol in conversion to CO_2. *ACS Catalysis,* **2015**, 5(3), 1995-2008.

130. Parreira, L.S.; da Silva, J.C.M.; D'Villa -Silva, M.; Simões, F.C.; Garcia, S.; Gaubeur, I.; Cordeiro, M.A.L.; Leite, E.R.; and dos Santos, M.C. PtSnNi/C nanoparticle electrocatalysts for the ethanol oxidation reaction: Ni stability study. *Electrochimica Acta,* **2013**, 96, 243-252.

131. Beyhan, S.; Léger, J.-M.; and Kadırgan, F. Pronounced synergetic effect of the nano-sized PtSnNi/C catalyst for ethanol oxidation in direct ethanol fuel cell. *Applied Catalysis B: Environmental,* **2013**, 130-131, 305-313.

132. Huang, M.; Wu, W.; Wu, C.; and Guan, L. Pt_2SnCu nanoalloy with surface enrichment of Pt defects and SnO_2 for highly efficient electrooxidation of ethanol. *Journal of Materials Chemistry A,* **2015**, 3(9), 4777-4781.

133. Li, M.; Cullen, D.A.; Sasaki, K.; Marinkovic, N.S.; More, K.; and Adzic, R.R. Ternary electrocatalysts for oxidizing ethanol to carbon dioxide: Making Ir capable of splitting C-C bond. *Journal of the American Chemical Society,* **2013**, 135(1), 132-141.

134. Sheng, T.; Lin, W.F.; Hardacre, C.; and Hu, P. Significance of beta-dehydrogenation in ethanol electro-oxidation on platinum doped with Ru, Rh, Pd, Os and Ir. *Physical Chemistry Chemical Physics,* **2014**, 16(26), 13248-13254.

135. Antolini, E.; Colmati, F.; and Gonzalez, E.R. Effect of Ru addition on the structural characteristics and the electrochemical activity for ethanol oxidation of carbon supported Pt–Sn alloy catalysts. *Electrochemistry Communications,* **2007**, 9(3), 398-404.

136. Wu, G.; Swaidan, R.; and Cui, G. Electrooxidations of ethanol, acetaldehyde and acetic acid using PtRuSn/C catalysts prepared by modified alcohol-reduction process. *Journal of Power Sources,* **2007**, 172(1), 180-188.

137. Zhu, M.; Shao, Q.; Pi, Y.; Guo, J.; Huang, B.; Qian, Y.; and Huang, X. Ultrathin vein-like iridium–tin nanowires with abundant oxidized tin as high-performance ethanol oxidation electrocatalysts. *Small,* **2017**, 13(36), 1701295.

138. Du, W.; Wang, Q.; Saxner, D.; Deskins, N.A.; Su, D.; Krzanowski, J.E.; Frenkel, A.I.; and Teng, X. Highly active iridium/iridium–tin/tin oxide heterogeneous nanoparticles as alternative electrocatalysts for the ethanol oxidation reaction. *Journal of the American Chemical Society,* **2011**, 133(38), 15172-15183.

139. Chai, D.; Wang, W.; Wang, F.; Jing, W.; Wang, P.; and Lei, Z. Heterogeneous Ir_3Sn–CeO_2/C as alternative Pt-free electrocatalysts for ethanol oxidation in acidic media. *International Journal of Hydrogen Energy,* **2017**, 42(15), 9775-9783.

140. Du, W.; Deskins, N.A.; Su, D.; and Teng, X. Iridium–ruthenium alloyed nanoparticles for the ethanol oxidation fuel cell reactions. *ACS Catalysis,* **2012**, 2(6), 1226-1231.

141. Courtois, J.; Du, W.; Wong, E.; Teng, X.; and Deskins, N.A. Screening iridium-based bimetallic alloys as catalysts for direct ethanol fuel cells. *Applied Catalysis A: General,* **2014**, 483, 85-96.

142. Lai, S.C.S.; Kleyn, S.E.F.; Rosca, V.; and Koper, M.T.M. Mechanism of the dissociation and electrooxidation of ethanol and acetaldehyde on platinum as studied by SERS. *Journal of Physical Chemistry C,* **2008**, 112(48), 19080-19087.

143. Kutz, R.B.; Braunschweig, B.; Mukherjee, P.; Behrens, R.L.; Dlott, D.D.; and Wieckowski, A. Reaction pathways of ethanol electrooxidation on polycrystalline platinum catalysts in acidic electrolytes. *Journal of Catalysis,* **2011**, 278(2), 181-188.

144. Bard, A.J. and Faulkner, Larry R. Electrochemical methods: Fundamentals and applications, 2nd Edition. *JOHN WILEY & SONS, INC,* **2000**.

145. Mojet, B.L.; Ebbesen, S.D.; and Lefferts, L. Light at the interface: the potential of attenuated total reflection infrared spectroscopy for understanding heterogeneous catalysis in water. *Chemical Society Reviews,* **2010**, 39(12), 4643-4655.

146. Yajima, T.; Uchida, H.; and Watanabe, M. In-situ ATR-FTIR spectroscopic study of electro-oxidation of methanol and adsorbed CO at Pt-Ru alloy. *Journal of Physical Chemistry B,* **2004**, 108(8), 2654-2659.

147. Leung, L.W.H. and Weaver, M.J. Reactant structural effects on the formation and electro-oxidation of adsorbed carbon-monoxide from small organic-molecules at platinum as studied by time-resolved FTIR spectroscopy. *Journal of Electroanalytical Chemistry,* **1988**, 240(1-2), 341-348.

148. Leung, L.W.H.; Chang, S.C.; and Weaver, M.J. Real-time FTIR spectroscopy as an electrochemical mechanistic probe - electrooxidation of ethanol and related species on well-defined Pt(111) surfaces. *Journal of Electroanalytical Chemistry,* **1989**, 266(2), 317-336.

149. Gao, P.; Chang, S.C.; Zhou, Z.H.; and Weaver, M.J. Electrooxidation pathways of simple alcohols at platinum in pure nonaqueous and concentrated aqueous environments as studied by real-time FTIR spectroscopy. *Journal of Electroanalytical Chemistry,* **1989**, 272(1-2), 161-178.

150. Chang, S.C.; Leung, L.W.H.; and Weaver, M.J. Metal crystallinity effects in electrocatalysis as probed by real-time FTIR spectroscopy-electrooxidation of formic-acid, methanol, and ethanol on ordered low-index platinum surfaces. *Journal of Physical Chemistry,* **1990**, 94(15), 6013-6021.

151. Schmiemann, U.; Muller, U.; and Baltruschat, H. The influence of the surface-structure on the adsorption of ethene, ethanol and cyclohexene as studied by DEMS. *Electrochimica Acta,* **1995**, 40(1), 99-107.

152. Tian, Z.Q.; Ren, B.; and Wu, D.Y. Surface-enhanced raman scattering: From noble to transition metals and from rough surfaces to ordered nanostructures. *The Journal of Physical Chemistry B,* **2002**, 106(37), 9463-9483.

153. Guyot-Sionnest, P.; Superfine, R.; Hunt, J.H.; and Shen, Y.R. Vibrational spectroscopy of a silane monolayer at air/solid and liquid/solid interfaces using sum-frequency generation. *Chemical Physics Letters,* **1988**, 144(1), 1-5.

154. Peremans, A.; Tadjeddine, A.; and Guyot-Sionnest, P. Vibrational dynamics of CO at the (100) platinum electrochemical interface. *Chemical Physics Letters,* **1995**, 247(3), 243-248.

155. Gomes, J.F.; Busson, B.; and Tadjeddine, A. SFG study of the ethanol in an acidic medium−Pt(110) interface: Effects of the alcohol concentration. *The Journal of Physical Chemistry B,* **2006**, 110(11), 5508-5514.

156. Yang, S.; Noguchi, H.; and Uosaki, K. Electronic structure of the CO/Pt(111) electrode interface probed by potential-dependent IR/visible double resonance sum frequency generation spectroscopy. *The Journal of Physical Chemistry C,* **2015**, 119(46), 26056-26063.

157. A. Lagutchev; G. Q. Lu; T. Takeshita; Dana D. Dlott; and Wieckowskia, A. Vibrational sum frequency generation studies of the $(2\times2)\rightarrow(\sqrt{19}\times\sqrt{19})$ $(2\times2)\rightarrow(\sqrt{19}\times\sqrt{19})$ phase transition of CO on Pt(111) electrodes. *The Journal of Chemical Physics,* **2006**, 125(15), 10.

158. Gomes, J.F.; Busson, B.; Tadjeddine, A.; and Tremiliosi-Filho, G. Ethanol electro-oxidation over Pt(hkl): Comparative study on the reaction intermediates probed by FTIR and SFG spectroscopies. *Electrochimica Acta,* **2008**, 53(23), 6899-6905.

159. Braunschweig, B.; Mukherjee, P.; Dlott, D.D.; and Wieckowski, A. Real-time investigations of Pt(111) surface transformations in sulfuric acid solutions. *Journal of the American Chemical Society,* **2010**, 132(40), 14036-14038.

160. Gomes, J.F.; Bergamaski, K.; Pinto, M.F.S.; and Miranda, P.B. Reaction intermediates of ethanol electro-oxidation on platinum investigated by SFG spectroscopy. *Journal of Catalysis,* **2013**, 302, 67-82.

161. Kutz, R.B.; Braunschweig, B.; Mukherjee, P.; Dlott, D.D.; and Wieckowski, A. Study of ethanol electrooxidation in alkaline electrolytes with isotope labels and sum-frequency generation. *The Journal of Physical Chemistry Letters,* **2011**, 2(17), 2236-2240.

162. Bruckenstein, S. and Gadde, R.R. Use of a porous electrode for in situ mass spectrometric determination of volatile electrode reaction products. *Journal of the American Chemical Society,* **1971**, 93(3), 793-794.

163. Wolter, O. and Heitbaum, J. Differential electrochemical mass spectroscopy (DEMS) -A new method for the study of electrode processes. *Berichte der Bunsengesellschaft für physikalische Chemie,* **1984**, 88(1), 2-6.

164. Baltruschat, H. and Schmiemann, U. The adsorption of unsaturated organic species at single crystal electrodes studied by differential electrochemical mass spectrometry. *Berichte der Bunsengesellschaft für physikalische Chemie,* **1993**, 97(3), 452-460.

165. Hartung, T. and Baltruschat, H. Differential electrochemical mass spectrometry using smooth electrodes: Adsorption and hydrogen/deuterium exchange reactions of benzene on platinum. *Langmuir,* **1990**, 6(5), 953-957.

166. Bogdanoff, P.; Friebe, P.; and Alonso-Vante, N. A new inlet system for differential electrochemical mass spectroscopy applied to the photocorrosion of p-InP(111) single crystals. *Journal of the Electrochemical Society,* **1998**, 145(2), 576-582.

167. Tegtmeyer, D.; Heindrichs, A.; and Heitbaum, J. Electrochemical on line mass-spectrometry on a rotating electrode inlet system. *Berichte der Bunsengesellschaft Physical Chemistry Chemical Physics,* **1989**, 93(2), 201-206.

168. Wasmus, S.; Cattaneo, E.; and Vielstich, W. Reduction of carbon-dioxide to methane and ethene - An online MS study with rotating electrodes. *Electrochimica Acta,* **1990**, 35(4), 771-775.

169. Gao, Y.Z.; Tsuji, H.; Hattori, H.; and Kita, H. New online mass-spectrometer system designed for platinum single-crystal electrode and electroreduction of acetylene. *Journal of Electroanalytical Chemistry,* **1994**, 372(1-2), 195-200.

170. Wonders, A.H.; Housmans, T.H.M.; Rosca, V.; and Koper, M.T.M. On-line mass spectrometry system for measurements at single-crystal electrodes in hanging meniscus configuration. *Journal of Applied Electrochemistry,* **2006**, 36(11), 1215-1221.

171. Bogdanoff, P. and Alonsovante, N. Online determination via differential electrochemical mass-spectroscopy (DEMS) of chemical-products formed in photoelectrocatalytical

systems. *Berichte der Bunsengesellschaft Physical Chemistry Chemical Physics,* **1993**, 97(7), 940-942.

172. Manzo-Robledo, A.; Boucher, A.C.; Pastor, E.; and Alonso-Vante, N. Electro-oxidation of carbon monoxide and methanol on carbon-supported Pt-Sn nanoparticles: A DEMS study. *Fuel Cells,* **2003**, 2(2), 109-116.

173. Seiler, T.; Savinova, E.R.; Friedrich, K.A.; and Stimming, U. Poisoning of PtRu/C catalysts in the anode of a direct methanol fuel cell: A DEMS study. *Electrochimica Acta,* **2004**, 49(22-23), 3927-3936.

174. Bayer, D.; Cremers, C.; Baltruschat, H.; and Tubke, J. The electro-oxidation of ethanol in alkaline medium at different catalyst metals. *Polymer Electrolyte Fuel Cells,* **2011**, 41(1), 1669-1680.

175. Iwasita, T.; Rasch, B.; Cattaneo, E.; and Vielstich, W. A SNIFTIRS study of ethanol oxidation on platinum. *Electrochimica Acta,* **1989**, 34(8), 1073-1079.

176. Wang, H.; Jusys, Z.; and Behm, R.J. Ethanol electrooxidation on a carbon-supported Pt catalyst: Reaction kinetics and product yields. *Journal of Physical Chemistry B,* **2004**, 108(50), 19413-19424.

177. Vigier, F.; Coutanceau, C.; Hahn, F.; Belgsir, E.M.; and Lamy, C. On the mechanism of ethanol electro-oxidation on Pt and PtSn catalysts: Electrochemical and in situ IR reflectance spectroscopy studies. *Journal of Electroanalytical Chemistry,* **2004**, 563(1), 81-89.

178. Wang, Q.; Sun, G.Q.; Jiang, L.H.; Xin, Q.; Sun, S.G.; Jiang, Y.X.; Chen, S.P.; Jusys, Z.; and Behm, R.J. Adsorption and oxidation of ethanol on colloid-based Pt/C, PtRu/C and Pt3Sn/C catalysts: In situ FTIR spectroscopy and on-line DEMS studies. *Physical Chemistry Chemical Physics,* **2007**, 9(21), 2686-2696.

179. Kavanagh, R.; Cao, X.M.; Lin, W.F.; Hardacre, C.; and Hu, P. Origin of low CO_2 selectivity on platinum in the direct ethanol fuel cell. *Angewandte Chemie International Edition,* **2012**, 51(7), 1572-1575.

180. Du, W.; Mackenzie, K.E.; Milano, D.F.; Deskins, N.A.; Su, D.; and Teng, X. Palladium–tin alloyed catalysts for the ethanol oxidation reaction in an alkaline medium. *ACS Catalysis,* **2012**, 2(2), 287-297.

181. Antolini, E. Palladium in fuel cell catalysis. *Energy & Environmental Science,* **2009**, 2(9), 915-931.

182. Choi, Y. and Liu, P. Understanding of ethanol decomposition on Rh(111) from density functional theory and kinetic Monte Carlo simulations. *Catalysis Today,* **2011**, 165(1), 64-70.

183. Sutton, J.E. and Vlachos, D.G. Ethanol activation on closed-packed surfaces. *Industrial & Engineering Chemistry Research,* **2015**, 54(16), 4213-4225.

184. Rao, V.; Cremers, C.; Stimming, U.; Cao, L.; Sun, S.G.; Yan, S.Y.; Sun, G.Q.; and Xin, Q. Electro-oxidation of ethanol at gas diffusion electrodes. A DEMS study. *Journal of the Electrochemical Society,* **2007**, 154(11), B1138-B1147.

185. Gomes, J.; Profeti, D.; and Deiner, L.J. Influence of the particle size distribution on the activity and selectivity of carbon-supported platinum nanoparticle catalysts for ethanol electrooxidation. *ChemElectroChem,* **2014**, 1(3), 655-662.

186. Bergamaski, K.; Gonzalez, E.R.; and Nart, F.C. Ethanol oxidation on carbon supported platinum-rhodium bimetallic catalysts. *Electrochimica Acta,* **2008**, 53(13), 4396-4406.

187. Colmenares, L.; Wang, H.; Jusys, Z.; Jiang, L.; Yan, S.; Sun, G.Q.; and Behm, R.J. Ethanol oxidation on novel, carbon supported Pt alloy catalysts - Model studies under defined diffusion conditions. *Electrochimica Acta,* **2006**, 52(1), 221-233.

188. Gilman, S. Multipulse potentiodynamic studies of the adsorption of carbon monoxide and hydrogen on rhodium electrodes. II. Mixed adsorption of carbon monoxide and hydrogen. *The Journal of Physical Chemistry,* **1967**, 71(13), 4339-4343.

189. VandeVondele, J.; Krack, M.; Mohamed, F.; Parrinello, M.; Chassaing, T.; and Hutter, J. Quickstep: Fast and accurate density functional calculations using a mixed Gaussian and plane waves approach. *Computer Physics Communications,* **2005**, 167, 103-128.

190. http://www.cp2k.org. *CP2K developers home page*. 2015.

191. Hutter, J.; Iannuzzi, M.; Schiffmann, F.; and VandeVondele, J. CP2K: atomistic simulations of condensed matter systems. *Wiley Interdisciplinary Reviews: Computational Molecular Science,* **2014**, 4(1), 15-25.

192. Perdew, J.P.; Burke, K.; and Ernzerhof, M. Generalized gradient approximation made simple. *Physical Review Letters,* **1996**, 77, 3865-3868.

193. Vandevondele, J. and Hutter, J. Gaussian basis sets for accurate calculations on molecular systems in gas and condensed phases. *The Journal of Chemical Physics,* **2007**, 127(11), 114105-114105.

194. Goedecker, S.; Teter, M.; and Hutter, J. Separable dual-space Gaussian pseudopotentials. *Physical Review B,* **1996**, 54(3), 1703-1710.

195. Krack, M. Pseudopotentials for H to Kr optimized for gradient-corrected exchange-correlation functionals. *Theoretical Chemistry Accounts,* **2005**, 114(1-3), 145-152.

196. Ferrin, P.; Simonetti, D.; Kandoi, S.; Kunkes, E.; Dumesic, J.a.; Nørskov, J.K.; and Mavrikakis, M. Modeling ethanol decomposition on transition metals: A combined application of scaling and Brønsted-Evans-Polanyi relations. *Journal of the American Chemical Society,* **2009**, 131(16), 5809-5815.

197. Zhang, J.; Cao, X.M.; Hu, P.; Zhong, Z.; Borgna, A.; and Wu, P. Density functional theory studies of ethanol decomposition on Rh(211). *The Journal of Physical Chemistry C,* **2011**, 115(45), 22429-22437.

198. Guo, W.; Li, M.; Lu, X.; Zhu, H.; Li, Y.; Li, S.; and Zhao, L. Ethanol decomposition on a Pd(110) surface: A density functional theory investigation. *Dalton Transactions,* **2013**, 42(6), 2309-2318.

199. Wang, S.; Temel, B.; Shen, J.; Jones, G.; Grabow, L.C.; Studt, F.; Bligaard, T.; Abild-Pedersen, F.; Christensen, C.H.; Nørskov, J.K.; Claus, F.A.-p.; and Jens, H.C. Universal Brønsted-Evans-Polanyi relations for C–C, C–O, C–N, N–O, N–N, and O–O dissociation reactions. *Catalysis Letters,* **2010**, 141(3), 370-373.

200. Molina, L.M.; Rasmussen, M.D.; and Hammer, B. Adsorption of O_2 and oxidation of CO at Au nanoparticles supported by TiO_2(110). *The Journal of Chemical Physics,* **2004**, 120(16), 7673-7680.

201. Chen, W.; Tao, Q.; Cai, J.; and Chen, Y.-X. The effect of alcohol concentration on the mass signal of CO_2 detected by differential mass spectrometry. *Electrochemistry Communications,* **2014**, 48, 10-12.

202. Shao, M.H. and Adzic, R.R. Electrooxidation of ethanol on a Pt electrode in acid solutions: In situ ATR-SEIRAS study. *Electrochimica Acta,* **2005**, 50(12), 2415-2422.

203. Hitmi, H.; Belgsir, E.M.; Leger, J.M.; Lamy, C.; and Lezna, R.O. A kinetic, analysis of the electrooxidation of ethanol at a platinum-electrode in acid-medium. *Electrochimica Acta,* **1994**, 39(3), 407-415.

204. Giz, M.J. and Camara, G.A. The ethanol electrooxidation reaction at Pt (111): The effect of ethanol concentration. *Journal of Electroanalytical Chemistry,* **2009**, 625(2), 117-122.

205. Qadir, K.; Joo, S.H.; Mun, B.S.; Butcher, D.R.; Renzas, J.R.; Aksoy, F.; Liu, Z.; Somorjai, G.A.; and Park, J.Y. Intrinsic relation between catalytic activity of CO oxidation on Ru nanoparticles and ru oxides uncovered with ambient pressure XPS. *Nano Letters,* **2012**, 12(11), 5761-5768.

206. Grass, M.E.; Zhang, Y.; Butcher, D.R.; Park, J.Y.; Li, Y.; Bluhm, H.; Bratlie, K.M.; Zhang, T.; and Somorjai, G.A. A reactive oxide overlayer on rhodium nanoparticles during CO oxidation and its size dependence studied by in situ ambient-pressure X-ray photoelectron spectroscopy. *Angewandte Chemie International Edition,* **2008**, 47(46), 8893-8896.

207. Duan, Z. and Henkelman, G. CO oxidation on the Pd(111) surface. *ACS Catalysis,* **2014**, 4(10), 3435-3443.

208. Ackermann, M.D.; Pedersen, T.M.; Hendriksen, B.L.M.; Robach, O.; Bobaru, S.C.; Popa, I.; Quiros, C.; Kim, H.; Hammer, B.; Ferrer, S.; and Frenken, J.W.M. Structure and reactivity of surface oxides on Pt(110) during catalytic co oxidation. *Physical Review Letters,* **2005**, 95(25), 255505.

209. Westerström, R.; Wang, J.G.; Ackermann, M.D.; Gustafson, J.; Resta, A.; Mikkelsen, A.; Andersen, J.N.; Lundgren, E.; Balmes, O.; Torrelles, X.; Frenken, J.W.M.; and Hammer, B. Structure and reactivity of a model catalyst alloy under realistic conditions. *Journal of Physics: Condensed Matter,* **2008**, 20(18), 184018.

210. De Souza, R.F.B.; Silva, J.C.M.; Assumpção, M.H.M.T.; Neto, A.O.; and Santos, M.C. Ethanol oxidation reaction using PtSn/C+Ce/C electrocatalysts: Aspects of ceria contribution*. Electrochimica Acta,* **2014**, 117, 292-298.

211. Trasatti, S. and Petrii, O.A. Real surface area measurements in electrochemistry*. Journal of Electroanalytical Chemistry,* **1992**, 327(1), 353-376.

212. Yin, J.; Shan, S.; Ng, M.S.; Yang, L.; Mott, D.; Fang, W.; Kang, N.; Luo, J.; and Zhong, C.-J. Catalytic and electrocatalytic oxidation of ethanol over palladium-based nanoalloy catalysts*. Langmuir,* **2013**, 29(29), 9249-9258.

213. Mavrikakis, M.; Hammer, B.; and Norskov, J.K. Effect of strain on the reactivity of metal surfaces*. Physical Review Letters,* **1998**, 81(13), 2819-2822.

214. Strasser, P.; Koh, S.; Anniyev, T.; Greeley, J.; More, K.; Yu, C.; Liu, Z.; Kaya, S.; Nordlund, D.; Ogasawara, H.; Toney, M.F.; and Nilsson, A. Lattice-strain control of the activity in dealloyed core–shell fuel cell catalysts*. Nature Chemistry,* **2010**, 2(6), 454-460.

215. Fujita, T.; Guan, P.; McKenna, K.; Lang, X.; Hirata, A.; Zhang, L.; Tokunaga, T.; Arai, S.; Yamamoto, Y.; Tanaka, N.; Ishikawa, Y.; Asao, N.; Yamamoto, Y.; Erlebacher, J.; and Chen, M. Atomic origins of the high catalytic activity of nanoporous gold*. Nature Materials,* **2012**, 11(9), 775-780.

216. Rizo, R.; Lazaro, M.J.; Pastor, E.; and Garcia, G. Spectroelectrochemical study of carbon monoxide and ethanol oxidation on Pt/C, PtSn(3:1)/C and PtSn(1:1)/C catalysts*. Molecules,* **2016**, 21(9), 12.

217. Bach Delpeuch, A.; Chatenet, M.; Rau, M.S.; and Cremers, C. Influence of H- and OH-adsorbates on the ethanol oxidation reaction - A DEMS study*. Physical Chemistry Chemical Physics,* **2015**, 17(16), 10881-10893.

218. Sun, S.; Halseid, M.C.; Heinen, M.; Jusys, Z.; and Behm, R.J. Ethanol electrooxidation on a carbon-supported Pt catalyst at elevated temperature and pressure: A high-temperature/high-pressure DEMS study*. Journal of Power Sources,* **2009**, 190(1), 2-13.

219. Huang, Y.F.; Kooyman, P.J.; and Koper, M.T.M. Intermediate stages of electrochemical oxidation of single-crystalline platinum revealed by in situ Raman spectroscopy*. Nature Communication,* **2016**, 7, 12440.

220. Topalov, A.A.; Katsounaros, I.; Auinger, M.; Cherevko, S.; Meier, J.C.; Klemm, S.O.; and Mayrhofer, K.J.J. Dissolution of platinum: Limits for the deployment of electrochemical energy conversion? *Angewandte Chemie International Edition,* **2012**, 51(50), 12613-12615.

221. Cherevko, S.; Keeley, G.P.; Geiger, S.; Zeradjanin, A.R.; Hodnik, N.; Kulyk, N.; and Mayrhofer, K.J.J. Dissolution of platinum in the operational range of fuel cells*. ChemElectroChem,* **2015**, 2(10), 1471-1478.

222. Souza-Garcia, J.; Herrero, E.; and Feliu, J.M. Breaking the C-C bond in the ethanol oxidation reaction on platinum electrodes: Effect of steps and ruthenium adatoms*. ChemPhysChem,* **2010**, 11(7), 1391-1394.

223. Florez-Montano, J.; Garcia, G.; Guillen-Villafuerte, O.; Rodriguez, J.L.; Planes, G.A.; and Pastor, E. Mechanism of ethanol electrooxidation on mesoporous Pt electrode in acidic medium studied by a novel electrochemical mass spectrometry set-up. *Electrochimica Acta,* **2016**, 209, 121-131.

224. Rossmeisl, J.; Nørskov, J.K.; Taylor, C.D.; Janik, M.J.; and Neurock, M. Calculated phase diagrams for the electrochemical oxidation and reduction of water over Pt(111). *The Journal of Physical Chemistry B,* **2006**, 110(43), 21833-21839.

APPENDICES

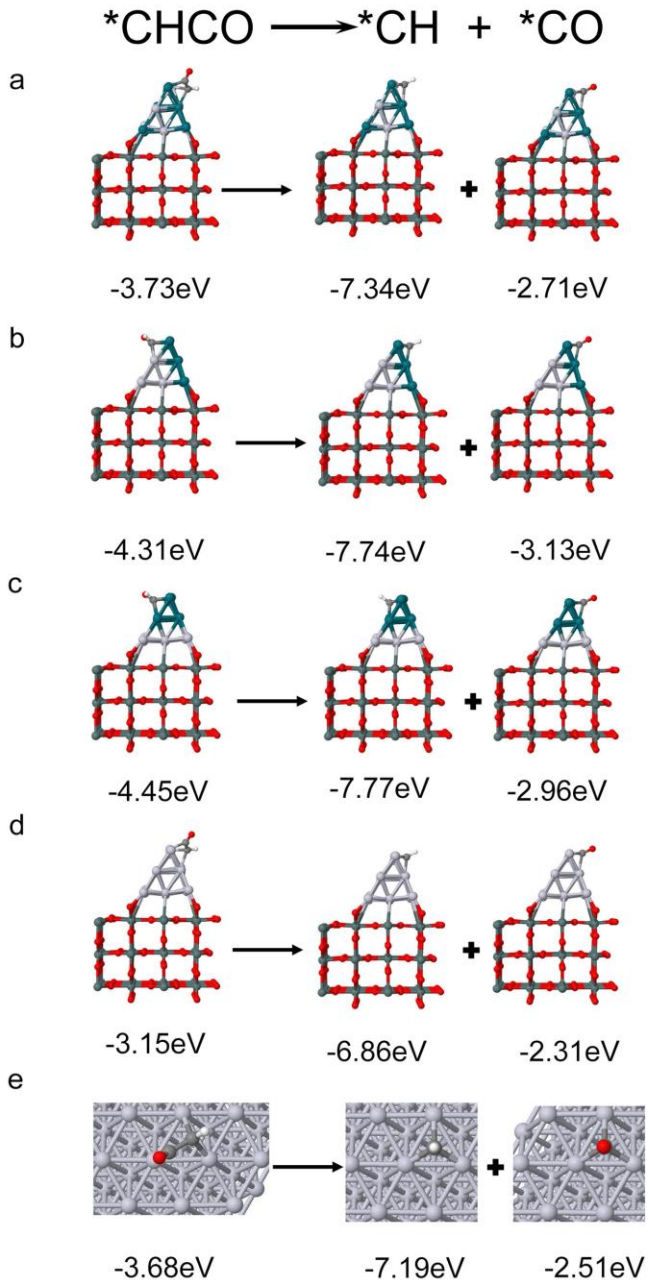

Appendix Figure 1. Reactions for C-C bond scission of *CHCO on various catalyst surfaces: (a) PtRh-SnO_2 (1st model), (b) PtRh-SnO_2 (2nd model), (c) PtRh-SnO_2 (3rd model), (d) Pt-SnO_2 and (e) Pt(111). Numbers indicate adsorption energies of the indicated species.

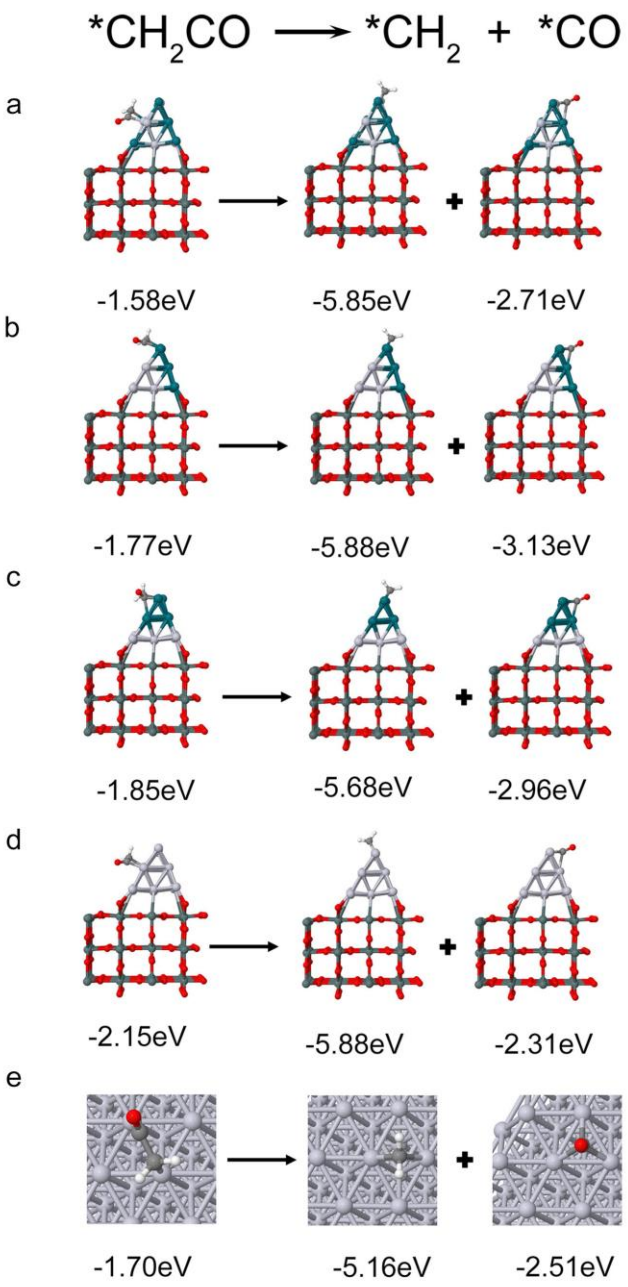

Appendix Figure 2. Reactions for C-C bond scission of *CH_2CO on various catalyst surfaces: (a) PtRh-SnO_2 (1st model), (b) PtRh-SnO_2 (2nd model), (c) PtRh-SnO_2 (3rd model), (d) Pt-SnO_2 and (e) Pt(111). Numbers indicate adsorption energies of the indicated species.

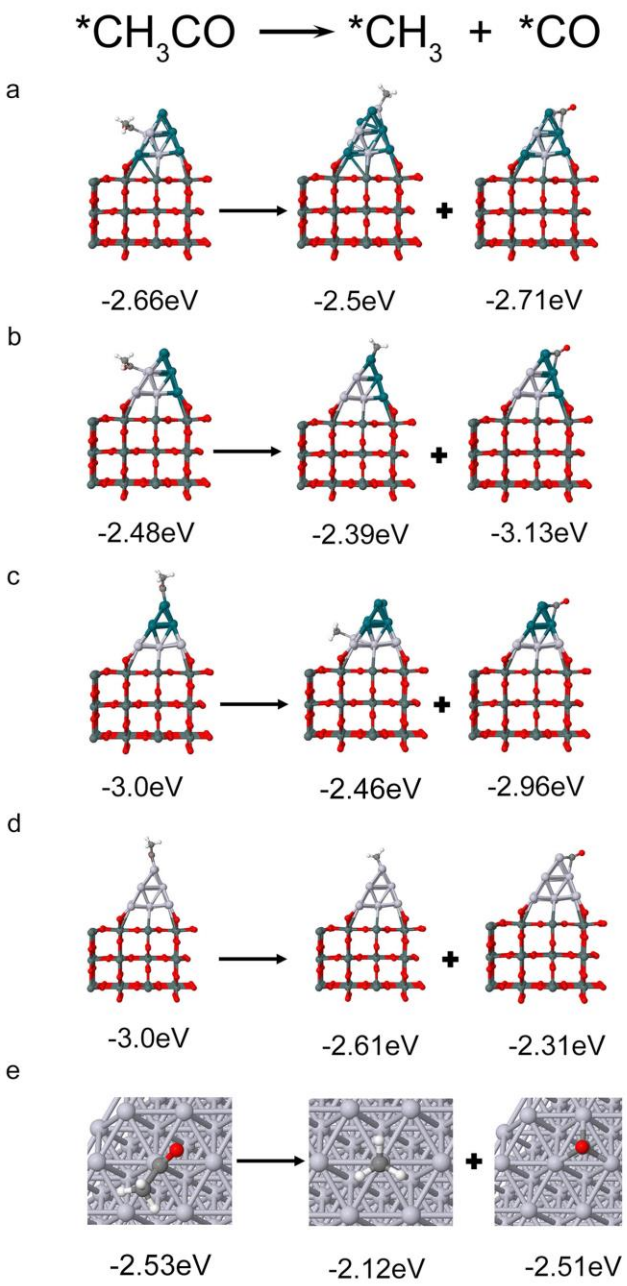

Appendix Figure 3. Reactions for C-C bond scission of *CH_3CO on various catalyst surfaces: (a) PtRh-SnO_2 (1st model), (b) PtRh-SnO_2 (2nd model), (c) PtRh-SnO_2 (3rd model), (d) Pt-SnO_2 and (e) Pt(111). Numbers indicate adsorption energies of the indicated species.

Appendix Table 1

Vapor pressure of water-P_{water} (mmHg)

T	P_{water}	*T*	P_{water}	*T*	P_{water}	*T*	P_{water}
20.0	17.535	**23.0**	21.068	**26.0**	25.209	**29.0**	30.043
20.2	17.753	**23.2**	21.324	**26.2**	25.509	**29.2**	30.392
20.4	17.974	**23.4**	21.583	**26.4**	25.812	**29.4**	30.745
20.6	18.197	**23.6**	21.845	**26.6**	26.117	**29.6**	31.102
20.8	18.422	**23.8**	22.110	**26.8**	26.426	**29.8**	31.461
21.0	18.650	**24.0**	22.377	**27.0**	26.739	**30.0**	31.824
21.2	18.880	**24.2**	22.648	**27.2**	27.055	**30.2**	32.191
21.4	19.113	**24.4**	22.922	**27.4**	27.374	**30.4**	32.561
21.6	19.349	**24.6**	23.198	**27.6**	27.696	**30.6**	32.934
21.8	19.578	**24.8**	23.476	**27.8**	28.021	**30.8**	33.312
22.0	19.827	**25.0**	23.756	**28.0**	28.349	**31.0**	33.695
22.2	20.070	**25.2**	24.039	**28.2**	28.680	**31.2**	34.082
22.4	20.316	**25.4**	24.326	**28.4**	29.015	**31.4**	34.471
22.6	20.565	**25.6**	24.617	**28.6**	29.354	**31.6**	34.864
22.8	20.815	**25.8**	24.912	**28.8**	29.697	**31.8**	35.261

Appendix Table 2

Temperature (T/ºC) vs. absorption coefficient (a) for carbon dioxide in water

T	a	T	a
5	1.424	**19**	0.902
6	1.377	**20**	0.878
7	1.331	**21**	0.854
8	1.282	**22**	0.829
9	1.237	**23**	0.804
10	1.194	**24**	0.781
11	1.154	**25**	0.759
12	1.117	**26**	0.738
13	1.083	**27**	0.718
14	1.050	**28**	0.699
15	1.019	**29**	0.682
16	0.985	**30**	0.665
17	0.956	**35**	0.592
18	0.928	**40**	0.530

Author's Publications

1.Guangxing Yang, Lida M. Namin, N. Aaron Deskins, Xiaowei Teng. Influence of ∗OH adsorbates on the potentiodynamics of the CO_2 generation during the electro-oxidation of ethanol. *Journal of Catalysis*, **2017**, 353, 335-348.

2.Guangxing Yang, Anatoly I. Frenkel, Dong Su, Xiaowei Teng. Enhanced electrokinetics of C-C bond splitting during ethanol oxidation by using a Pt/Rh/Sn catalyst with a partially oxidized Pt and Rh core and a SnO_2 shell. *ChemCatChem*,**2016**,8, 2876–2880. (Cover paper)

3.Wenxin Du, Guangxing Yang, Emily Wong, N. Aaron Deskins, Anatoly I. Frenkel, Dong Su, Xiaowei Teng. Platinum-tin oxide core–shell catalysts for efficient electro-oxidation of ethanol. *Journal of the American Chemical Society*,**2014**,136,10862-10865.